ABSTRACT

Title of Document: EXTENSION OF A KINETIC APPROACH TO CHEMICAL REACTIONS TO ELECTRONIC ENERGY LEVELS AND REACTIONS INVOLVING CHARGED SPECIES WITH APPLICATION TO DSMC SIMULATIONS.

Derek Shane Liechty, Ph.D., 2013

Directed By: Mark J. Lewis, Willis Young Professor and Department Chair, Department of Aerospace Engineering

The ability to compute rarefied, ionized hypersonic flows is becoming more important as missions such as Earth reentry, landing high mass payloads on Mars, and the exploration of the outer planets and their satellites are being considered. Recently introduced molecular-level chemistry models that predict equilibrium and nonequilibrium reaction rates using only kinetic theory and fundamental molecular properties are extended in the current work to include electronic energy level transitions and reactions involving charged particles. These extensions are shown to agree favorably with reported transition and reaction rates from the literature for near-equilibrium conditions. Also, the extensions are applied to the second flight of the Project FIRE flight experiment at 1634 seconds with a Knudsen number of 0.001 at an altitude of 76.4 km. In order to accomplish this, NASA's direct simulation Monte Carlo code DAC was rewritten to include the ability to simulate charge-neutral

ionized flows, take advantage of the recently introduced chemistry model, and to include the extensions presented in this work. The 1634 second data point was chosen for comparisons to be made in order to include a CFD solution. The Knudsen number at this point in time is such that the DSMC simulations are still tractable and the CFD computations are at the edge of what is considered valid because, although near-transitional, the flow is still considered to be continuum. It is shown that the inclusion of electronic energy levels in the DSMC simulation is necessary for flows of this nature and is required for comparison to the CFD solution. The flow field solutions are also post-processed by the nonequilibrium radiation code HARA to compute the radiative portion of the heating and is then compared to the total heating measured in flight.

EXTENSION OF A KINETIC APPROACH TO CHEMICAL REACTIONS TO ELECTRONIC ENERGY LEVELS AND REACTIONS INVOLVING CHARGED SPECIES WITH APPLICATION TO DSMC SIMULATIONS

By

Derek Shane Liechty

Dissertation submitted to the Faculty of the Graduate School of the
University of Maryland, College Park, in partial fulfillment
of the requirements for the degree of
Doctor of Philosphy
2013

Advisory Committee:
Professor Mark J. Lewis, Chair
Associate Professor James Baeder
Assistant Professor Ray Sedwick
Associate Professor Kenneth Yu
Professor Gregory Jackson

Acknowledgements

I would first like to thank my wife and children for the love and support that they have provided throughout my graduate career. I couldn't have done it without them.

Second, I must thank my advisor Professor Mark Lewis. He has always been more than willing to sit and discuss how my research was progressing and guide me through the twists and turns of graduate school.

I also need to thank Dr. Christopher Johnston for his assistance in post-processing the DSMC simulations presented herein to obtain the radiative heating to the surface of the Fire II vehicle.

Finally, there have also been many in my professional life that have helped guide me along this path. First, thanks to Dr. N. Ronald Merski, my Branch Head at the NASA Langley Research Center Aerothermodynamics Branch, for the support and patience that he has shown. Also, a huge debt of gratitude goes to Professor Emeritus Graeme Bird, Dr. Richard Wilmoth, and Dr. James Moss for being fantastic role models and mentors.

Table of Contents

List of Tables

List of Figures

Nomenclature

a	Constant in inverse power potential and Arrhenius equation
B	Magnetic field (T)
b	Constant in Arrhenius equation
C_1, C_2	Constants in the Millikan-White vibrational relaxation model and TCE chemistry model
D	Non-collisional operator defined for the Boltzmann equation
E	Electric field (N/C), Energy (J)
e	electron charge (C)
F	Force acting on a particle (N)
f	Distribution function
g	Relative velocity (m/s), degeneracy
h	Planck's constant
i	Energy level
J	Collisional operator defined for the Boltzmann equation
k	Boltzmann constant
k_f, k_r	Forward/reverse reaction or transition rate
M	Normalized collision mass
m	Mass (kg)
m_r	Reduced mass
N	Number of particles in a computational cell
n	Number density (m^{-3})
P	Probability
p	Pressure (N/m^2)
Q^A	Partition function of species A
$Q(v)$	Probability density function for the post-collision velocity v
$Q(a,b)$	Incomplete Gamma function
q	Charge on a particle (C)
R	Random number, Collision rate parameter
T	Temperature (K)
t	Time (s)
W	Number of real particles represented by a simulated particle
V	Volume (m^3)
u,v,w	Velocity in the x-,y-,z-directions (m/s)
Z	Collision number
x,y,z	Cartesian coordinates (m)
α	Exponent in inverse power potential
χ,ψ	Collision angles (rad)
δ	Dirac delta function
ε	Symmetry factor (=1 if dissimilar, =2 if same), specific energy (J/kg)
ε_0	Permittivity of free space
ϕ	Electric potential
Υ	Fraction of collisions that meet conditions for chemical reaction

$\Gamma(a)$	Gamma function of a
μ	Viscosity
Θ	Characteristic temperature (K)
σ	Collision cross-section (m^2)
τ	Mean free time (s)
Ω	Solid angle in a collision (strad)
ω	Exponent in VHS interaction model
ζ	Degrees-of-freedom

Subscripts

AI	Associative ionization
a	Activation
ambipolar	Ambipolar electric field
chex	Charge exchange
coll	Collision
diss	Dissociation
e	Electron
el	Electronic energy mode
eq	Equilibrium
exch	Exchange
f	Forward
int	Internal
ion	Ionization
max	Maximum value
r	Reverse
react	Reaction
rec	Recombination
ref	Reference
rot	Rotational energy mode
T	Total
trans	Translational energy
vib	Vibrational energy mode

Superscripts

AI	Associative ionization
chex	Charge exchange
cont	Continuum value
DSMC	DSMC value
ion	Ionization

Chapter 1: Introduction

The aerothermodynamic environments experienced by hypersonic vehicles are characterized by strong shock waves, which produce high temperatures resulting in high heating of the vehicle. The severity of the environment is dependent upon the mission profile and the vehicle configuration[1]. A high-speed planetary-entry blunt-body vehicle, such as the Galileo probe entering Jupiter or a high speed Earth return capsule, encounters an environment dominated by high enthalpy effects, which include elevated levels of ionization and may result in significant radiative heating. The aerodynamic and aerothermal loads on a hypersonic vehicle set the performance requirements for various sub-systems, such as the thermal protection system (TPS) and the control system. The design and safe operation of these vehicles, therefore, require adequate definition of the flight environment.

During the design phase, the aerothermodynamic performance of a hypersonic vehicle is defined by use of either experimental or computational tools. However, as in most flight regimes, these definitions cannot be solely obtained from ground test facilities, as no facility can reproduce all aspects of the flight environment. This limitation is particularly true for the hypersonic flight regime because of the high energy requirement needed to create a true hypersonic environment at a reasonable scale on the ground, and especially applicable to the transitional/rarefied portion of the trajectory because of the very low density requirement. Therefore, designers rely on computational tools for the prediction of the aerothermal loads experienced by vehicles entering or re-entering the atmosphere from space.

In rarefied flows, because of the breakdown of the continuum assumption, kinetic methods are employed. Since its introduction in the early 1960's, the direct simulation Monte Carlo (DSMC) method of Bird[2] has become the de facto standard for simulating low-density gas dynamics. For these types of flows, traditional computational fluid dynamics (CFD) methods are invalid because assumptions made in developing the differential equations on which they are based break down under rarefied conditions. In contrast to continuum CFD methods, the DSMC method performs a direct physical simulation of the gas at the molecular level that closely mimics the Boltzmann equations. In the simulation, particles are tracked in space and time, accounting for both gas surface interactions and intermolecular collisions.

In the upcoming years, the ability to compute rarefied, ionized hypersonic flows will become increasingly important. Missions such as Earth (re)entry, landing high mass payloads on Mars, and the exploration of the outer planets and their satellites will continue to push the state of the art in DSMC simulations. These missions may result in shock-layer temperatures reaching into the tens-of-thousands of degrees, where the treatment of electronic energy levels and ionization processes becomes increasingly important. The proper treatment of these mechanisms is needed to accurately predict overall shock wave thickness and structure, as well as heat transfer to the vehicle. Even when the reactants are minor species, the overall flow field is not affected by

details of the energy modes and reaction model, but a particular radiation signature may be strongly affected[3]. Either way, the accurate treatment and prediction of electronic energy distribution and ionization is an important component of the design of vehicle sub-systems.

1.1 Objectives of this Work

Although there has been much recent interest in the modeling of ionization processes[4-9], the inclusion of electronic energy levels in DSMC simulations has largely been overlooked and they are not included in many DSMC implementations. However, recent advances in DSMC algorithms[10-14], specifically the Quantum-Kinetic (Q-K) Chemistry Model, have allowed the prediction of equilibrium and non-equilibrium reaction rates using only kinetic theory and fundamental molecular properties (i.e., no macroscopic reaction-rate information). Models such as these are important especially when reaction rate data are limited or the gas is far from equilibrium and an engineering approximation is required. Thus far, these new models have only covered neutral-species reactions. It is the purpose of this thesis to expand the Q-K model to include electronic energy level transitions and also to include reactions involving charged species.

In addition to ionization, radiation can become an important factor depending on the mission and thermal protection system. For example, inflatable ballutes can be used to decelerate spacecraft while still high in the atmosphere. The material used for the skin of the ballute would have a very low tolerance for heating, necessitating the knowledge of what the radiative heating load would be. Several methods of calculating radiative heating for rarefield flows[15-18] have been developed. For the current study, however, an uncoupled methodology used in many computational fluid dynamics radiation evaluations[19, 20] was adopted. While this study does not improve on the methodologies used for calculating the radiative heat transfer, having separate species non-equilibrium electronic temperatures would make radiative predictions much more accurate.

The models developed herein will be validated against reaction rates reported in the literature and applied to the second flight of the Flight Investigation Reentry Environment (FIRE II) Project. This was an Apollo-era flight experiment to measure the radiative and convective heating on spacecraft material during atmospheric reentry at lunar return speeds. The trajectory point at 76.42 km was chosen for the computations because, while the flow is nearly in the transitional regime and DSMC is more appropriate, computational fluid dynamics (CFD) has frequently been applied at this altitude with success. Therefore, the DSMC simulations presented in this thesis will be compared to CFD solutions and flight data from this trajectory point. However, while the methods developed herein are completely applicable to higher altitudes, the use of CFD is not recommended because of the break down of the assumption of continuum flow.

1.2 Outline of Thesis

The remainder of this thesis is organized as follows. The second chapter provides an overview of the governing equations that are the basis for the simulation of fluid flows from the continuum through rarefied regimes. Also, a description of the methodology and structure of the DSMC algorithm, both "traditional" DSMC and the more recent algorithmic advances, is presented as well as previously existing electronic energy level treatments and ionized gas models. Chapter Three describes the extensions to the Q-K model and their implementation. In Chapter Four, these extensions are applied to an adiabatic heat bath and sampled transition/reaction rates are compared to those rates found in the literature. In Chapter Five, these extensions are then compared against previous chemical reaction models as applied to the second Flight Investigation of Reentry Environment (FIRE II) experiment[21]. Finally, Chapter Six summarizes the results of the thesis, the contributions of the thsis to the state-of-the-art, and recommended future research directions.

Chapter 2: Simulation of Rarefied and Weakly Ionized Reentry Flows

In this chapter, the theoretical basis of particle simulation is first summarized. Next, a description of the direct simulation Monte Carlo numerical method is given, including the traditional methods and more recent algorithmic advances, as well as previous attempts to include electronic energy levels and models of ionized flow. Throughout this description, mention will be given of any modifications that were required to be performed on the DSMC algorithm of choice.

2.1 Theoretical Basis of Particle Simulation

The particle simulation method has been developed independently by plasma physicists and aerothermodynamisists. Plasma physicists, who simulate charged particles, have developed the particle-in-cell (PIC) method based on the theory of charge assignment and force interpolation. This theory has made it possible to obtain smooth distributions of charge density and current density in Maxwell's equation of electromagnetic fields. The details of the PIC method can be found in the classical works of Birdsall and Langdon[22] and Hockney and Eastwood[23]. On the other hand, aerothermodynamicists have been developing a particle simulation method of neutral species beginning with the work of Bird[2, 24]. This method is called the direct simulation Monte Carlo (DSMC) method.

Particle simulation of both charged and neutral species is necessary to examine the structures of high-speed, rarefied, reacting flows. However, for flows where the plasma density is considered low (~10%), the assumption of charge neutrality is generally assumed and the charged particles are treated as neutral particles[25-30]. More will be discussed on these techniques in Section 2.2.4. The current section describes how the probability laws used in particle simulation may be derived[31] from a relevant Boltzmann equation for a weakly ionized plasma and simplifications will be pointed out for our assumption of charge neutrality.

2.1.1 The Boltzmann Equation

The theoretical basis of particle simulation can be explained using a weakly ionized plasma consisting of electrons (*e*), ions (*A*), and molecules (*B*). If Coulomb collisions *e-e, e-A,* and *A-A* can be disregarded, only the remaining *e-B, A-B,* and *B-B* collisions need to be considered. The particle motions of species *e, A,* and *B* are governed by the respective Boltzmann equation for each of these species. Except for Coulomb collisions, the Boltzmann equation for electrons or ions is linear, but the Boltzmann equation for molecules is nonlinear because of the *B-B* collisions. Although the PIC method was developed for charged species and the DSMC method for neutral species, the idea behind the two methods is similar. The Boltzmann equation of ions, *A,* is written as:

$$\frac{\partial f_A}{\partial t} + v_j \frac{\partial f_A}{\partial x_j} + \frac{1}{m_A}\frac{\partial}{\partial v_j}\left(\bar{F}_j f_A\right) = \iint\left[f_A(\vec{v}')f(\vec{w}') - f_A(\vec{v})f(\vec{w})\right] g\sigma^{AB}\, d\Omega\, d\vec{w} \quad (2.1.1)$$

Here, Coulomb collisions are neglected and only *A*-*B* collisions are considered, $\vec{F}_j$ is the force acting on particle *A* with a mass of m_A, $f_A(\vec{v})$ and $f_B(\vec{w})$ are the velocity distribution functions of species *A* and *B*, $\vec{v}'$ and $\vec{w}'$ are the post-collision velocities, $g = |\vec{v} - \vec{w}|$ is the relative speed, σ^{AB} is the differential cross section, and $d\Omega$ (=$\sin\chi\, d\chi\, d\psi$) is the solid angle. In the remainder of the derivation, $f_A(\vec{v},\vec{x},t)$ and $f_B(\vec{v},\vec{x},t)$ are expressed as $f_A(\vec{v})$ and $f_B(\vec{v})$ in the right hand side of the equation for simplicity. The differential cross section σ^{AB} is a function of *g* and the deflection angle χ. The force $\vec{F}$ is given by:

$$\vec{F} = q_A\left(\vec{E} + \vec{v} \times \vec{B}\right) \tag{2.1.2}$$

where q_A is the charge of the particle *A* and $\vec{E}$ and $\vec{B}$ are the electric and magnetic fields, respectively. However, for our purposes, the force experienced by the charged particles is effectively zero since there is an assumption of no charge separation (i.e., charge neutrality). For the sake of completeness, though, this term will be kept in the remainder of the derivation.

If the method to obtain $f_A(\vec{v},\vec{x},t)$ is given, the solution of f_A can be found at any time by step-by-step calculations started from an initial velocity distribution function. For a small Δt, we have:

$$f_A(\vec{v},\vec{x},t+\Delta t) = f_A(\vec{v},\vec{x},t) + \Delta t\left(\frac{\partial f_A}{\partial t}\right) \tag{2.1.3}$$

Substituting $\partial f_A / \partial t$ of Equation (2.1.1) into Equation (2.1.3) gives us:

$$f_A(\vec{v},\vec{x},t+\Delta t) = (1+\Delta tJ)(1+\Delta tD) f_A(\vec{v},\vec{x},t) \tag{2.1.4}$$

where *D* and *J* are operators defined by

$$D(f_A) = -v_j \frac{\partial f_A}{\partial x_j} - \frac{1}{m_A}\frac{\partial}{\partial v_j}\left(F_j f_A\right) \tag{2.1.5}$$

$$J(f_A) = \iint\left[f_A(\vec{v}')f_B(\vec{w}') - f_A(\vec{v})f_B(\vec{w})\right] g\sigma^{AB}\, d\Omega\, d\vec{w} \tag{2.1.6}$$

D and *J* denote non-collisional and collisional operators, respectively, and therefore, Equation (2.1.4) decouples the non-collisional and collisional parts of the motion. Equation (2.1.4) is equal to Equation (2.1.3) if the term of order $(\Delta t)^2$ is disregarded such that the solution obtained from Equation (2.1.4) is first-order accurate. In general, Δt should be much less than the mean free time τ (the mean free path divided by the mean speed of the particles). This condition should be strictly satisfied in the case when particle *A* is charged [32]. Note, however, that if particle *A* is a molecule, the condition can be replaced by a weaker one of $\Delta t < \tau$. The reason why the weaker

condition can be applied is that molecular trajectories are straight and, therefore, accurate for any Δt and that the state of the gas changes little in the mean free time.

Equation (2.1.4) suggests that a method of solving the Boltzmann equation is to first obtain $f_A^* \equiv (1+\Delta tD) f_A$ (non-collisional) and then obtain $(1+\Delta tJ) f_A^*$ (collisional). The first procedure is equivalent to solving:

$$\frac{\partial f_A}{\partial t} + v_j \frac{\partial f_A}{\partial x_j} + \frac{1}{m_A} \frac{\partial}{\partial v_j} \left(F_j f_A \right) = 0 \tag{2.1.7}$$

by use of the initial distribution function $f_A(\vec{v},\vec{x},t)$. If the solution at $t+\Delta t$ is $f_A^*(\vec{v},\vec{x},t)$, then the solution is $f_A^*(\vec{v},\vec{x},t) = f_A\left(\vec{v} - \left(\vec{F}/m_A\right)\Delta t, \vec{x} - \vec{v}\Delta t, t\right)$, and therefore

$$f_A^*(\vec{v}+\Delta\vec{v},\vec{x}+\Delta\vec{x},t) = f_A(\vec{v},\vec{x},t) \tag{2.1.8}$$

where $\Delta\vec{v} = \left(\vec{F}/m_A\right)\Delta t$ and $\Delta\vec{x} = \vec{v}\Delta t$. Equation (2.1.8) implies that the particles of species *A* move according to the equation of motion

$$\begin{aligned} m_A \frac{d\vec{v}}{dt} &= q_A\left(\vec{E} + \vec{v} \times \vec{B}\right) \\ \frac{d\vec{x}}{dt} &= \vec{v} \end{aligned} \tag{2.1.9}$$

These equations of motion are used in PIC simulations which means that the Boltzmann equation without the collision term is that solved by the PIC method. When Equations (2.1.9) are solved for all particles, which is trivial for DSMC since there is no net force, we have $f_A^*(\vec{v},\vec{x},t)$. The second procedure is equivalent to solving

$$\frac{\partial f_A}{\partial t} = \iint \left[f_A(\vec{v}') f_B(\vec{w}') - f_A(\vec{v}) f_B(\vec{w}) \right] g \sigma^{AB} d\Omega d\vec{w} \tag{2.1.10}$$

using the initial distribution function $f_A^*(\vec{v},\vec{x},t)$. The solution of Equation (2.1.10) at $t+\Delta t$ is $f_A(\vec{v},\vec{x},t+\Delta t)$.

Equation (2.1.10), which does not include the term $\partial f_A / \partial x_j$, represents the collisional relaxation of the velocity distribution in a spatially uniform state of species *A*. Equation (2.1.10) can be applied only to a small cell where the gradient of density, temperature, and flow velocity of species *A* can be regarded as uniform. Because of this requirement, the cell dimension should be of the order of the mean free path of species *A,* and is the basis for the cell size of the DSMC method.

A solution of equation (2.1.10) can be obtained by an equivalent stochastic process[33]. First, in particle simulation, it is sufficient to consider the motions of a set of particles randomly sampled from all particles. The sampled particles are referred to as simulated particles. The number of simulated particles in a cell is much smaller than is the number of real particles. The weight, W, is defined as the number of real particles represented by each simulated particle. After moving all simulated particles by Δt, we identify the simulated particles in each cell by examining the positions of the particles. Let N_A be the number of simulated particles in a cell and $\vec{v}_{A1}, \vec{v}_{A2}, \ldots$ be the particle velocities. The velocity distribution function $f_A^*(\vec{v}, \vec{x}, t)$ for a cell located at $\vec{x}$ is expressed as

$$f_A^*(\vec{v}, \vec{x}, t) = \frac{n_A}{N_A} \sum_{i=1}^{N_A} \delta^3\left(\vec{v} - \vec{v}_{A_i}\right) \tag{2.1.11}$$

where n_A is the number density of the cell, $\delta^3(\,)$ is the Dirac delta function, and $\vec{v}_{Ai}$ is the solution of Eq. (2.1.9) at time $t+\Delta t$. The function $\delta^3\left(\vec{v} - \vec{v}_{Ai}\right)$ is the probability density function for the velocity $\vec{v}_{Ai}$ of particle A_i. Similarly, the velocity distribution function of species B at the end of the particle's motion is

$$f_B^*(\vec{w}, \vec{x}, t) = \frac{n_B}{N_B} \sum_{j=1}^{N_B} \delta^3\left(\vec{w} - \vec{v}_{B_j}\right) \tag{2.1.12}$$

where $\vec{v}_{Bi}$ is the velocity of simulated particle B_j. The solution of $f_A(\vec{v}, \vec{x}, t + \Delta t)$ can be obtained from

$$\begin{aligned} f_A(\vec{v}, \vec{x}, t + \Delta t) &= (1 + \Delta t J) f_A^*(\vec{v}, \vec{x}, t) \\ &= f_A^*(\vec{v}, \vec{x}, t) + \Delta t \iint \left[f_A(\vec{v}') f_B(\vec{w}') - f_A(\vec{v}) f_B(\vec{w}) \right] g \sigma^{AB} \, d\Omega \, d\vec{w} \end{aligned} \tag{2.1.13}$$

Substitution of Equations (2.1.11) and (2.1.12) into Equation (2.1.13) yields

$$f_A(\vec{v}, \vec{x}, t + \Delta t) = \frac{n_A}{N_A} \sum_{i=1}^{N_A} f_{A_i}(\vec{v}) \tag{2.1.14}$$

where $f_{Ai}(\vec{v})$ is the probability density function for the velocity of particle A_i at $t+\Delta t$. It is given by

$$f_{A_i}(\vec{v}) = \left(1 - P_{A_i}\right) \delta^3\left(\vec{v} - \vec{v}_{A_i}\right) + P_{A_i} Q_{A_i}(\vec{v}) \tag{2.1.15}$$

The structure of Eq. (2.1.15) states that P_{Ai} is the collisional probability of particle A_i. Note that if $P_{Ai} = 0$, $f_{Ai}(\vec{v}) = \delta^3\left(\vec{v} - \vec{v}_{Ai}\right)$, and there is no change in velocity because of a collision. The probability P_{Ai} is given by

$$P_{A_i} = \sum_{j=1}^{N_B} P_{A_i,B_j} \tag{2.1.16}$$

where

$$P_{A_i,B_j} = N_B^{-1} n_B g_{A_i,B_j} \sigma_T^{AB}\left(g_{A_i,B_j}\right)\Delta t \tag{2.1.17}$$

Here, $g_{Ai,Bj} = \left|\vec{v}_{Ai} - \vec{v}_{Bj}\right|$ is the relative speed and σ_T^{AB} is the total collision cross section. Equation (2.1.16) reveals that $P_{Ai,Bj}$ is the probability of particle A_i colliding with particle B_j in Δt. The function $Q_{Ai}(\vec{v})$ is the probability density function for the post-collision velocity $\vec{v}$. It is written as:

$$Q_{A_i}(\vec{v}) = \sum_{j=1}^{N_B} \frac{P_{A_i,B_j}}{P_{A_i}} Q_{A_i,B_j}(\vec{v}) \tag{2.1.18}$$

Here, the ratio $P_{Ai,Bj}/P_{Ai}$ represents the conditional probability that the collision partner of particle A_i is particle B_j under the condition that particle A_i collides in Δt. Here, $Q_{Ai,Bj}(\vec{v})$ is the probability density function for the post-collision velocity of particle A_i when its collision partner is particle B_j, which is given by:

$$Q_{A_i,B_j}(\vec{v}) = \frac{\sigma^{AB}\left(g_{A_i,B_j},\chi\right)\delta\left(\left|\vec{g}'\right| - g_{A_i,B_j}\right)}{\left(g_{A_i,B_j}\right)^2 M_B^3 \sigma_T^{AB}\left(g_{A_i,B_j}\right)} \tag{2.1.19}$$

where

$$\vec{g}' = \frac{1}{M_B}\left(\vec{v} - M_A \vec{v}_{A_i} - M_B \vec{v}_{B_j}\right) \tag{2.1.20}$$

$M_A = m_A/(m_A+m_B)$, $M_B = m_B/(m_A+m_B)$, χ is the angle between $\vec{g}'$ and $\vec{v}_{Ai} - \vec{v}_{Bj}$, and $\sigma^{AB}(g_{Ai,Bj},\chi)$ is the differential cross section. From Eq. (2.1.19), we have

$$Q_{A_i,B_j}(\vec{v})d\vec{v} = \delta\left(\left|\vec{g}'\right| - g_{A_i,B_j}\right)dg' \frac{\sigma^{AB}\left(g_{A_i,B_j},\chi\right)\sin\chi d\chi d\psi}{\sigma_T^{AB}\left(g_{A_i,B_j}\right)} \tag{2.1.21}$$

where $d\vec{v} = M_B^3 d\vec{g}' = M_B^3 g'^2 dg' \sin\chi d\chi d\psi$. Note that M_B^3 is the Jacobian of the transformation from $\vec{v}$ to $\vec{g}'$, and then Eq. (2.1.20) yields the post-collision velocity $\vec{v}'_{Ai}(\equiv \vec{v})$ of particle A_i

$$\vec{v}'_{A_i} = \frac{1}{m_A + m_B}\left(m_A \vec{v}_{A_i} + m_B \vec{v}_{B_j} + m_B \vec{g}'\right) \tag{2.1.22}$$

where $\vec{g}'\left(= \vec{v}'_{Ai} - \vec{v}'_{Bj}\right)$ is the post-collision relative velocity and $|\vec{g}'| = g_{Ai,Bj}$. The probability that $\vec{g}'$ is included in the solid angle $\sin\chi d\chi d\psi$ is $\sigma^{AB}\left(g_{Ai,Bj},\chi\right)\sin\chi d\chi d\psi / \sigma_T^{AB}\left(g_{Ai,Bj}\right)$. The direction (χ,ψ) of $\vec{g}'$ can be sampled using this probability.

Equations (2.1.16) and (2.1.17), which are derived from the Boltzmann equation, can also be obtained by use of the elementary free-path theory. The collision frequency of particle A_i is

$$\nu_{A_i} = n_B \overline{g_{A_i,B_j}\sigma_T^{AB}\left(g_{A_i,B_j}\right)}$$

where $g_{Ai,B}$ is the relative speed between A_i and some particle B, and the bar denotes the average of particles B. Therefore, the average of all simulated particles B in a cell and the collision probability of particle A_i take the form

$$P_{A_i} = \nu_{A_i}\Delta t = \frac{n_B \Delta t}{N_B}\sum_{j=1}^{N_B} g_{A_i,B_j}\sigma_T^{AB}\left(g_{A_i,B_j}\right)$$

This equation agrees with Equation (2.1.16). We cannot obtain the probability laws to determine the post-collision velocities from the free-path theory, however. In many cases, we can write such probability laws intuitively because the laws derived from the Boltzmann equation agree with the physical image of the collision.

The probability laws used to determine the velocity of particle A_i at $t+\Delta t$ are then:

1) Particle A_i collides in Δt with a probability of P_{Ai}.

2) Under the condition that particle A_i collides, its collision partner is particle B_j with a probability of $P_{Ai,Bj}/P_{Ai}$.

3) If the collision partner is B_j, the post-collision velocity $\vec{v}'_{Ai}$ is given by Equation (2.1.22).

Therefore, the particle simulation method can be derived from the Boltzmann equations of ions and is true for any species. Although the Boltzmann equation for a simple gas is nonlinear because of collisions between like molecules, the simulation method was derived in 1980[34]. Before this work, those in the field of rarefied gas dynamics had regarded the particle simulation method as a kind of numerical experiment. By use of the measure theory, mathematicians[35] verified that Nanbu's particle simulation method is an appropriate method for solving the Boltzmann equation.

The most important ideas of the particle simulation method can be summarized as: 1) decoupling of collisionless motion and collisions; and 2) calculating collisions independently in each cell. These basic concepts have been shown to naturally result from the operator splitting in the form of $(1+\Delta tJ)(1+\Delta tD)$. Now consider the conditions for choosing Δt. The operator splitting is allowed if and only if $\Delta t\left|J\left(f_A\right)\right| \ll f_A$ and $\Delta t\left|D\left(f_A\right)\right| \ll f_A$. The first condition states that the effect of collisions in Δt must be small; therefore the collision probability $P_{Ai} \simeq \Delta t / \tau$ is small, where τ is the mean free time. The time step must satisfy the condition $\Delta t \ll \tau$. The second condition requires that $|\Delta \mathbf{x}| \ll |x|$ and $|\Delta \mathbf{v}| \ll |v|$ in Eq. (2.1.8). That is, $\bar{v}\Delta t \ll x$ and $\left(\bar{F} / m_A\right)\Delta t \ll \bar{v}$, where $\bar{v}$ is the mean particle speed and $\bar{F} / m_A$ is the mean acceleration. The condition that $\bar{v}\Delta t \ll x$ is usually replaced by the Courant condition $\bar{v}\Delta t < \Delta_c$, where Δ_c denotes the cell size. Therefore, a particle's displacement in Δt must be less than the cell size. The condition $\left(\bar{F} / m_A\right)\Delta t \ll \bar{v}$ requires that the change in the particle's speed in Δt must be much less than the original speed for PIC simulations. Therefore, a smaller Δt should be used for an external field.

2.2 Traditional Direct Simulation Monte Carlo Methods

The DSMC technique was developed primarily by Graeme Bird, now Emeritus Professor at the University of Sydney, Australia, nearly a half century ago. Since its inception, this technique has been used in many different applications ranging from the simulation of micro-electromechanical devices (MEMs), to various industrial and pharmacological deposition simulations, to the simulation of (re)entry and other rarefied flow fields.

In the work outlined herein, the DSMC method is used to simulate the Boltzmann equation for rarefied/transitional reentry flows in which the Navier-Stokes equations are not valid throughout the entire flow field. Specifically, the algorithm employed is the DSMC Analysis Code (DAC)[36, 37], which was developed by a team led by LeBeau beginning at the NASA Langley Research Center and continuing at the NASA Johnson Space Center. The DSMC algorithms in the release version of DAC are based on those developed by Bird[2].

Regardless of the DSMC code used, the basic structure of the algorithm is the same. The following is included to briefly describe the flow of a generic DSMC algorithm.

2.2.1 Collision Algorithm

In each computational cell, particles are chosen to collide in such a way as to reproduce the required macroscopic collision rate. The simplest implementation of collision pair selection is to disregard particle position within the cell when selecting the pair. This methodology restricts the size of a computational cell in that it must be smaller than the local average mean free path of the flow field. This was the first selection methodology and is still utilized today. The next selection methodology

was to select the first particle randomly in the cell and then select the particle closest to the first excluding its previous collision partner, or the so-called virtual sub-cell (VSC) algorithm of LeBeau[38]. This methodology allows for a larger collision cell size as long as the resulting mean collision distance divided by mean free path remains at least as small as the resulting value from the original selection methodology. Other selection methodologies have been proposed[39, 40], but the two discussed above are the most prevalent. The VSC algorithm is that which was used in the current study.

In many modern DSMC codes, Bird's No Time Counter (NTC) method is used to select colliding pairs[2]. At each time step and in each computational cell, the number of particle pairs to be tested for collisions is calculated as follows:

$$N_{coll} = \tfrac{1}{2} n \bar{N} \left(\sigma_T g\right)_{\max} \Delta t \tag{2.2.1}$$

where n is the number density of gas particles in the cell, $\bar{N}$ is the average number of simulator particles in the cell, Δt is the simulation time step, g is the relative velocity of a colliding pair of particles, and σ_T is the total collision cross section of the colliding pair. Each of these pairs are then selected to collide if the probability:

$$P_{coll} = \frac{\left(\sigma_T g\right)}{\left(\sigma_T g\right)_{\max}} \tag{2.2.2}$$

is less than a random number uniformly distributed between zero and one. This method assumes that the collision rates between species will be implicitly reproduced, even though all species are lumped into the same group for the pair selection process. This method can become inefficient if the product of the collision cross section and relative velocity becomes very much different between species pairs, as is the case when electrons are introduced into the flow, because the maximum value of $\sigma_T g$ is very large and results in many null collisions. This is the basic algorithm used by the DAC code.

In order to address this issue, the collision algorithm in DAC was modified as follows[31]. The collision algorithm can be divided into two groups. One includes collisions between similar particles, and the other collisions between dissimilar particles. The collision term of the Boltzmann equation is nonlinear for like collisions and linear for unlike collisions. Consequently, the collision algorithm for like collisions is different from that for the unlike collisions.

There are five classes of collisions involving charged particles: electrons with neutrals, ions with neutrals, electrons with ions, ions with ions, and electrons with electrons. The interactions of the last three classes obey the Coulomb force law:

$$F = \frac{1}{4\pi\varepsilon_0} \frac{q_1 q_2}{r^2} \tag{2.2.3}$$

where ε_0 is the permittivity of free space and *r* is the distance between the particles. Bird[41] and Taylor *et. al.* [25], however, used the variable hard sphere (VHS) model of Bird to describe the first four classes of collisions by setting the diameter of the heavy ions equal to the diameter of their neutral counterparts. The reference diameter of the electrons is set equal to 1e-10 m, which is orders of magnitude larger than the classical value of 6e-15 m. This choice was somewhat arbitrary, but Bird did mention that the electron diameter was varied in his simulations by a factor of three with no significant effect on the flow field parameters. Neither modeled electron-electron collisions. This is the approach that will be followed herein.

In general, then, one can divide the collision algorithm into two for weakly ionized plasmas, neglecting Coulomb collisions: 1) collisions between unlike particles; and 2) collisions between like particles. The algorithm for type (1) is derived from the linear Boltzmann equation as in Section 2.1.1, and that for type (2) is from the nonlinear Boltzmann equation.

Let us consider the elastic collisions:

$$A(\vec{v}_A) + B(\vec{v}_B) \rightarrow A(\vec{v}_A') + B(\vec{v}_B')$$

If gas *B* is at rest and in equilibrium at temperature T_B, the probability that particle *A* elastically collides with some particle *B* is:

$$P_{coll} = n_B \overline{g\sigma_T(g)}\Delta t \tag{2.2.4}$$

where n_B is the number density of gas *B*, $g = |\vec{v}_A - \vec{v}_B|$ is the relative velocity, and the average is taken over the Maxwellian distribution of $\vec{v}_B$. The average in Equation(2.2.4) is for all simulated particles in the cell, which gives:

$$P_{coll} = \frac{n_B}{N_B}\sum_{j=1}^{N_B} g_j \sigma_T(g_j)\Delta t \tag{2.2.5}$$

where N_B is the number of simulated *B* particles. If the collision is treated by the hard-sphere model, the scattering is isotropic. The post-collision velocities are then:

$$\begin{aligned}\vec{v}_A' &= \frac{1}{m_A + m_B}\left(m_A\vec{v}_A + m_B\vec{v}_B + m_B|\vec{v}_A - \vec{v}_B|\vec{R}\right)\\ \vec{v}_B' &= \frac{1}{m_A + m_B}\left(m_A\vec{v}_A + m_B\vec{v}_B - m_A|\vec{v}_A - \vec{v}_B|\vec{R}\right)\end{aligned} \tag{2.2.6}$$

where the two *R*'s are the same unit vector with a random direction. However, the hard sphere model is generally insufficient for most applications because it does not match the gas's viscosity or diffusion rate as a function of temperature. On the other hand, the most accurate Lennard-Jones potential is not suited for the DSMC method

because the collision calculation is very time-consuming. But, the simple inverse-power potential $V(r) = a/r^{\alpha}$ is sufficiently accurate and very efficient for collision calculations. The differential cross section σ for the inverse-power potential takes the form:

$$\sigma = Ag^{-4/\alpha} \tag{2.2.7}$$

where g is the relative speed and A is a function of the deflection angle χ. If A is independent of χ, the probability $\sigma\, d\Omega/\sigma_T$ that the post-collision relative velocity is directed into the solid angle $d\Omega$ becomes $d\Omega/4\pi$, or the scattering is isotropic and the post-collision velocities are the same as that of the hard-sphere model. The variable hard-sphere (VHS) model was proposed by Bird[41] to avoid the divergence of the total collision cross section and using isotropic scattering for the inverse-power potential. In the VHS model, the coefficient A is constant and, once a gas is selected, A and α can be chosen to best fit the Chapman-Enskog viscosity to experimental data. This leads to a power law temperature dependence of the coefficient of viscosity such that:

$$\mu \propto T^{\omega} \tag{2.2.8}$$

where

$$\omega = \frac{\alpha + 4}{2\alpha} \tag{2.2.9}$$

and ω is bounded by 0.5 and 1.0 at the hard-sphere and Maxwell molecule limits, respectively. The VHS parameters used in the current study are discussed in Section 5.3.

2.2.1.1 Simple Gas

For a single species gas in a computational cell, let $\vec{v}_1, \vec{v}_2, \ldots, \vec{v}_N$ be the velocities of the simulated particles. The probability P_i that molecule i collides in Δt with some other particle is given by Equation (2.2.5). For a simple gas, this is:

$$P_i = \frac{n}{N}\sum_{j=1}^{N} g_{ij}\sigma_T\left(g_{ij}\right)\Delta t = \sum_{j=1}^{N} P_{ij} \tag{2.2.10}$$

where $g_{ij} = \vec{v}_i - \vec{v}_j$ and

$$P_{ij} = N^{-1} n g_{ij}\sigma_T\left(g_{ij}\right)\Delta t \tag{2.2.11}$$

Note that $P_{ii} = 0$ because $g_{ii} = 0$. The term for $j = i$ should therefore be omitted in Equation (2.2.10).

If g_{ij} is then replaced by g_{max}, the resulting probability is:

$$\left(P_{ij}\right)_{\max} = N^{-1} n g_{\max} \sigma_T \left(g_{\max}\right) \Delta t \tag{2.2.12}$$

This probability is greater than P_{ij}. For $P_{ij} = (P_{ij})_{max}$, Equation (2.2.10) takes the form:

$$\left(P_i\right)_{\max} = n N^{-1} \left(N-1\right) g_{\max} \sigma_T \left(g_{\max}\right) \Delta t \tag{2.2.13}$$

The number of collisions in Δt for $(P_i)_{max}$ is

$$N_{\max} = \tfrac{1}{2} \sum_{i=1}^{N} \left(P_i\right)_{\max} = \tfrac{1}{2} n \left(N-1\right) g_{\max} \sigma_T \left(g_{\max}\right) \Delta t \tag{2.2.14}$$

The factor of ½ on the right hand side of Equation (2.2.14) is to avoid double counting collisions between like particles. N_{max} is called the maximum collision number. The computing time necessary to obtain the real collision number

$$N_{coll} = \tfrac{1}{2} \sum_{i=1}^{N} \sum_{j=1}^{N} P_{ij} \tag{2.2.15}$$

is proportional to N^2. This is not insignificant because collisions in all cells in a computational domain must be calculated at each time step. In the null-collision method, the task is avoided by regarding N_{max} as the collision number in Δt. To compensate for excess collisions, N_{max}-N_c, some of the N_{max} collisions are regarded as null collisions. We now define:

$$P_{ij} = \left(P_{ij}\right)_{\max} q_{ij} \tag{2.2.16}$$

where $q_{ij} = g_{ij} \sigma_T \left(g_{ij}\right) \Big/ g_{\max} \sigma_T \left(g_{\max}\right)$. This means that the pair (i,j) first makes a tentative collision with a probability of $(P_{ij})_{max}$. The tentative collision results in a real collision with a probability of q_{ij} and a null collision with a probability of 1-q_{ij}. The number of tentative collisions is $(P_{ij})_{max}$ times the number of pairs $N(N\text{-}1)/2$; the product is equal to N_{max}. A tentative collision pair can be chosen randomly because $(P_{ij})_{max}$ is common to all (i,j). So, to summarize, we first obtain N_{max}. In general, N_{max} is not an integer. Let $p = N_{\max} - \lfloor N_{\max} \rfloor$, where $\lfloor N_{\max} \rfloor$ is the integral part of N_{max}. We then set $N_{\max} = \lfloor N_{\max} \rfloor + 1$ with a probability of p and $N_{\max} = \lfloor N_{\max} \rfloor$ with a probability of 1-p. The following two steps are then repeated N_{max} times:

1. Choose a pair (i,j) of $i \neq j$ randomly and obtain q_{ij}.

2. Call a random number U. If $U < q_{ij}$, the pair collides. If they do collide, the pre-collision velocities are replaced by the post-collision velocities given in Equation (2.2.6) where the particles A and B are of the same kind.

2.2.1.2 Gas Mixture

For the sake of simplicity, consider a binary mixture of species A and B. The types of collisions are A-A, B-B, and A-B. The A-B collision is a collision between unlike particles. The other two types are treated as in the gas of a simple gas above. Let N_A and N_B be the numbers of simulated particles A and B in the cell. The probability that molecule A_i collides with some molecule B in Δt is

$$P_{A_i} = n_B \overline{g\sigma_T^{AB}} \Delta t \tag{2.2.17}$$

where g is the relative speed and σ_T^{AB} is the total cross section for the A-B collision. The average is for all simulated molecules B in the cell, so the probability takes the form:

$$P_{A_i} = \sum_{j=1}^{N_B} P_{A_i,B_j} \tag{2.2.18}$$

where

$$P_{A_i,B_j} = N_B^{-1} n_B g_{A_i,B_j} \sigma_T^{AB} \Delta t \tag{2.2.19}$$

If we again introduce the idea of the maximum collision number where $g_{Ai,Bi}$ is replaced by $g_{\max}^{AB}$, we have the upper bound of $P_{Ai,Bi}$:

$$P_{\max}^{AB} = N_B^{-1} n_B g_{\max}^{AB} \sigma_T^{AB} \left(g_{\max}^{AB} \right) \Delta t \tag{2.2.20}$$

The maximum number of A-B collisions in Δt for $P_{\max}^{AB}$ is

$$N_{\max}^{AB} = \sum_{i=1}^{N_A} P_{\max}^{AB} = \sum_{i=1}^{N_A} \sum_{j=1}^{N_B} P_{\max}^{AB} \tag{2.2.21}$$

Note that the factor of ½ is not necessary for A-B collisions. Substitution of Eq. (2.2.20) into Eq. (2.2.21) gives us:

$$N_{\max}^{AB} = n_B N_A g_{\max}^{AB} \sigma_T^{AB} \left(g_{\max}^{AB} \right) \Delta t \tag{2.2.22}$$

The number density n_B is expressed as:

$$n_B = \frac{W N_B}{V_c} \tag{2.2.23}$$

where V_c is the cell volume and W is the weight. As discussed previously, one simulated particle represents W real particles. Presently, assume that all the particles in a cell have a common weight. The collision procedure in the previous section is then repeated for all species combinations *A*-*A*, *A*-*B*, and *B*-*B* using the updated definitions of number of collisions and probabilities for like and unlike collision pairs as required.

2.2.2 Internal Degrees-of-Freedom

A typical application of the DSMC method involves the calculation of many billions of intermolecular collisions, and this leads to the requirement for computationally simple molecular models. This has led to the development of "phenomenological" models that focus on the generation of accurate results for the observed gas properties but do not attempt to provide the most realistic model of individual collisions at the microscopic level[13]. The developers of classical kinetic theory faced a similar problem in that they required mathematically tractable molecular models that permitted the derivation of analytical expressions for the macroscopic transport properties. The classical models were the obvious choice for early DSMC work, but were found to have serious shortcomings that have been overcome by phenomenological models that have been introduced in the context of the DSMC method.

We have already seen a phenomenological model be applied to elastic collisions by way of the variable hard sphere model, which combines the unrealistic but simple isotropic scattering of a hard sphere with a realistic variation of diameter with the relative speed of the collision pair. This model leads to accurate results for viscosity and heat conduction coefficients.

In the same way, classical kinetic theory did not lead to any useful models for inelastic collisions. For example, the rough sphere model retains the deficiencies of the hard sphere model with regard to the transport properties, and it is unable to deal with the quantum effects that cause most gases to have fewer than three rotational degrees of freedom and has a fixed and unrealistically fast rotational relaxation time. This problem was solved in the context of the DSMC method by the introduction of the Larsen-Borgnakke, or L-B, model[42] for rotation which can be regarded as the archetypal phenomenological procedure. It is an add-on to the VHS model and, for a fraction of the collisions that are chosen to match measured rotational relaxation rates, the post-collision rotational energies are selected from the equilibrium distribution that correspond to the collision energy. The L-B model was extended to the vibrational modes, but it assumed that the internal energies were continuously distributed and was found lacking. The situation was corrected by the introduction[43] of the quantum version of the L-B model.

DSMC methods test colliding particles for possible internal energy exchanges or chemical reactions. The collision selection rules use probabilities that must be defined such that they result in the desired macroscopic relaxation rate behavior. This typically involves identifying a macroscopic rate equation that the simulation

attempts to match through appropriate definitions of selection probabilities *P*. These rate equations often contain parameters such as collision numbers *Z*, characteristic times τ, or rate coefficients that are estimated from experiments or analysis. Ambiguity regarding specific definitions of the targeted macroscopic rates and coefficients has often led to confusion in defining the appropriate selection probabilities in DMSC methods.

In studies of vibrational relaxation, Haas[44] developed a relationship between the appropriate DSMC selection probability *P* and the resulting Landau-Teller macroscopic relaxation behavior. This relationship was later generalized, allowing for rotational relaxation, by Lumpkin *et al*.[45] in the form of a "correction factor" for collision numbers *Z*. It was observed that the DSMC probabilities *P*, in general, cannot be specified by the assumption *P=1/Z*, which has been employed throughout the DSMC community. Dissimilar applications of the selection probability and incompatible definitions of collision number led to disagreement among DSMC researchers regarding these correction factors.

Haas *et al*.[46] went on to clarify the definitions of macroscopic rate parameters employed in rotational relaxation, including differing interpretations of Jeans' equation[47]. It was shown that relaxing energies, when plotted against the cumulative number of molecular collisions, lead to a single solution, regardless of the assumed intermolecular potential in an adiabatic bath. Differing definitions of collision time τ_c between experiments and DSMC were clarified. The two most widely used selection methodologies were discussed, and DSMC rotational relaxation probabilities *P*, specific to each methodology, were derived to match the macroscopic rate equations exactly. Prevalent selection methods cannot reproduce Jeans' equation exactly for the case of heteromolecular collisions, nor can they reproduce Jeans' and Landau-Teller[48] rate behavior for simultaneous rotational and vibrational relaxation. Thus, a new selection methodology was introduced that was better suited to the general case of gas mixtures experiencing multimode internal energy relaxation. Although constant *Z* values were used, the developments were valid for variable *Z* as well.

Gimelshein *et al*.[49, 50] proposed a simplified inelastic collision algorithm using particle selection prohibiting multiple relaxations. They felt that the selection methodology proposed by Haas[46] lead to an unnecessarily complicated functional dependence between the probability and the collision number. To avoid the complexity, a straightforward selection methodology was developed which also resulted in relaxation behavior matching the Landau-Teller equation when the correct correction factor was used.

Gimelshein *et al*.[50] took a closer look at vibrational relaxation and derived an exact relationship that connects the vibrational relaxation number, Z_{vib}^{DSMC}, used in the DSMC method and that employed in continuum simulations. An approximate expression for Z_{vib}^{DSMC} was also derived that is cost-effective and applicable when translational temperature is larger than the vibrational temperature.

2.2.2.1 Rotational and Vibrational Energy Transfer

Models for rotational and vibrational energy transfer with translational energy in a collision have been explored previously. The Larsen-Borgnakke (L-B) model[42] is usually used to describe the rotational and vibrational energy transfer in the DSMC method. A fraction of the total number of collisions, $1/Z_{vib}$ or $1/Z_{rot}$, lead to the energy exchange, where Z_{vib} and Z_{rot} are the vibrational and rotational collision numbers, respectively. Originally, the internal energy modes were treated as continuous. These energy modes are, of course, discrete. To address this issue, Bergemann and Boyd introduced the algorithms of the L-B model with discrete vibrational and rotational energy levels for diatomic molecules[43, 51]. Gimelshein *et al.* then extended the L-B model for the case of polyatomic gas mixtures with discrete vibrational and rotational energies[49].

The temperature dependent nature of rotational and vibrational relaxation rates has been developed by Parker[52] and Millikan and White[53], which provides the characteristic relaxation times as functions of the temperature for a wide range of pure and mixed diatomic gases. In the L-B model, the vibrational and rotational post-collision energies are modeled according to the local equilibrium distribution functions. The derivation of these models for application in the DSMC method can be viewed in Reference [2], but the vibrational relaxation model resulting from Millikan and White, which is used in this study, is:

$$Z_{vib} = \left(\frac{C_1}{T^{\omega}} \right) \exp\left(C_2 T^{-1/3} \right) \tag{2.2.24}$$

where C_1 and C_2 are constants used to fit the experimental data.

However, these lead to the incorrect macroscopic relaxation rate. Lumpkin and Haas *et al.*[45, 46] introduced a correction factor for the rotational relaxation rate in the DSMC method. Most continuum analyses and computational codes use Jeans' equation[47] to model rotational relaxation. In a single species gas, Jeans' equation uses the instantaneous equilibrium rotational energy $E_{rot}^{*}(t)$ and a time constant, which can be written as the product of the instantaneous collision time τ_c and a characteristic collision number Z as:

$$\frac{dE_{rot}}{dt} = \frac{E_{rot}^{*}(t) - E_{rot}(t)}{\tau_c Z_r^{cont}} \tag{2.2.25}$$

where E_{rot} is the mean rotational energy per molecule in the ensemble, and t represents time. Denoting the rotational degrees of freedom by ζ_{rot}, E_{rot}^{*} is defined by:

$$E_{rot}^{*} = \frac{\zeta_{rot}}{2} kT \tag{2.2.26}$$

and will change with time as the translational temperature T varies during relaxation under adiabatic conditions. Similarly, τ_c may vary with T, depending upon the intermolecular potential assumed for the gas. Most DSMC methods employ the VHS model, which assumes rigid-sphere collision mechanics, but establishes the collision rate in a manner consistent with an inverse-power potential. The relative translational energy of colliding particles near equilibrium, as a result of biasing due to collision selection, is distributed with ζ_{trans} degrees of freedom given by:

$$\zeta_{trans} = 4 - \frac{4}{\alpha} = 5 - 2\omega \tag{2.2.27}$$

Note that this can differ from $\zeta_T = 3$ associated with the translational energy of an equilibrium ensemble of particles in a reservoir. Biasing from collision selection plays a significant role in the relaxation of the energy in a reservoir and becomes apparent in the derivation of the relaxation probability. Haas[46] derived the relationship for the particle selection method for a single species gas (allowing for multiple relaxation) as:

$$P_{part}^{DSMC} = \left(\frac{\zeta_T + 2\zeta_{rot}}{2\zeta_{rot}} \right) \left[1 - \sqrt{1 - \left(\frac{\zeta_{rot}}{\zeta_T} \right) \left(\frac{\zeta_T + \zeta_{rot}}{\zeta_T + 2\zeta_{rot}} \right) \frac{4}{Z_{rot}^{cont}}} \right] \tag{2.2.28}$$

that correctly reproduced the relaxation rate given by Jeans' equation. He goes on to say that $P_{part} = 1/Z$ could be a fair assumption for adiabatic relaxation, but only if one redefined Z by using adiabatic relaxation data that has been cast into the isothermal form of Jeans' equation as suggested by Bird[2]. As such for adiabatic flows, $P_{part} = (1/Z_{Bird}) = (1/Z)(1+\zeta_{rot}/\zeta_T)$ can be a fair assumption to the exact expression. Better yet, the probabilities were shown to approach asymptotic limits described by:

$$P_{part}^{DSMC} = \left(1 + \frac{\zeta_{rot}}{\zeta_T} \right) \frac{1}{Z_{rot}^{cont}} \tag{2.2.29}$$

which represents an excellent approximation when $Z > 10$ for the particle-selection methodology.

Gimelshein[50] then analyzed the vibrational relaxation rates in the DSMC method. The main difference between rotation-translation and vibration-translation relaxation is that while the rotational mode can be describes as having a constant number of degrees-of-freedom at all temperatures except cryogenic, the number of vibrational degrees-of-freedom varies with the temperature. For a simple harmonic oscillator, the number of vibrational degrees-of-freedom ζ_{vib} is:

$$\zeta_{vib} = \frac{2\Theta_{vib}/T}{\exp\left(\Theta_{vib}/T\right) - 1} \tag{2.2.30}$$

where Θ_{vib} is the characteristic vibrational temperature of the mode. This means that the relationship for rotational relaxation probability given above are not applicable to the vibration-translation energy transfer. Gimelshein derives the relationships that allow one to match the vibrational relaxation rate in DSMC with that predicted by the Landau-Teller equation[48]:

$$\frac{dE_{vib}}{dt} = \frac{E_{vib}^{*}(t) - E_{vib}(t)}{\tau_{coll} Z_{vib}^{cont}} \tag{2.2.31}$$

where t is again time, E_{vib} is the mean vibrational energy per molecule in the ensemble, and E_{vib}^{*} is the instantaneous equilibrium vibrational energy, defined as:

$$E_{vib}^{*} = \frac{\zeta_{vib}(T_{trans})}{2} kT_{trans} \tag{2.2.32}$$

He goes on to derive the expression for the DSMC collision number for vibration as:

$$P_{vib}^{DSMC} = \frac{\zeta_{vib}(T_{trans})T_{trans} - \zeta_{vib}(T_{vib})T_{vib}}{\zeta_T (T_{trans} - T')} \frac{1}{Z_{vib}^{cont}} \tag{2.2.33}$$

The probability of a vibrationally inelastic collision in the DSMC method is then $P = 1/Z_{vib}^{cont}$. Although exact, Equation (2.2.33) is costly for direct use in DSMC computations because it involves the calculation of the vibrational and translational temperatures, and then the subsequent numerical determination of *T'* (post collisional temperature). However, the exact expression can be significantly simplified when the vibrational and translational temperatures are close:

$$\begin{aligned} P_{vib}^{DSMC} &\approx \frac{\zeta_T + A}{\zeta_T} \frac{1}{Z_{vib}^{cont}} \\ A &= \tfrac{1}{2}\zeta_{vib}^{2}(T)\exp(\Theta_{vib}/T) \end{aligned} \tag{2.2.34}$$

The above equation is applicable only when the difference between the vibrational and translational temperatures is small. However, it was found that if the translational temperature is used as *T*, Equation (2.2.34) reproduced well the correct expression in Equation (2.2.33) for all cases where the vibrational temperature was lower than the translational one.

2.2.2.2 Electronic Energy Levels

In the past, Bird[15] and Carlson *et al.*[17, 25] modeled electronically excited levels and electronic transitions in DSMC. In their work, each excited particle was assigned a distribution over all available states, assuming that the electronic energy mode was in equilibrium. Gallis and Harvey[16, 54] modeled non-equilibrium thermal radiation in DSMC as well as electronic excitation processes. However, for their method, accurate cross sections for electronic excitation and absorption were required and the

uncertainty in the cross sections is not well known for all the species. Because of these deficiencies, a much more accessible non-equilibrium electronic energy model is developed in this thesis in Section 3.1.

2.2.2.3 Selection Methodology

Haas[46] derives the relationship for a versatile L-B selection methodology that is applicable to gas mixtures and is adapted from the particle-selection method; probability, P, is applied to each molecule individually within the colliding pair, but the event in which both particles relax is prohibited (called particle-selection prohibiting double relaxation). This ensures that relaxation of A molecules is independent of the energy of B molecules, and the L-B mechanics can therefore reproduce the relaxation rate behavior for each species independently. The appropriate functional form for the relaxation probability was defined as:

$$\tfrac{1}{2}P_{A|B}^2 - \left(\frac{\zeta_{T_{A|B}} + \zeta_{r_A}}{2\zeta_{T_{A|B}}} \frac{1}{Z_{A|B}} - \frac{\zeta_{T_{A|B}} + \zeta_{r_B}}{2\zeta_{T_{A|B}}} \frac{1}{Z_{B|A}} + 1 \right) P_{A|B} + \frac{\zeta_{T_{A|B}} + \zeta_{r_A}}{\zeta_{T_{A|B}}} \frac{1}{Z_{A|B}} = 0 \quad (2.2.35)$$

where the Z values are from continuum methods. This expression involves only rotational energy exchange. The expression for multimode energy relaxation is presented by Haas[46], and the reader is referred to the reference for the complete derivation.

Gimelshein[49, 50] believed that, although correct, the above selection methodology leads to an unnecessarily complicated functional dependence between the probability and the collision number. This is especially true when multi-mode relaxation is considered. To avoid the complexity, a straightforward selection methodology was used that is illustrated in Figure 2.1. The first step is to select a random number Rn uniformly between 0 and 1. Then, using the value of Rn, the possible relaxation events are tested, so that either rotational or vibrational relaxation may occur for particle A or particle B. Multiple relaxation events are prohibited.

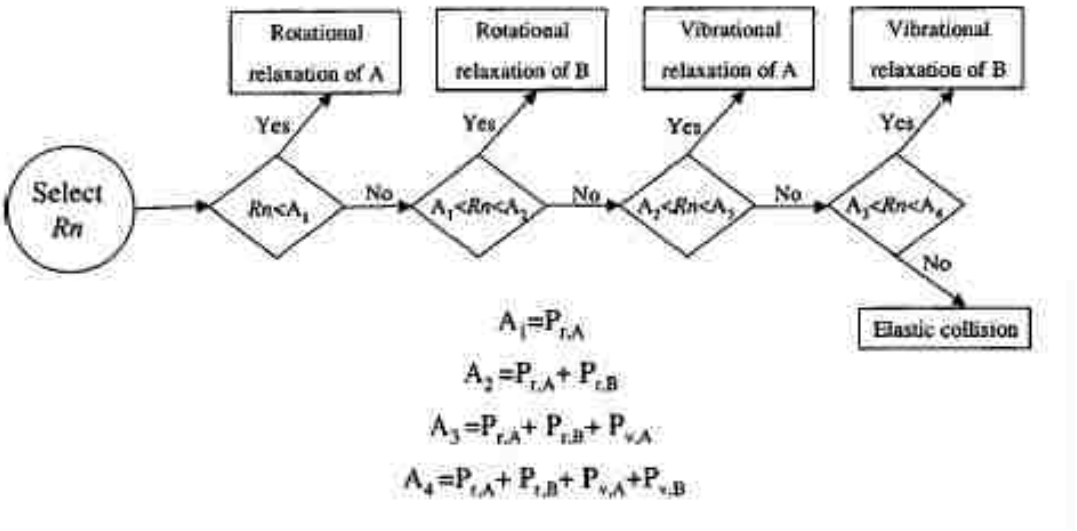

Figure 2.1: Selection methodology for inelastic and elastic collisions.

Similar to that suggested by Haas, the simplified selection methodology allows only one relaxation event to take place in a collision. Vibrational and rotational relaxation rates of different species in the gas mixture are independent, and the necessary relaxation rates may also be accurately captured. It can be easily implemented and is characterized by a simpler dependence between the collision numbers and the relaxation probabilities. This method should not be applied when the total probability of internal-translational energy exchange is larger than unity. If the sum of the probabilities is greater than unity, an alternative methodology is implemented as shown in Figure 2.2. These selection methodologies are easily updated to include electronic energy exchange.

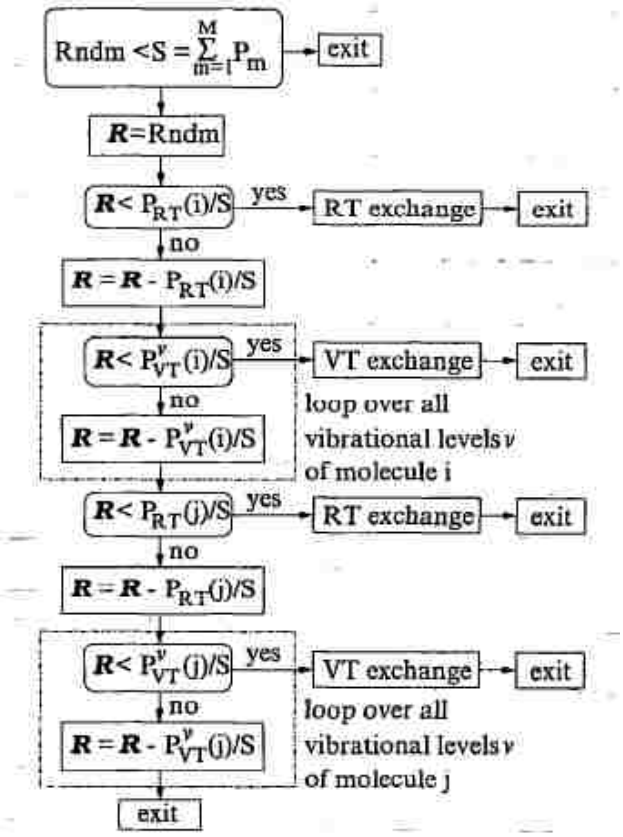

Figure 2.2: Selection methodology for inelastic collisions if the sum of the probabilities is greater than unity.

2.2.3 Chemical Reactions

Once the collision partners have been selected as described in Section 2.2.1, they are then tested to see if a chemical reaction will occur. A typical bimolecular reaction may be written as:

$$A + B \leftrightarrow C + D$$

As long as the reaction takes place in a single step with no species other than the reactants present, it has been found that the rate equation for the change of concentration of species A may be written:

$$-\frac{dn_A}{dt} = k_f(T) n_A n_B - k_r(T) n_C n_D \tag{2.2.36}$$

The rate coefficients are functions of temperature and are independent of the number densities and time. A further result that originally had an empirical basis is that the rate coefficients are of the form:

$$k_f = aT^b \exp\left(-\frac{E_a}{kT}\right) \tag{2.2.37}$$

where a and b are constants and E_a is called the activation energy of the reaction.

The Total Collision Energy (TCE) model[55] of Bird was developed in order to obtain a rate coefficient based on a chemical reaction cross section which takes the form:

$$\sigma_{react} = \begin{cases} 0 & if\ E_{coll} < E_a \\ \sigma_T C_1 \left(E_{coll} - E_a\right)^{C_2} \left(1 - \frac{E_a}{E_{coll}}\right)^{\bar{\zeta}+3/2-\omega_{AB}} & if\ E_{coll} > E_a \end{cases} \tag{2.2.38}$$

where C_1 and C_2 are constants, E_{coll} is the collision energy available to the reaction, and $\bar{\zeta}$ is the average number of internal degrees of freedom that contribute to the collision energy. The resulting rate coefficient becomes:

$$k(T) = \frac{2C_1\sigma_{ref}}{\pi^{1/2}\varepsilon}\left(\frac{2kT_{ref}}{m_r}\right)^{1/2} \frac{\Gamma\left(\bar{\zeta}+C_2+5/2-\omega_{AB}\right)}{\Gamma\left(\bar{\zeta}+b+3/2\right)} \frac{k^{C_2}T^{C_2+1-\omega_{AB}}}{T_{ref}^{1-\omega_{AB}}} \exp\left(-\frac{E_a}{kT}\right) \tag{2.2.39}$$

where the constants C_1 and C_2 are:

$$\begin{aligned} C_1 &= \frac{\pi^{1/2}\varepsilon a T_{ref}^b}{2\sigma_{ref}} \frac{\Gamma\left(\bar{\zeta}+5/2-\omega_{AB}\right)}{\Gamma\left(\bar{\zeta}+b+3/2\right)} \left(\frac{m_r}{2kT_{ref}}\right)^{1/2} \frac{T_{ref}^{1-\omega_{AB}}}{k^{b-1+\omega_{AB}}} \\ C_2 &= b-1+\omega_{AB} \end{aligned} \tag{2.2.40}$$

The probability of the reaction then occurring at each collision with $E_c > E_a$ between power-law VHS particles is then:

$$P_{react} = \frac{\sigma_R}{\sigma_T} = \frac{\pi^{1/2}\varepsilon a T_{ref}^b}{2\sigma_{ref}\left(kT_{ref}\right)^{b-1+\omega_{AB}}} \frac{\Gamma\left(\bar{\zeta}+5/2-\omega_{AB}\right)}{\Gamma\left(\bar{\zeta}+b+3/2\right)} \left(\frac{m_r}{2kT_{ref}}\right)^{1/2} \frac{\left(E_{coll}-E_a\right)^{b+\bar{\zeta}+1/2}}{E_{coll}^{\bar{\zeta}+3/2-\omega_{AB}}} \tag{2.2.41}$$

The same can be done for termolecular, dissociation/recombination reactions represented as:

$$AB + T \leftrightarrow A + B + T$$

where AB is the dissociating molecule and T is the third body particle. The rate of formation of either species A or B in the forward reaction can be written:

$$\frac{dn_A}{dt} = k_f n_{AB} n_T \tag{2.2.42}$$

while the loss of species A in the reverse reaction is

$$\frac{dn_A}{dt} = k_r n_A n_B n_T \tag{2.2.43}$$

The corresponding reaction probability for the forward dissociation reaction is the same as that in Equation (2.2.41) and the probability of a recombination can be written:

$$P_{react} = \frac{\sigma_{react}}{\sigma_T} = \frac{\pi^{1/2} n_T \varepsilon a T_{ref}^b}{2\sigma_{ref}} \frac{\Gamma\left(5/2 - \omega_{AB}\right)}{\Gamma\left(b + 3/2\right)} \left(\frac{m_r}{2kT_{ref}}\right)^{1/2} \left(\frac{E_{coll}}{kT_{ref}}\right)^{b-1+\omega_{AB}} \tag{2.2.44}$$

where the activation energy and, therefore, contributing internal degrees of freedom are taken as zero.

These are the typically implemented set of probabilities for both forward and reverse reactions in DSMC codes. They require available data for each forward and reverse reaction. However, these data are not always readily available for the reverse reactions. Also, many CFD codes make use of statistical mechanics in order to specify the reverse reaction rate. If comparisons are to be made to CFD results, it follows that the DSMC code should use statistical mechanics to obtain the reverse reaction rate where data are not available. This methodology is not used in general where data are available because the reaction probabilities are functions of the macroscopic temperature, which is less physically realistic than the dependence on the collision energy for the forward reactions. Another use of statistical mechanics is to calculate the reverse reaction rate from the forward reaction data, and then choose the relevant coefficients from the available reverse reaction data to most closely match the rate computed from statistical mechanics. The following modifications were implemented in the DAC software for those reverse reactions where data were unavailable.

Chemical equilibrium requires a balance between the forward and reverse reactions such that the concentrations of all species remain constant with time. Therefore, for a bimolecular reaction,

$$K_{eq} \equiv \frac{k_f}{k_r} = \frac{n_C n_D}{n_A n_B} \tag{2.2.45}$$

where K_{eq} is the equilibrium constant. Similarly, the equilibrium constant for the termolecular dissociation-recombination reaction is written as:

$$K_{eq} \equiv \frac{k_f}{k_r} = \frac{n_A n_B}{n_{AB}} \tag{2.2.46}$$

Equilibrium statistical mechanics relates the numbers of the various species in a system to the partition functions. For the bimolecular reaction,

$$\frac{N_C N_D}{N_A N_B} = \frac{Q^C Q^D}{Q^A Q^B} \exp\left(-\frac{E_a}{kT}\right) \tag{2.2.47}$$

where Q is the partition function for the species that is indicated by the superscript, and E_a should be interpreted as the difference between the forward and reverse activation energies. The number N is related to the volume V of the system by $N = nV$, which results in the bimolecular equilibrium constant written as:

$$K_{eq} \equiv \frac{k_f}{k_r} = \frac{n_C n_D}{n_A n_B} = \frac{Q^C Q^D}{Q^A Q^B} \exp\left(-\frac{E_a}{kT}\right) \tag{2.2.48}$$

For the termolecular reaction, the system volume does not cancel and the corresponding equation is:

$$K_{eq} \equiv \frac{k_f}{k_r} = \frac{n_A n_B}{n_{AB}} = \frac{Q^A Q^B}{V Q^{AB}} \exp\left(-\frac{E_a}{kT}\right) \tag{2.2.49}$$

The partition function for each species can be written as the product of the separate translational, rotational, vibrational, and electronic partition functions:

$$Q = Q_{trans} Q_{rot} Q_{vib} Q_{el} \tag{2.2.50}$$

First, the translational partition function is:

$$Q_{trans} = V\left(2\pi mkT/h^2\right)^{3/2} \tag{2.2.51}$$

The rotational partition function is:

$$Q_{rot} = \frac{T}{\varepsilon' \Theta_{rot}} \tag{2.2.52}$$

where ε' is a symmetry factor equal to 2 for homonuclear molecules and 1 for heteronuclear molecules. The harmonic oscillator model leads to a vibrational partition function of:

$$Q_{vib} = 1/\left(1 - \exp\left(-\Theta_{vib}/T\right)\right) \tag{2.2.53}$$

Finally, the electronic partition function is summed over the j levels as:

$$Q_{el} = \sum_{i=0}^{j} g_i \exp\left(-\frac{E_{el}^i}{kT}\right) \tag{2.2.54}$$

where g_i are the degeneracies. Finally, it can be shown[2] that, for a bimolecular reverse reaction given the data for the forward reaction (a's and b's), the reverse reaction probability is:

$$P_{react} = \frac{\sigma_{react}}{\sigma_T} = \frac{a_f T^{b_f}}{(2/\varepsilon)\pi^{-1/2}\sigma_{ref}\left(T/T_{ref}\right)^{1-\omega}\left(2kT_{ref}/m_r\right)^{1/2}} \frac{Q^A Q^B}{Q^C Q^D} \tag{2.2.55}$$

Also, for the termolecular reverse reaction:

$$P_{react} = \frac{\sigma_{react}}{\sigma_T} = \frac{a_f T^{b_f}}{(2/\varepsilon)\pi^{-1/2}\sigma_{ref}\left(T/T_{ref}\right)^{1-\omega}\left(2kT_{ref}/m_r\right)^{1/2}} \frac{n_T V Q^{AB}}{Q^A Q^B} \tag{2.2.56}$$

For the case where the reverse reaction has finite activation energy, the probability is then:

$$P_{react} = \frac{\sigma_{react}}{\sigma_T} = \frac{a_f T^{b_f} \exp\left(-E_a/kT\right)}{(2/\varepsilon)\pi^{-1/2}\sigma_{ref}\left(T/T_{ref}\right)^{1-\omega}\left(2kT_{ref}/m_r\right)^{1/2}} \frac{Q^A Q^B}{Q^C Q^D} \frac{\Gamma\left(\bar{\zeta} + 5/2 - \omega\right)}{\Gamma\left(\bar{\zeta} + 5/2 - \omega, E_a/kT\right)} \tag{2.2.57}$$

2.2.4 Electric Field

Various researchers have modeled the electric field structure in a hypersonic shock layer in the past. The first such calculation was by Bird[26]. In his work, the electrons were moved through the computational grid with the ions that they were created with. No explicit electric field calculation was made, so the ions and electrons were not accelerated, and the simulation time step was that of the heavy particles. Later, Bird modified this method[27] to include a calculation of the ambipolar electric field using a form of the equation derived by Langmuir and Tonks[56]

$$E_{ambipolar} = -\frac{kT_e}{e}\frac{d\left[\ln\left(n_e\right)\right]}{dx} \tag{2.2.58}$$

In this equation, T_e and n_e are the average electron translational temperature and number density, macroscopic quantities derived from the DSMC solution. This equation can be derived from the macroscopic conservation of momentum for the electron species using the assumption of negligible inertial effects, negligible friction due to collisions, zero magnetic field and constant translational temperature. In his work, Bird calculated $E_{ambipolar}$ using the results from a previously converged calculation. He then re-converged the DSMC calculation, applying the prescribed acceleration to the charged particles at each time step from $E_{ambipolar}$. The field

$E_{ambipolar}$ was calculated from the re-converged DMSC solution, and the entire process repeated until there was no change in the resulting flow field parameters. The movement of the electrons was still tied to that of the ions in this method.

In the work by Gallis and Harvey[28], the electrons and ions were again moved together, and the electric field was calculated in a similar manner to equation (2.2.58). Here, however, the assumption of isothermal electrons was not made:

$$E_{ambipolar} = -\frac{kT_e}{e}\frac{d\left[\ln\left(p_e\right)\right]}{dx} \tag{2.2.59}$$

and the gradient of the electron pressure was instead used to calculate the ambipolar electric field. Gallis and Harvey used a simulation time step corresponding to the cell crossing time of the heavy particles, and accelerated the heavy particles according to the field $E_{ambipolar}$. They then computed the average ion velocity in a given cell, and adjusted the average electron velocity in the same cell to match. In this way, the electron energies were affected by the electric field in an average sense.

Carlson, Hassan and Taylor[25, 29] devised a method in which assumptions of zero net current and charge neutrality were used to calculate the electric field without the use of any macroscopic quantities. They wrote down Newton's law for a charged particle of species *s* moving under the influence of an electric field:

$$m_s\frac{d\vec{v}}{dt} = q_s\vec{E} \tag{2.2.60}$$

and thus the expressions for average electron and ion velocity by summing over individual particles:

$$\begin{aligned}\vec{v}_e &= \frac{\sum\vec{v}_{e,0}}{N_e} - \frac{e\overline{\vec{E}}\Delta t}{2m_e}\\ \vec{v}_i &= \frac{\sum\vec{v}_{i,0}}{N_i} + \frac{e\overline{\vec{E}}\Delta t}{2m_i}\end{aligned} \tag{2.2.61}$$

where $\overline{\vec{E}}$ is the average electric field over a simulation time step, N is the number of simulator particles, $\vec{v}_0$ is a velocity vector at the start of a simulation iteration, and the subscripts *e* and *i* refer to electron and ion species, respectively. By enforcing charge neutrality, $N_e = N_i$, they then solved for the ambipolar electric field required to make the average ion and electron velocities equal, while enforcing the assumption of zero net current:

$$\frac{e\overline{\vec{E}}\Delta t}{2} = \frac{\sum\vec{v}_{e,0} - \sum\vec{v}_{i,0}}{N_e\left(\sum\frac{1}{m_i} - \sum\frac{1}{m_e}\right)} \tag{2.2.62}$$

The electric field given above was used to accelerate the charged particles during the move portion of the DSMC algorithm. Additionally, a simple model of the particle acceleration in the plasma sheath at the vehicle surface was implemented. The electrons were reflected specularly from the vehicle surface to simulate their reflection in the strong negative potential gradient that would exist in the plasma sheath. An additional energy increment, $e\phi$, was added to the surface heat transfer measurement for each ion impacting the surface. The expected potential drop across the sheath, ϕ, was calculated from one-dimensional collisionless sheath theory.

Boyd[30] developed a model for the electric field of a weakly ionized plasma that is similar to the one originally proposed by Bird. The model was first implemented in a simulation of the plasma flow through an arcjet type thruster. Each electron is moved with the velocity of an ion throughout the domain, and the charged particles do not receive any velocity increment because of their response to an electric field. However, in this model, the average ion velocity of the cell in which the electron is located is used to move the electron particles, and it is not associated with a specific ion particle. This model maintains charge neutrality in an approximate sense, and results in lower computational overhead than the first model proposed by Bird.

In order to calculate the self-induced electric field without any assumption of charge neutrality, zero net current, or ambipolar diffusion, the electrostatic Poisson equation must be solved. This was carried out for very rarefied flows surrounding spacecraft in low Earth orbit by two groups of researchers[57, 58]. While interesting, the preliminary results presented by these researchers in the cited references are for flow fields of significantly different structure than the shock layers being considered in this work. Gallis *et al*.[59] presented preliminary results in which they solved the electrostatic Poisson equation in conjunction with the DSMC method for a hypersonic helium flow field. Unfortunately, the results presented in this work were sparse, and the physical processes associated with reacting air were not included in the analysis, and a systematic study of the effect of rigorously including the electric field in the computation on the flow field parameters was not presented.

Presently, a hybrid of Bird's original model and Boyd's model[30] was implemented. The electrons were kept separate but retained their own velocities as was done in Boyd's model; however, they are moved along with their associated ion as was done in Bird's model. By doing this, all particles are moved at the heavy particle time scale, but collisions occur at the electron time scale.

2.3 Recent Direct Simulation Monte Carlo Advances

Molecular-level chemistry models that predict equilibrium and non-equilibrium reaction rates using only kinetic theory and fundamental molecular properties (i.e., no macroscopic reaction-rate information) have recently been proposed[10, 11, 13, 14]. In addition, a new vibrational relaxation model has also been introduced that only relies on fundamental molecular properties and a single measure of vibrational collision number at a reference temperature[10]. Preliminary evaluations[14] indicate that the resultant reaction rates are in very good agreement with measured Arrhenius

rates for near-equilibrium conditions and with both measured rates and other theoretical models for far-from-equilibrium conditions.

2.3.1 Vibrational Relaxation

A new vibrational relaxation model has recently been introduced by Bird[10]. The data for the vibrational collision number, Z_{vib}, is generally presented as a function of temperature in a Millikan-White plot. A convenient way of using this information in a DSMC procedure is through an expression that employs the values of Z_{vib} at two temperatures. The temperatures may be set to the characteristic temperature of vibration, Θ_{vib}, and the characteristic temperature of dissociation, Θ_{diss}. Then, if the corresponding collision numbers are Z_c and Z_{diss}, the variation of the collision number with temperature T is given by:

$$Z_{vib} = Z_{diss}\left(\frac{\Theta_{diss}}{T}\right)^{\omega}\left[\frac{Z_c}{Z_{diss}}\left(\frac{\Theta_{vib}}{\Theta_{diss}}\right)^{\omega}\right]^{\left[\left(\frac{\Theta_{diss}}{T}\right)^{1/3}-1\right]\Big/\left[\left(\frac{\Theta_{diss}}{\Theta_{vib}}\right)^{1/3}-1\right]} \tag{2.3.1}$$

The problem with the Millikan-White data for most gases is that it leads to collision numbers less than unity at the dissociation temperature. This is physically impossible and the most effective way to deal with the problem is to set the collision number to unity at the dissociation temperature. Also, it is preferable to set the second temperature, T_{ref}, where the collision number is Z_{ref}. The collision number then becomes:

$$Z_{vib} = \left(\frac{\Theta_{diss}}{T}\right)^{\omega}\left[Z_{ref}\left(\frac{\Theta_{vib}}{T_{ref}}\right)^{\omega}\right]^{\left[\left(\frac{\Theta_{diss}}{T}\right)^{1/3}-1\right]\Big/\left[\left(\frac{\Theta_{diss}}{T_{ref}}\right)^{1/3}-1\right]} \tag{2.3.2}$$

For a procedure based on this equation, the required data for each vibrational mode is the vibrational collision number at the reference temperature. The one-third-power law is preserved, but there is a decrease in the rate at higher temperatures. This is essentially a more precise alternative to the "Park correction factor"[60] that is commonly employed in CFD.

Consider a collision in which the sum of the relative translational energy and the pre-collision vibrational energy of the molecule under consideration is E_{coll}. The "quantized collision temperature" is defined by:

$$\begin{aligned} T_{coll} &= \frac{i_{\max}\Theta_{vib}}{7/2-\omega} \\ i_{\max} &= Int\left[\frac{E_{coll}}{k\Theta_{vib}}\right] \end{aligned} \tag{2.3.3}$$

where the collision energy has been quantized through the truncation of i_{max} to an integer. The relevant parameters for the new vibrational model used are listed in Table A.3.

2.3.2 Chemical Reactions – The Quantum-Kinetic Chemistry Model

Bird has proposed[10, 11, 13] a set of molecular-level chemistry models based solely on fundamental properties of the two colliding particles: total collision energy, quantized vibrational levels, and molecular dissociation energies. These models link chemical-reaction cross-sections to the energy-exchange process and the probability of transition between vibrational energy states. The Larsen-Borgnakke[42] procedures and the principle of microscopic reversibility are then used to derive simple models for recombination reactions and for the reverse (exothermic) reactions. These models do not require any macroscopic data, and they balance the fluxes into and out of each state, thus satisfying microscopic reversibility. As mentioned earlier, preliminary evaluations[14] indicate that the resultant reaction rates are in very good agreement with measured Arrhenius rates for near-equilibrium conditions and with both measured rates and other theoretical models for far-from equilibrium conditions.

2.3.2.1 Dissociation Reactions

Bird suggests[10] that a complete and consistent description of vibrational energy exchange between colliding molecules must include dissociation. This concept is embodied in the energy-threshold model of Bird[2]. According to this model, during the energy-exchange process of a diatomic molecule, if the energy content of the vibrational mode exceeds the energy threshold of the dissociation or exchange reaction, the reaction $AB + T \rightarrow A + B + T$ occurs.

In his critique of Bird's model, Lord[61] pointed out that a "continuum" of states (i.e., an infinite number) exists above the dissociation limit. Therefore, Lord argues, if a dissociation reaction is energetically possible, it occurs. Thus, assuming a particular collision between two simulators, where at least one of them is a diatomic molecule, the serial application of the Larsen-Borgnakke energy exchange model would make the collision energy:

$$E_{coll} = E_{trans,pair} + E_{vib,mol} \tag{2.3.4}$$

available to the vibrational mode of the molecule in question. In this expression of collision energy, $E_{trans,pair}$ is the translational energy of the pair, and $E_{vib,mol}$ is the vibrational energy of the molecule considered for dissociation. Assuming a harmonic oscillator model, the maximum vibrational level that can be reached is that given in Equation (2.3.3), where the vibrational collision number has been defined as unity. If this level is higher than the dissociation level ($i_d = \Theta_d / \Theta_v$), or

$$i_{\max} > \frac{\Theta_{diss}}{\Theta_{vib}} \tag{2.3.5}$$

a dissociation occurs.

When the serial application of the quantum Larsen-Borgnakke model is considered, potential post-collision states i^* are chosen uniformly from the states equal to or below i_{max} and are selected through an acceptance-rejection routine[2] with probability

$$P_{vib}^{i^*} = \left(1 - \frac{i^* k\Theta_{vib}}{E_{coll}}\right)^{3/2-\omega} \tag{2.3.6}$$

where ω is the temperature exponent of the coefficient of viscosity. Then, the corresponding rate coefficient in an equilibrium VHS gas at temperature T is:

$$k_f^{diss}(T) = gR_{coll}^{AB,T}\Upsilon\left(i_{\max}\right)^{AB,T} \tag{2.3.7}$$

The degeneracy g of the reaction is included to cover the case of a polyatomic molecule in which the reaction can occur through more than one mode with the same characteristic vibrational temperature. The collision rate parameter $R_{coll}^{AB,T}$ is the collision rate for collisions between gas species AB and T divided by the number density product. It can be written for an equilibrium VHS gas as

$$R_{coll}^{AB,T} = \left(\frac{2\pi^{1/2}}{\varepsilon}\right)\left(r_{ref}^{AB} + r_{ref}^{T}\right)^2\left(\frac{T}{T_{ref}}\right)^{1-\omega^{AB,T}}\left(\frac{2kT_{ref}}{m_r^{AB,T}}\right)^{1/2} \tag{2.3.8}$$

where r_{ref} is the molecular radius at temperature T_{ref} and m_r is the reduced mass. For dissociations, it is necessary to add the symmetry factor ε that is 1 for homonuclear and 2 for heteronuclear molecules. The parameter $\Upsilon\left(i_{\max}\right)^{AB,T}$ is the fraction of collisions between AB and T that have sufficient energy to meet the condition of equation (2.3.5). With i as the pre-collision vibrational state of AB, the result for an equilibrium VHS gas is

$$\Upsilon\left(i_{\max}\right)^{AB,T} = \sum_{i=0}^{i_{\max}-1}\left\{Q\left[\left(5/2-\omega^{AB,T}\right), \frac{\left(i_{\max}-i\right)\Theta_{vib}^{AB}}{T}\right]\exp\left(-\frac{i\Theta_{vib}^{AB}}{T}\right)\right\} \Big/ z_{vib}(T)^{AB} \tag{2.3.9}$$

Here, $Q(a,x) = \Gamma(a,x)/\Gamma(a)$ is a form of the incomplete Gamma function and $z_v(T) = 1/\left[1-\exp\left(-\Theta_v/T\right)\right]$ is the vibrational partition function. As an example, the dissociation rate of molecular nitrogen is presented in Figure 2.3 for the Q-K model as compared to several rates from the literature, the first of which is the value used in the DSMC simulations using the TCE chemistry model.

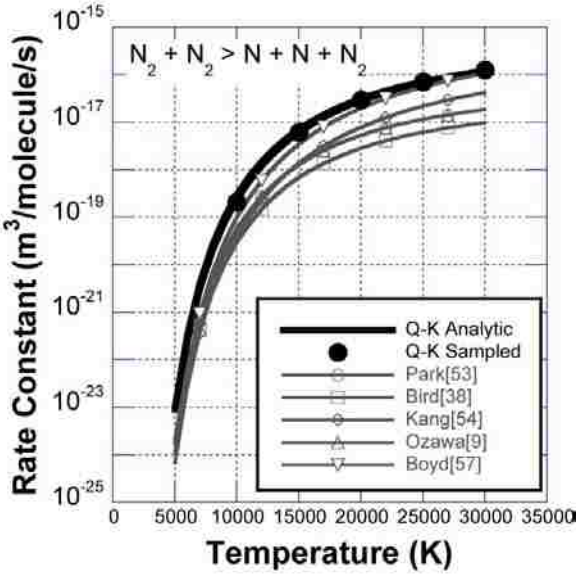

Figure 2.3: Comparison of Q-K dissociation rate of the reaction $N_2 + N_2 \rightarrow N + N + N_2$ with those from literature.

2.3.2.2 Recombination Reactions

The condition for recombination in a collision between species A and B is that another atom or molecule is within the "ternary collision volume" V_{coll}. The probability of recombination is therefore

$$P_{rec} = nV_{coll} \tag{2.3.10}$$

where n is the number density. The corresponding rate equation is

$$k_r(T) = R_{coll}^{A,B} nV_{coll} \tag{2.3.11}$$

The ratio $k_f(T)/k_r(T)$ from Equations (2.3.7) and (2.3.11) may be equated to the equilibrium constant from statistical mechanics in order to determine the ternary collision volume. It has been found that a volume in the form

$$V_{coll} = aT^b V_{ref} \tag{2.3.12}$$

allows nearly an exact fit of this ratio to the equilibrium constant. The coefficients used for these adjustments can be viewed in Table A.16. The reference volume V_{ref} is most conveniently set to the volume of the sphere with radius equal to the sum of the reference radii of the three particles.

The values of the constants a and b are determined in the context of the macroscopic temperature, but the evaluation of the ternary collision volume in the DSMC implementation is based on the quantities associated with the collision. The

"collision temperature" based on the relative translational energy in a collision with relative speed g is:

$$T_{coll} = \frac{m_r^{A,B} g^2}{2k\left(\frac{5}{2} - \omega^{A,B}\right)} \tag{2.3.13}$$

As an example, the cumulative recombination rate of two atomic nitrogen atoms is presented in Figure 2.4 as compared to values from the literature, the first of which is the rate computed by statistical mechanics from the dissociation of molecular nitrogen.

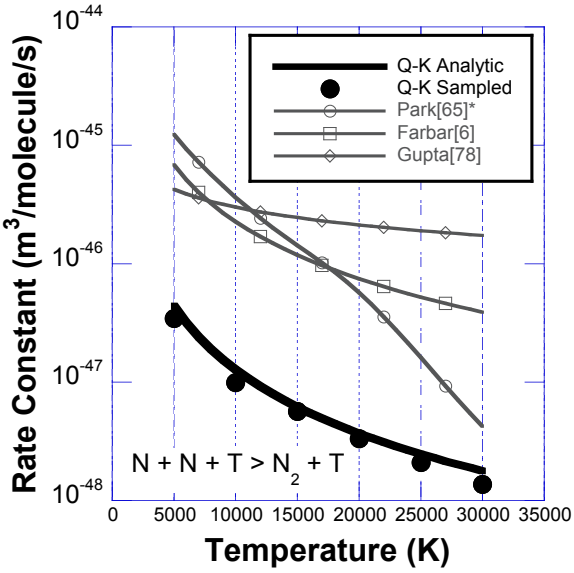

Figure 2.4: Comparison of Q-K recombination rate of atomic nitrogen with those from literature.

2.3.2.3 Exchange Reactions

Exchange reactions are binary reactions written as $A + B \leftrightarrow C + D$ in which A and C are the molecules that split, while B and D are the atoms. The phenomenological DSMC procedure for this reaction is analogous to that for the dissociation model. For both the forward and reverse reactions, the reaction probability is equal to that of Equation (2.3.6) with i^* set to the vibrational level corresponding to the activation energy of the reaction, i_a

$$i_a = Int\left[\frac{E_a}{k\Theta_{vib}}\right] \tag{2.3.14}$$

This is a relative probability that must be normalized through division by the sum of probabilities from the ground state to i_{max}, resulting in

$$P_{exch} = \frac{\left(1 - i_a k\Theta_{vib}/E_{coll}\right)^{3/2-\omega}}{\sum_{i=0}^{i_{\max}} \left(1 - ik\Theta_{vib}/E_{coll}\right)^{3/2-\omega}} \tag{2.3.15}$$

This is sufficient if the level i_a is much larger than unity, but some endothermic reactions and all exothermic reactions have either zero or small activation energies. The use of discrete levels then leads to unacceptably abrupt changes in the rate coefficients and it is impossible to obtain a near exact agreement between the ratio of forward to reverse rate coefficients and the equilibrium constant. The level i_a is the highest level with energy below the activation energy E_a and a smooth curve is obtained for the rate coefficients if the energy $i_a k\Theta_v$ in the numerator is replaced by E_a. The DSMC probability of an exchange reaction in a collision with $E_c > E_a$ is then

$$P_{exch} = \frac{\left(1 - E_a/E_{coll}\right)^{3/2-\omega}}{\sum_{i=0}^{i_{\max}} \left(1 - ik\Theta_{vib}/E_{coll}\right)^{3/2-\omega}} \tag{2.3.16}$$

An exact expression can be written down for the fraction of collisions that satisfy the condition of Equation (2.3.16) in an equilibrium VHS gas. With j as the pre-collision vibrational level, this is

$$\begin{aligned} \frac{dN}{N} = {} & \frac{1 - \exp\left(-\Theta_{vib}/T\right)}{\Gamma\left(5/2 - \omega\right)} \\ & \times \sum_{j=0}^{\infty} \exp\left(-\frac{j\Theta_{vib}}{T}\right) \int_{\left(E_a/k - j\Theta_{vib}\right)/T \text{ if } >0, \text{else } 0}^{\infty} \left[\frac{m_r g^2}{2kT}\left(1 - \frac{E_a}{\tfrac{1}{2} m_r g^2 + jk\Theta_{vib}}\right)\right]^{3/2-\omega} \\ & \times \left[\sum_{i=0}^{\left[\left(\frac{1}{2} m_r g^2 + jk\Theta_{vib}\right)/\left(k\Theta_{vib}\right)\right]} \left(1 - \frac{ik\Theta_{vib}}{\tfrac{1}{2} m_r g^2 + jk\Theta_{vib}}\right)^{3/2-\omega}\right]^{-1} \exp\left(-\frac{m_r g^2}{2kT}\right) d\left(-\frac{m_r g^2}{2kT}\right) \end{aligned} \tag{2.3.17}$$

and the corresponding rate coefficient is

$$k(T) = g R_{coll} \left(dN/N\right) \tag{2.3.18}$$

This is a complex expression not easily programmed, but it is possible to develop an alternative expression that is based on physical reasoning rather than formal kinetic theory. The selection of possible post-collision vibrational levels in Equation (2.3.6) is from an equilibrium distribution so that the rate coefficient is simply the product of the degeneracy g, the collision rate parameter, and the fraction of the vibrational level i_a in the Boltzmann distribution. The term $i_a k\Theta_v$ in the exponential is replaced by E_a in order to maintain consistency with Equation (2.3.16), and the normalizing factor is simply the vibrational partition function, thus

$$k_f(T) = g^A R_{coll}^{A,B} \exp\left(-\frac{E_a^{A,B}}{kT}\right) \Big/ z_{vib}(T)^A \tag{2.3.19}$$

and

$$k_r(T) = g^C R_{coll}^{C,D} \exp\left(-\frac{E_a^{C,D}}{kT}\right) \Big/ z_{vib}(T)^A \tag{2.3.20}$$

The default activation energy for the forward reaction is the heat of reaction and that for the reverse reaction is zero. The ratio of the forward to the reverse rate is compared with the equilibrium constant and the two are brought into the best possible agreement by the upward adjustment of either the forward or reverse activation energy. These adjustments are temperature dependent through a relation similar to that in Equation (2.3.12) for the ternary collision factor:

$$\begin{aligned} E_a &= a\left(\frac{T_{coll}}{T_{ref}}\right)^b \left|E_{exch}\right| \\ E_a &= E_a - E_{exch} \; if \; E_{exch} < 0 \end{aligned} \tag{2.3.21}$$

For the endothermic reaction, E_{exch} is the negative of the activation energy, which would then result in the second part of the equation adding the prescribed energy to the activation energy. For the exothermic reaction, E_{exch} is equal to the activation energy of the endothermic reaction, so the second part of the equation above does not come into effect. The coefficients used in these adjustments are presented in Table A.17. In addition to these phenomenological adjustments, there may be experimental or theoretical evidence for activation energies above the default values. Should a phenomenological adjustment fall short of the desired value, both the forward and reverse activation energies may be adjusted to keep the forward to reverse rate ratio in agreement with the equilibrium constant. As an example, the endothermic and exothermic reaction rates for the exchange reaction $N_2 + O \rightarrow NO + N$ are compared to rates from the literature in Figure 2.5 and Figure 2.6, respectively. The Q-K results presented in these figures are in good agreement with those presented from the literature.

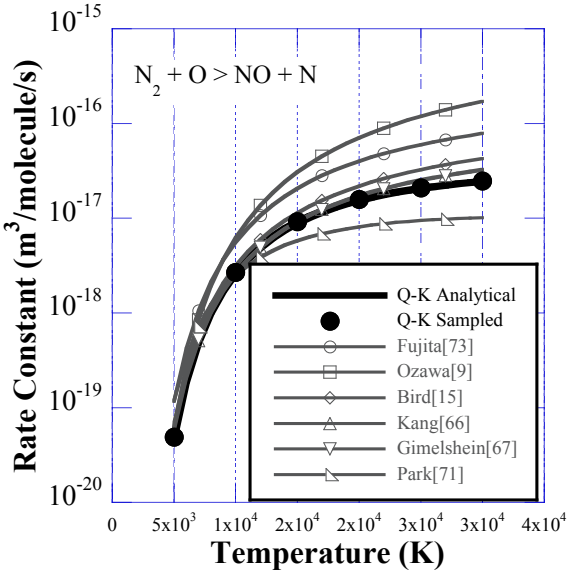

Figure 2.5: Comparison of Q-K exchange rate for the endothermic reaction $N_2 + O \rightarrow NO + N$ with those from literature.

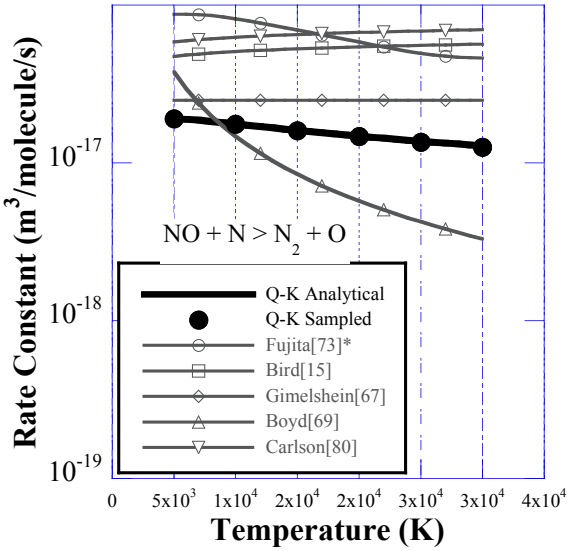

Figure 2.6: Comparison of Q-K exchange rate for the exothermic reaction $NO + N \rightarrow N_2 + O$ with those from literature.

Chapter 3: Extending the Quantum-Kinetic Chemistry Model

For missions where the shock-layer temperature reaches tens-of-thousands of degrees Kelvin, the importance of including electronic energy levels and ionization reactions becomes more pronounced. Although the treatment of electronic energy levels and ionization using the DSMC method is not a new development, most of these methods are based on measured, equilibrium rates, which are always questionable at high temperature, especially when applied to non-equilibrium problems.

In Chapter 2, the Quantum-Kinetic Chemistry Model of Bird was introduced. One of the attractive properties of this model is the fact that it does not rely on any macroscopic information, leveraging instead off of kinetic theory and physical data corresponding to the molecules undergoing each individual collision. The purpose of this chapter is to introduce new methods of treating electronic energy level transitions and chemical reactions involving charged species following the Q-K methodologies utilizing not only the vibrational energy levels, but also the electronic energy levels of the atoms and molecules.

3.1 Detailed Electronic Energy Level Model

To model the distribution of electronic energy in the DSMC technique, three procedures must be defined. First, when a particle is introduced into a simulation, it is necessary to obtain a new electronic energy from a given distribution through statistical sampling. A new electronic energy is also required when a particle changes its electronic energy after a collision with a surface. Under equilibrium conditions, the distribution has the well-known Boltzmann form. Second, it is necessary to statistically sample a new electronic energy following a collision, which involves electronic energy transfer. Third, a method to reproduce the electronic energy transition rate must be defined. Detailed examples of applying this model at hypersonic (re)entry conditions in air are presented subsequently in Section 4.3.

3.1.1 Equilibrium Sampling

Each electronic energy level j has a distinct energy, E_j, and degeneracy, g_j. The Boltzmann distribution for the electronic energy levels at a given temperature T gives the following result for the fraction of particles in level j:

$$f_{el}(j) = \frac{N_j}{N} = \frac{g_j \exp\left(-E_j/kT\right)}{\sum_{i=0}^{i_{\max}} g_i \exp\left(-E_i/kT\right)} \tag{3.1.1}$$

This distribution is used when either creating a new particle or after a surface collision in the DSMC simulation at a boundary specified at the temperature T. However, it is not possible to sample an electronic energy level j directly from the distribution. Therefore, an acceptance-rejection procedure is employed by selecting values for j from the following distribution:

$$f'_{el}(j) = \frac{g_j \exp\left(-E_j/kT\right)}{g_J \exp\left(-E_J/kT\right)} \tag{3.1.2}$$

where J is the value of j for which Equation (3.1.1) is a maximum. Unfortunately, since the degeneracy of each level is a variable specific to each species, there is no way to determine the maximum level a priori, so the maximum level must be searched for at each implementation or saved and recalled for a constant boundary temperature. The sampling of a new electronic energy level then proceeds as follows:

1. select at random an electronic energy level evenly distributed between 0 and J_{max} where J_{max} is the maximum possible energy level;
2. determine the value J for which Equation (3.1.1) is a maximum;
3. accept the value of j if $f_{el}'(j)$ > RAND, a random number;
4. if the value of j is not accepted, return to step 1.

3.1.2 Post-Collision Sampling

A phenomenological approach is usually adopted in the DSMC method when a collision occurs that involves energy transfer. The Larsen-Borgnakke method[42] samples a post-collision state from a combined distribution of the translational and electronic collision energies of the colliding particles. Based on the approach of Bergemann and Boyd[43] and Boyd[51], the Dirac delta function is employed to define the distribution of energies in Equation (3.1.1) in the following continuous form:

$$f_{el}\left(E_{el}, j\right) = \frac{g_j \exp\left(-E_j/kT\right)}{\sum_{i=0}^{i_{max}} g_i \exp\left(-E_i/kT\right)} \delta\left(\frac{E_{el}}{kT} - \frac{E_{el}^j}{kT}\right) \tag{3.1.3}$$

Consideration must now be given to the distribution of translational energy of the colliding particles. This distribution is naturally affected by the intermolecular model used since this determines the collision probability. For the present study, the variable hard sphere (VHS) collision model of Bird[41] is used. However, it is straightforward to develop the formulation for an alternative collision model such as the variable soft sphere of Koura[62]. For the VHS model, the distribution of the translational energies is:

$$f_{trans}\left(E_{trans}\right) = \frac{1}{\Gamma\left(5/2 - \omega\right)} \left(\frac{E_{trans}}{kT}\right)^{3/2-\omega} \exp\left(-\frac{E_{trans}}{kT}\right) \tag{3.1.4}$$

Using Equations (3.1.3) and (3.1.4), the combined distribution for sampling a post-collision electronic energy level j' from the total collision energy $E_{coll} = E_{trans}+E_{el} = E_{trans}'+E_{el}'$ is:

$$f\left(j';E_{coll}\right)=\frac{1}{\Gamma\left(\tfrac{5}{2}-\omega\right)}\frac{g_{j'}}{\sum_{i=0}^{i_{\max}} g_i \exp\left(-E_{el}^{i}/kT\right)}\left(\frac{E_{coll}-E_{el}^{j'}}{kT}\right)^{\tfrac{3}{2}-\omega}\exp\left(-\frac{E_{coll}}{kT}\right) \quad (3.1.5)$$

In applying the general Larsen-Borgnakke scheme, it is assumed that local thermodynamic equilibrium prevails. Therefore, the temperature T in Equation (3.1.5) is constant. Also, the total collision energy is constant, so it is only necessary to perform sampling of the post-collision state from the following distribution form:

$$g\left(j';E_{coll}\right)\propto g_{j'}\left(E_{coll}-E_{el}^{j'}\right)^{\tfrac{3}{2}-\omega} \quad (3.1.6)$$

Again, an acceptance-rejection procedure is used. The normalized distribution that is required is obtained by finding the value of j' for which Equation (3.1.6) is maximum, J', which is different for each value of E_{coll}. Therefore, the following distribution is obtained:

$$g'\left(j';E_{coll}\right)=\frac{g_{j'}\left(E_{coll}-E_{el}^{j'}\right)^{\tfrac{3}{2}-\omega}}{g_{J'}\left(E_{coll}-E_{el}^{J'}\right)^{\tfrac{3}{2}-\omega}} \quad (3.1.7)$$

The procedures are implemented as follows:

1. given a pair of particles with total collision energy E_{coll} which undergoes electronic energy exchange, determine J';

2. determine the maximum allowable electronic energy level obtainable from E_{coll}, J'';

3. take J^* to be the smaller of J' and J'';

4. as described in the previous section on equilibrium sampling, perform an acceptance-rejection procedure to sample j' from:

$$g'\left(j';E_{coll}\right)=\frac{g_{j'}\left(E_{coll}-E_{el}^{j'}\right)^{\tfrac{3}{2}-\omega}}{g_{J^*}\left(E_{coll}-E_{el}^{J^*}\right)^{\tfrac{3}{2}-\omega}} \quad (3.1.8)$$

3.1.3 Electronic Energy Level Transitions

A transition from electronic energy level i to level j for species A can be written in the form of a chemical reaction as $A^i + B \rightarrow A^j + B$. Following the Q-K model, the

simplest model is to assume that the transition occurs if the electronic energy level of A after a trial Larsen-Borgnakke redistribution of the collision energy, $E_{coll} = E_{trans}+E_{el}^{A}$, is $j^* = j$. Since the transition is treated as a chemical reaction, there are J_{max} transitions to consider where J_{max} is the maximum energy level energetically possible.

In the DSMC code, the process for determining if an energy level transition occurs, and if so, to which transition level, is as follows:

1. determine the value of J_{max} and compute the denominator of Equation (3.1.7);

2. perform acceptance-rejection according to Equation (3.1.7) until a test level is accepted.

This selection process is analogous to the selection process used in selecting a chemical reaction from a list of possible reactions.

3.2 Chemical Reactions Involving Charged Species

As outlined in Section 2.3.2, Bird[10, 11, 13], supported by Gallis[14], proposes a set of molecular-level chemistry models based solely on fundamental properties of the two colliding molecules: total collision energy, quantized vibrational energy levels, and molecular dissociation energies. These models link chemical cross-sections to the energy exchange process and the probability of transition between vibrational energy states. The Larsen-Borgnakke procedures and the principle of microscopic reversibility are then used to derive simple models. The models do not require any macroscopic data and they function by seeking to balance fluxes into and out of each state, thus satisfying microscopic reversibility. Since reactions involving only neutral species have been covered thus far, processes involving charged species are presented in the current section. Again, more detailed comparisons for these reactions pertaining to hypersonic (re)entry in are be presented in Sections 4.4 through 4.7.

3.2.1 Ionization Reactions

The procedure for ionization is analogous to that for dissociation. The difference is that ionization is linked to the electronic energy level instead of the vibrational energy level as with dissociation. For ionization, the collision energy is defined as $E_{coll}=E_{trans,pair}+E_{ele,particle}$ where the first term on the right is the relative translational energy of the colliding pair and the second term is the electronic energy of the particle being considered for ionization. If the collision energy is greater than the ionization energy of the particle, ionization occurs. The corresponding rate coefficient in an equilibrium VHS gas at temperature T is:

$$k_f^{ion}(T) = R_{coll}^{A,B}\Upsilon\left(J_{\max}\right)^{A,B} \tag{3.2.1}$$

where the collision rate parameter $R_{coll}^{A,B}$ is identical to that of Equation (2.3.8). The fraction of collisions between *A* and *B* that have sufficient energy to meet the requirement of ionization is then:

$$\Upsilon\left(J_{\max}\right)^{A,B} = \sum_{i=0}^{J_{\max}} Q\left(\tfrac{5}{2} - \omega^{A,B}, \frac{E_{ion} - E_{el}^{i,A}}{kT}\right) \frac{g_i^A \exp\left(-E_{el}^{i,A}/kT\right)}{z_{el}(T)^A} \tag{3.2.2}$$

where $z_{el}(T)^A$ is the electronic partition function for particle *A*.

3.2.2 Associative Ionization Reactions

The forward (endothermic) associative ionization reaction can be thought of occurring as $A + B \rightarrow AB^* \rightarrow AB^+ + e^-$ where AB^* is an intermediate, excited molecule that may lead to the ionized species AB^+ plus an electron. The first step is similar to the recombination procedure described in Ref. [10]. If the AB^* molecule is in the ground vibrational state after a trial Larsen-Borgnakke redistribution of the collision energy, the intermediate molecule is "formed." In the second step, the dissociation energy is first added to the original collision energy. The new collision energy is then distributed among the internal energy modes of the AB^* molecule and then this molecule is tested for ionization as described above. If the remaining collision energy after redistribution plus the electronic energy of the molecule is greater than the ionization energy of the molecule, the associative ionization reaction occurs. The corresponding rate coefficient can then be written as:

$$k_f^{AI} = R_{coll}^{A,B} \Upsilon_{f,AI}^{AB^*} \Big/ z_{vib}(T)^{AB^*} \tag{3.2.3}$$

where the collision rate parameter $R_{coll}^{A,B}$ is again identical to that of Equation (2.3.8). The vibrational partition function is included to account for the probability that the AB^* molecule will be in the ground state. The fraction of collisions with sufficient energy for the molecule AB^* to ionize are then calculated by summing over all possible initial internal energy states of atoms *A* and *B* (electronic energy states) and all possible vibrational, rotational, and electronic energy states of the intermediate AB^* molecule as follows:

$$\begin{aligned}\Upsilon_{f,AI}^{AB^*} = & \sum_{i_{el}^A=0}^{i_{el,\max}^A} \sum_{i_{el}^B=0}^{i_{el,\max}^B} \sum_{i_{vib}^{AB^*}=0}^{i_{vib,\max}^{AB^*}} \sum_{i_{rot}^{AB^*}=0}^{i_{rot,\max}^{AB^*}} \sum_{i_{el}^{AB^*}=0}^{i_{el,\max}^{AB^*}} f_{el}\left(i_{el}^A\right) f_{el}\left(i_{el}^B\right) \\ & \times P_{vib,trans}^{i_{vib}^{AB^*}}\left(E_{coll}^0\right) P_{rot,trans}^{i_{rot}^{AB^*}}\left(E_{coll}^1\right) P_{el,trans}^{i_{el}^{AB^*}}\left(E_{coll}^2\right) Q\left(\tfrac{5}{2} - \omega^{AB^*}, \frac{E_{ion} - E_{el}^{AB^*}}{kT}\right)\end{aligned} \tag{3.2.4}$$

The sums over the atomic electronic energy levels is over all possible levels. For the molecular internal energies, the maximum level is that which is the highest energetically possible. To start, an initial translational energy is assumed to be the average relative translational energy, or $(\tfrac{5}{2} - \omega)kT$. This is an approximation and

may result in a discrepancy between the above analytical expression and the actual sampled rate. It is possible to integrate over all possible relative translational energies, but it makes an already long calculation (summing over all possible internal states) much longer. As will be shown subsequently, this formulation results in an acceptable comparison with the sampled values in Section 4.4. The first two expressions after the summations are simply the probabilities of atoms A and B being in electronic levels $i_{ele}{}^{A}$ and $i_{ele}{}^{B}$, respectively. The next three terms are analogous to Equation (3.1.8) in that they are the probabilities of the respective internal mode of energy being at the specified quantum level at the specified collision energy. The collision energies are defined as:

$$\begin{aligned} E_{coll}^{0} &= \left(\tfrac{5}{2} - \omega\right) kT + E_{diss}^{AB^*} + E_{el}^{A} + E_{el}^{B} \\ E_{coll}^{1} &= E_{coll}^{0} - E_{vib}^{AB^*} \\ E_{coll}^{2} &= E_{coll}^{1} - E_{rot}^{AB^*} \end{aligned} \tag{3.2.5}$$

where each successive collision energy subtracts the previous internal energy mode. Then the last term, as in the dissociation and ionization rate equations, is the fraction of collisions for which the translational energy is greater than the difference between the ionization energy of AB^* and the electronic energy of AB^*.

The reverse (exothermic) associative ionization reaction is similar to the forward reaction. If the AB^* molecule is in the ground electronic state after a trial Larsen-Borgnakke redistribution of the collision energy, an intermediate molecule is "formed." In the second step, the ionization energy is first added to the original collision energy. The new collision energy is again distributed among the internal energy modes of the AB^* molecule, which is then tested for dissociation as described above. If the remaining collision energy after redistribution plus the vibrational energy of the molecule is greater than the dissociation energy of the molecule, the reverse associative ionization reaction occurs. The corresponding rate coefficient can then be written as:

$$k_r^{AI} = R_{coll}^{AB^+,e^-} \Upsilon_{r,AI}^{AB^*} \frac{g_0^{AB^*} \exp\left(-E_{el}^{0}/kT\right)}{\sum_{i=0}^{i_{\max}} g_i^{AB^*} \exp\left(-E_{el}^{i}/kT\right)} \tag{3.2.6}$$

where the collision rate parameter $R_{coll}^{A,B}$ is again identical to that of Equation (2.3.8). The last term is included to account for the probability that the AB^* molecule will be in the ground electronic state. The fraction of collisions with sufficient energy for the molecule AB^* to ionize are then calculated by summing over all possible initial internal energy states of AB^+ (the electron has none) and all possible vibrational, rotational, and electronic energy states of the intermediate AB^* molecule as follows:

$$\Upsilon^{AB^*}_{r,AI} = \sum_{i_{el}^{AB^+}=0}^{i_{el,\max}^{AB^+}} \sum_{i_{rot}^{AB^+}=0}^{i_{rot,\max}^{AB^+}} \sum_{i_{vib}^{AB^+}=0}^{i_{vib,\max}^{AB^+}} \sum_{i_{vib}^{AB^*}=0}^{i_{vib,\max}^{AB^*}} \sum_{i_{rot}^{AB^*}=0}^{i_{rot,\max}^{AB^*}} \sum_{i_{el}^{AB^*}=0}^{i_{el,\max}^{AB^*}} f_{el}\left(i_{el}^{AB^+}\right) f_{rot}\left(i_{rot}^{AB^+}\right) f_{vib}\left(i_{vib}^{AB^+}\right)$$
$$\times P_{vib,trans}^{i_{vib}^{AB^*}}\left(E_{coll}^0\right) P_{rot,trans}^{i_{rot}^{AB^*}}\left(E_{coll}^1\right) P_{el,trans}^{i_{el}^{AB^*}}\left(E_{coll}^2\right) Q\left(\tfrac{5}{2}-\omega^{AB^*}, \frac{E_{diss}-E_{vib}^{AB^*}}{kT}\right) \tag{3.2.7}$$

The sums over the internal energy levels of AB^+ are over all possible levels. For the internal energies of AB^*, the maximum level is that which is the highest energetically possible. In order to do this, an initial translational energy is again assumed to be the average relative translational energy, or $\left(\tfrac{5}{2}-\omega\right)kT$, along with the aforementioned cautions. The first three expressions after the summations are simply the probabilities of the AB^+ molecule being in the respective states. The next three terms are again analogous to Equation (3.1.8) in that they are the probabilities of the respective internal mode of energy being at the specified quantum level at the specified collision energy. The collision energies are defined as:

$$\begin{aligned} E_{coll}^0 &= \left(\tfrac{5}{2}-\omega\right)kT + E_{ion}^{AB^*} + E_{el}^{AB^*} + E_{rot}^{AB^*} + E_{vib}^{AB^*} \\ E_{coll}^1 &= E_{coll}^0 - E_{vib}^{AB^+} \\ E_{coll}^2 &= E_{coll}^1 - E_{rot}^{AB^+} \end{aligned} \tag{3.2.8}$$

where each successive collision energy subtracts the previous internal energy mode. Then the last term, as in the dissociation and ionization rate equations, is the fraction of collisions for which the translational energy is greater than the difference between the dissociation energy of AB^* and the vibrational energy of AB^*

3.2.3 Charge Exchange Reactions

The charge exchange reaction is analogous to the exchange reaction outlined in Section 2.3.2.3. The binary exchange reaction can be written as $A + B^+ \leftrightarrow A^+ + B$. This reaction takes place when the electronic energy level of the colliding neutral particle, *A*, after a trial Larsen-Borgnakke redistribution of the sum of the relative translational energy and electronic energy of the neutral particle is equal to the electronic energy level with energy just below the activation energy of the reaction. The probability of the reaction occurring is then:

$$P_{chex} = \frac{g_a\left(E_{coll}-E_{el}^a\right)^{\frac{3}{2}-\omega}}{\sum_{i=0}^{i_{\max}} g_i\left(E_{coll}-E_{el}^i\right)^{\frac{3}{2}-\omega}} \tag{3.2.9}$$

The corresponding rate equation for the forward reaction is then:

$$k_f^{chex}(T) = R_{coll}^{A,B^+} \frac{g_a \exp\left(-E_a^{A,B^+}/kT\right)}{\sum_{i=0}^{i_{\max}^A} g_i^A \exp\left(-E_{el}^{i,A}/kT\right)} \tag{3.2.10}$$

and for the reverse reaction is:

$$k_r^{chex}(T) = R_{coll}^{A^+,B} \frac{g_a \exp\left(-E_a^{A^+,B}/kT\right)}{\sum_{i=0}^{i_{\max}^B} g_i^B \exp\left(-E_{el}^{i,B}/kT\right)} \tag{3.2.11}$$

As with the exchange reactions in Section 2.3.2.3, the ratio of the forward and reverse reactions can be compared with the equilibrium constant and adjustments can be made to the phenomenological model to bring the model in closer agreement with statistical mechanics.

3.2.4 Other Exchange Reactions

In other exchange reactions involving charged species, the predominant mechanism is the breaking of a bond of one species (either neutral or charged) in order to exchange one atom to bond with the original atom, just as with an exchange reaction involving only neutral particles. Therefore, the logic for performing this reaction involving charged species is similar to that involving only neutral species.

3.3 Selecting a Reaction

Next, the Quantum-Kinetic chemistry model requires the selection of which reaction occurs. For many collision pairs, there may be more than one possible reaction. In the TCE chemistry model, the reaction probability is computed for each of the possible reactions and summed. This sum is then compared to a random number between zero and one. If the random number is less than the sum of the probabilities, a reaction is to take place. The selection of the reaction then proceeds by normalizing the reaction probabilities, and another random number is chosen to select which reaction is allowed. In the Q-K method, there is no clear analogy, and previous implementations have utilized a hierarchical approach where the reactions are considered by type first. For the neutral reactions, the dissociation reaction was always considered first and allowed to proceed even if an exchange reaction was a possibility. However, it was found that this approach tended to be biased in favor of dissociation reactions, especially at high temperatures where most of the collisions have larger relative translational energies and the vibrational level distribution is shifted to the higher levels. This method becomes even more undesirable when charged species reactions are included in the reaction set. Specifically, what happens when both dissociation and ionization reactions occur simultaneously? This event doesn't actually occur for the current reaction set under consideration (only electron impact ionization of atomic species is considered herein), but this is obviously an issue that needs to be resolved.

An alternate approach to the hierarchical method was therefore implemented. This approach is, like the TCE model, based on assigning reaction probabilities to all of the possible reactions, summing them, then comparing the sum to a random number. If the random number is less than the sum of the probabilities, then the probabilities are normalized and then another random number is generated to select the reaction. The reaction probabilities for exchange and charge exchange reactions have already been given in Equations (2.3.16) and (3.2.10), respectively. For the remaining reactions that occur when the collision energy is such that the reaction occurs (dissociation, ionization, and associative ionization), the probability is set equal to one if it is determined that the reaction is allowed to occur. These probabilities are then summed and compared to a random number between zero and one (obviously, if a dissociation, ionization or associative ionization reaction are possible, a reaction will occur). If a reaction is to occur, $P_{r,i}$ is defined as the reaction probability for the i^{th} reaction, and the cumulative distribution for all reactions up to and including the j^{th} reaction is:

$$\overline{P}_{r,i} = \frac{\sum_{n=1}^{j} P_{r,n}}{\sum_{n=1}^{NR} P_{r,n}} \tag{3.3.1}$$

where NR is the total number of reactions possible with the current reactants. A random number is then chosen to determine which reaction proceeds.

As shown subsequently in Chapter 4, this selection methodology allows the sampled reaction rate to accurately reproduce the analytical rates shown in this chapter. There is one item that requires mentioning at this point that the chemistry set utilized in this thesis does not include. That is the possibility of a dissociation and ionization reaction occurring for the same set of particles. For example, when molecular nitrogen collides with an electron, the molecule can either dissociate or ionize. Under the rules for these processes listed above, when the respective criterion is met for either reaction, the probability of that reaction occurring is unity. What happens when both have a probability of unity? Using the above reaction selection methodology, it is shown in Figure 3.1 that the sampled rates still accurately reproduce the analytical rates. This occurs because the energy required for dissociation is less than that for ionization, so will always occur more frequently as shown in the figure. The highest reaction rate physically possible would be equal to the collision rate of the particles. As the limit where all of the collisions have sufficient energy for both reactions is approached, a departure from the analytical rates occurs since both are equal, resulting in sampling rates one half the analytic rates.

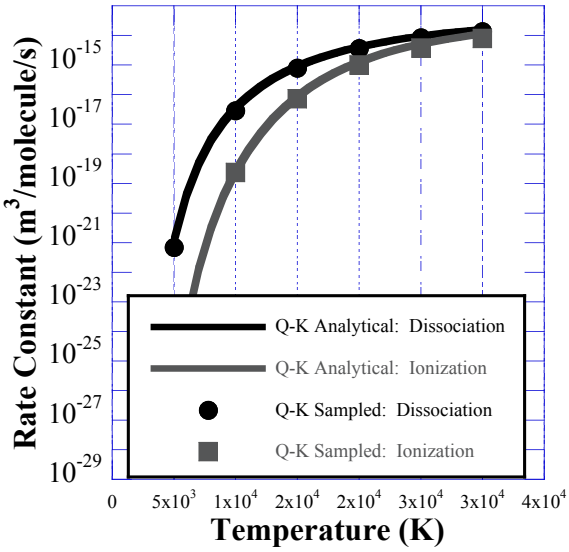

Figure 3.1: Sampled and analytic reaction rates when dissociation competes with ionization.

Chapter 4: Application of New Models to Upper-Atmosphere Hypersonic Flows

In this chapter, the new electronic energy level transition and chemistry models are validated by examining their ability to reproduce rates of chemical reactions in the literature[5-7, 9, 15, 29, 60, 63-78]. The DSMC models are applied in a two-dimensional code where the results are accumulated over all cells to approximate a zero-dimensional simulation. The test gas is comprised of eleven species: O, N, O_2, N_2, NO, O^+, N^+, O_2^+, N_2^+, NO+, and e^-. The simulations were run at various temperatures between 10,000 K and 60,000 K and at a continuum number density of 1.0e23 /m^3 in an adiabatic box 0.002 m on a side with 2 million particles. During the simulations, relaxation of the particles (including rotational, vibrational and electronic) was allowed to proceed as usual, but when a reaction was determined to take place, the number of reactions was advanced by one but the simulators were left unchanged, to maintain the thermodynamic energy balance with energy neither added nor removed from the gas.

4.1 Measurement of Reaction/Transition Rates

For a bi-molecular reaction $A + B \leftrightarrow C + D$, the forward reaction rate is calculated as:

$$k_f = \frac{dn_A / dt}{n_A n_B} \tag{4.1.1}$$

where the numerator is the change in number density of species A due to the reaction in the sampled time and the denominator is the product of the number densities of species A and B. The corresponding reverse reaction rate is:

$$k_r = \frac{dn_C / dt}{n_C n_D} \tag{4.1.2}$$

For a termolecular reaction $AB + T \leftrightarrow A + B + T$, the forward reaction rate is calculated as:

$$k_f = \frac{dn_{AB} / dt}{n_{AB} n_T} \tag{4.1.3}$$

as the bi-molecular reaction rate is, but the reverse reaction rate is now:

$$k_r = \frac{dn_A / dt}{2 n_A n_B n_T} \tag{4.1.4}$$

The capability of these techniques to reproduce measured equilibrium reaction rates will now be investigated. However, the uncertainty of the currently available measured rates for atmospheric hypersonic flows can be large. Most of the experimental data on which reaction rate sets are based were obtained for low temperatures (2,000 – 7,000 K). Even though uncertainty may be large, Park[60] suggests that the experimentally obtained reaction rates can be extrapolated up to 30,000 K.

The uncertainty of these measured rates is not always reported and in some cases is unknown. The problem becomes even more severe in the extrapolated portion of the temperature range ($T \geq$ 10,000 K). Park[60] reports that some rates measured for the same reaction differ by more than one order of magnitude, which will be apparent in the figures that follow. Since this work is focused on the extension of the Q-K model to electronic energy levels and reactions involving charged particles, only these transition and reaction rates will be discussed in this chapter. However, comparisons of the analytical Q-K rate expressions, the sampled Q-K rates, and rates found throughout the literature for every reaction included in this study are presented in Appendix C.

4.2 Definition of Translational, Rotational, Vibrational, and Overall Temperatures

There are various ways to define temperatures with regards to the DSMC methodology. In this work, we will refer to statistical mechanics for the definition of temperatures by defining the energy as:

$$\varepsilon = \tfrac{1}{2}\zeta RT \tag{4.2.1}$$

where ε is the specific energy of the quantity of interest, ζ is the number of degrees-of-freedom, R is the universal gas constant, and T is the temperature. By finding the energy, recognizing that $k = mR$, and rearranging Equation (4.2.1), one has the temperature of interest. For the translational temperature, we define ε_{trans} as:

$$\varepsilon_{trans} = \tfrac{1}{2}\overline{c'^2} \tag{4.2.2}$$

where $\overline{c'^2}$ is the average square of the thermal velocity defined as:

$$\overline{c'^2} = \overline{c^2} - 2\bar{\bar{c}}\bar{c}_0 + c_0^2 \tag{4.2.3}$$

where $\bar{\bar{c}}$ is the mean molecular velocity and $\bar{c}_0$ is the macroscopic stream or mean velocity. The translational temperature can then be defined as:

$$T_{trans} = \frac{2\varepsilon_{trans}}{3k} \tag{4.2.4}$$

since there are 3 translational degrees of freedom.

For the internal degrees of freedom of a specific species n, we define the average internal energy of a single particle as:

$$\overline{E_{\text{int}}^{n}} = m_n \varepsilon_{\text{int}}^{n} \tag{4.2.5}$$

and the temperature is then:

$$T_{\text{int}}^{n} = \frac{2\overline{E_{\text{int}}^{n}}}{k\zeta_{\text{int}}^{n}} \tag{4.2.6}$$

For the overall internal temperature averaged over all of the N species, we then define:

$$T_{\text{int}} = \frac{\sum_{n=1}^{N} \zeta_{\text{int}}^{n} T_{\text{int}}^{n}}{\sum_{n=1}^{N} \zeta_{\text{int}}^{n}} \tag{4.2.7}$$

For rotational energy, the average energy of each species is found by summing the rotational energies of the particles in the computational cell and dividing by the number of particles. For the rotational degrees of freedom, it is assumed that the mode is fully excited and is set to 2 for diatomic molecules.

For vibrational energy, the average energy of each species is again found by summing the vibrational energies of the particles and dividing by the number of particles. To then find the number of vibrational degrees of freedom for the species, using the definition of the average vibrational energy level $\overline{i_n} = \overline{E_{vib}^{n}} \big/ k\Theta_{vib}$ and some manipulation, one gets:

$$\zeta_{vib}^{n} = 2\overline{i_n} \ln\left(1 + 1/\overline{i_n}\right) \tag{4.2.8}$$

The electronic temperature is treated in a similar manner, but some modifications must be made to account for the discretized spacing of the electronic energy levels. To begin, the species electronic temperature is defined as:

$$T_{ele}^{n} = \frac{E_{ele}^{1,n} - E_{ele}^{0,n}}{k \ln\left(\dfrac{n_0^n g_1^n}{n_1^n g_0^n}\right)} \tag{4.2.9}$$

where the 0 and 1 denote the ground and first excited electronic energy levels, g is the degeneracy of the level, and n can be taken as the number density or total number of samples (result is the same since the ratio is being taken). This definition comes directly from the ratio of the Boltzmann distribution of the ground and first excited

electronic energy levels. Then, the effective number of degrees of freedom is defined as:

$$\zeta_{ele}^{n} = \frac{2\overline{E_{ele}^{n}}}{kT_{ele}^{n}} \tag{4.2.10}$$

as we have defined the effective degrees of freedom of the other internal modes.

4.3 Electronic Energy Level Transitions and Comparison to Equilibrium

The following section applies the methodologies developed in Section 3.1 to the aforementioned equilibrium heat bath. There are excitation and quenching processes between each of the atomic/molecular energy levels, resulting in a large number of rates being required for previous electronic energy level transition models, both for CFD and DSMC. The new Q-K based transition model negates the necessity for each of these transition rates (most of which use approximate analytic formulas). In the following sub-sections, only a portion of the transitions presented in Appendix C are discussed for exemplary purposes only.

4.3.1 Electron-Impact Excitation

The process of electron-impact excitation is significant for both atoms and molecules in hypersonic shock-layer applications. To begin, the electron-impact transitions of atomic nitrogen are examined. The sampled transition rates are compared to values reported by Tayal[79], Park[60], and Frost[80]. The transitions from the first to the fifth level and from the second to the fifth level are presented in Figure 4.1 and Figure 4.2, respectively. It is important to note that the 1-5 transition is considered a "forbidden" transition, while the 2-5 transition is an "allowed" transition. Even so, the phenomenological Q-K model compares very well to the reported rates from the literature.

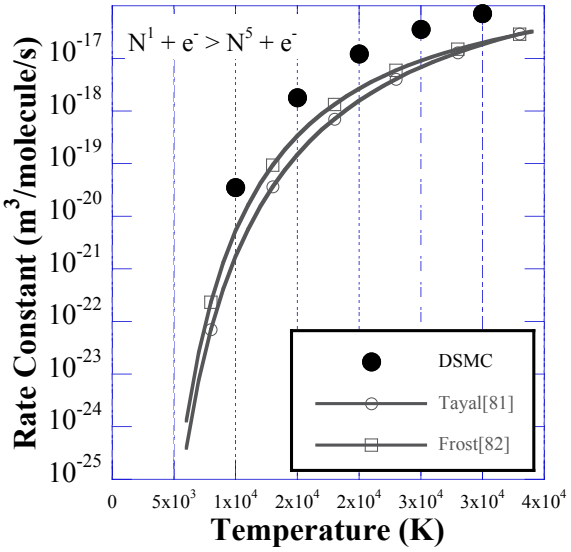

Figure 4.1: Comparison of sampled and reported electronic energy level transition rates from the first to fifth energy levels of atomic nitrogen.

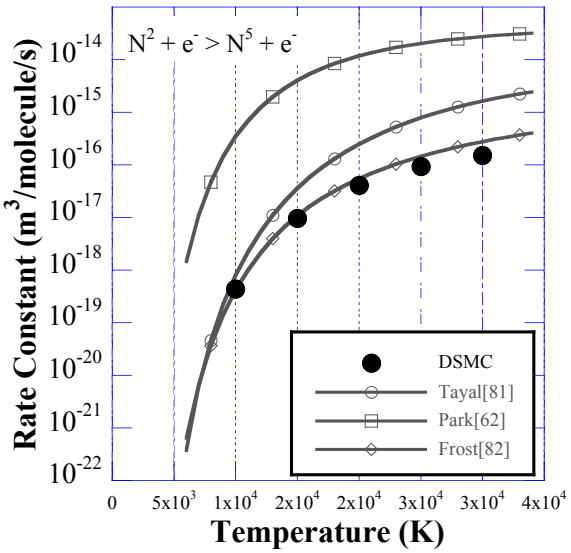

Figure 4.2: Comparison of sampled and reported electronic energy level transition rates from the second to the fifth energy levels of atomic nitrogen.

For the electron-impact transitions of atomic oxygen, the sampled transition rates are compared to values reported by Zatsarinny[81], Park[60], and Bhatia[82]. Once again, even though one transition is allowed (level 1-5, Figure 4.3) and one is forbidden (level 2-5, Figure 4.4), the comparisons are quite favorable.

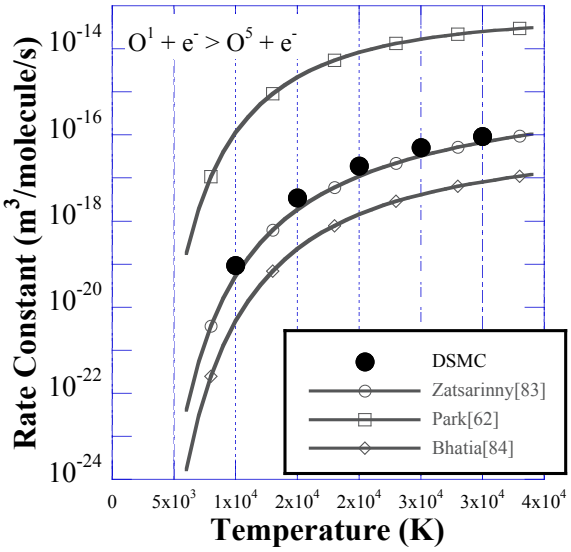

Figure 4.3: Comparison of sampled and reported electronic energy level transition rates from the first to fifth energy levels of atomic oxygen.

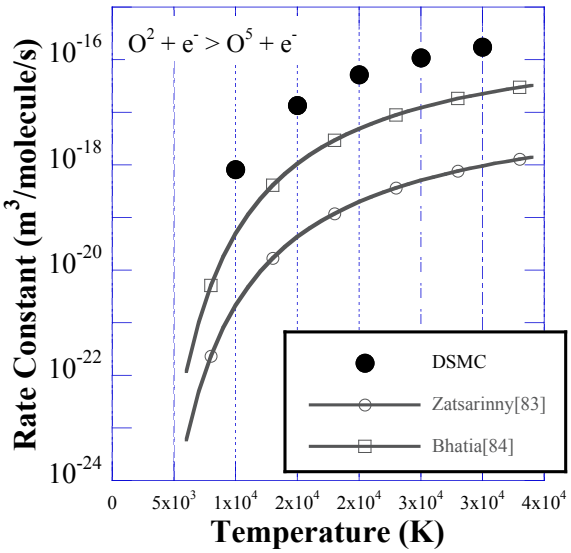

Figure 4.4: Comparison of sampled and reported electronic energy level transition rates from the second to the fifth energy levels of atomic oxygen.

The electron-impact transition rates of the molecular species are compared to rates presented by Cherni[83], Telulet[84], and Gorelov[85]. Example transition rates for molecular nitrogen, nitric oxide, and the molecular nitrogen ion are shown in Figure 4.5, Figure 4.6, and Figure 4.7, respectively. Again, good agreement is shown between the sampled rates and the reported rates.

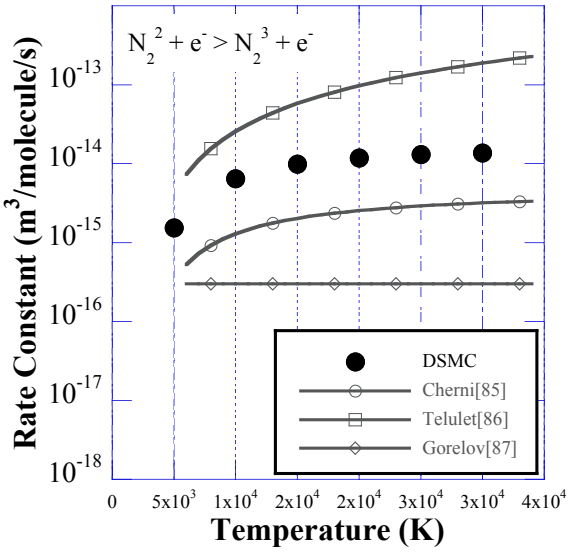

Figure 4.5: Comparison of sampled and reported electronic energy level transition rates from the second to the third energy levels of molecular nitrogen.

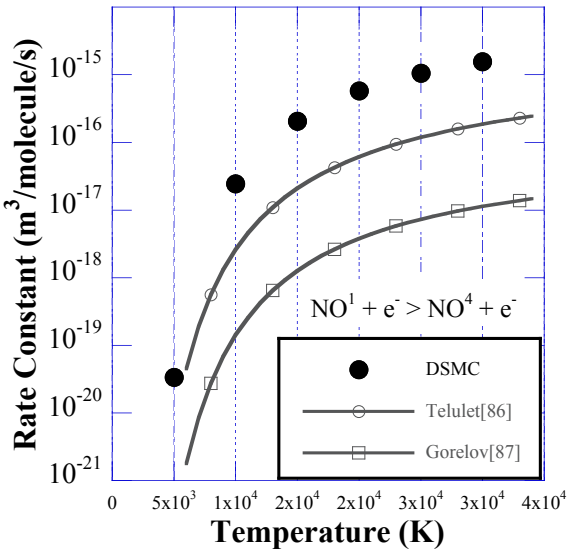

Figure 4.6: Comparison of sampled and reported electronic energy level transition rates from the first to the fourth energy levels of nitric oxide.

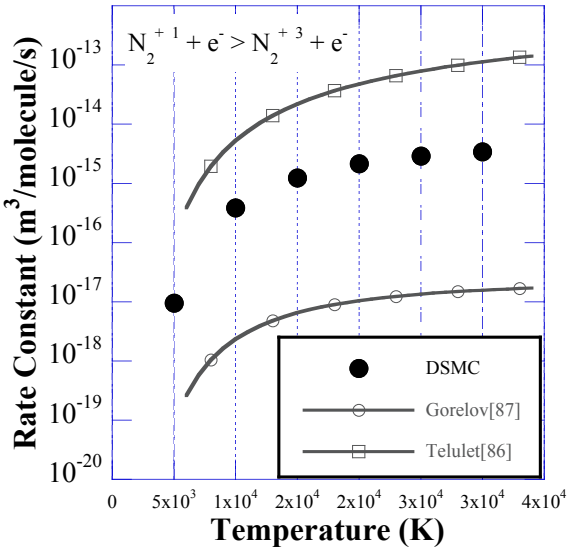

Figure 4.7: Comparison of sampled and reported electronic energy level transition rates from the first to the third energy levels of the molecular nitrogen ion.

4.3.2 Heavy Particle Impact Excitation

Transitions due to heavy particle collisions are similar to electron-impact transitions, but they are significantly less important for most applications, as discussed by Johnston[86], where he shows that the process is negligible for atomic and molecular species in lunar-return shock layers. The comparisons shown in this section are, for the most part, as favorable as those in the previous section for electron-impact transition rates. Comparisons are made with values reported in References [85, 87-93]. For example, the transitions of the molecular nitrogen ion when colliding with molecular nitrogen, as shown in Figure 4.8, is generally within an order of magnitude of the reported values (note the 3-4 order of magnitude in the spread of data for the level 1-2 transition). There is also good agreement for collisions of molecular nitrogen and nitric oxide for most transitions, as exemplified in Figure 4.9 and Figure 4.10, respectively.

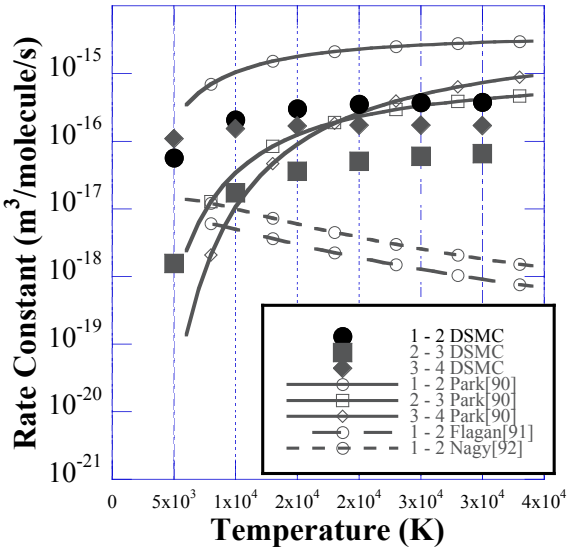

Figure 4.8: Comparison of sampled and reported electronic energy level transition rates for the molecular nitrogen ion when colliding with molecular nitrogen.

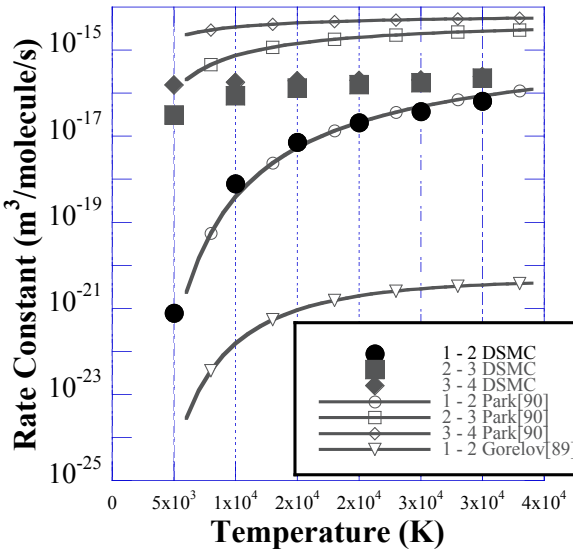

Figure 4.9: Comparison of sampled and reported electronic energy level transition rates for molecular nitrogen when colliding with atomic nitrogen.

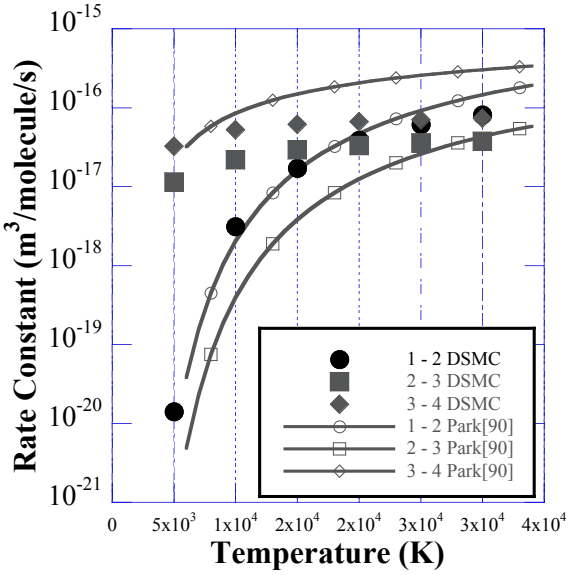

Figure 4.10: Comparison of sampled and reported electronic energy level transition rates for nitric oxide when colliding with molecular nitrogen.

However, there seem to be certain combinations of heavy-impact partners where the current phenomenological model can't accurately reproduce the measured/calculated transition rates. These combinations generally include transitions where the collision partner is molecular nitrogen, as shown in Figure 4.11, and the transition is from the lower levels (i.e., 1-2 or even some times 2-3).

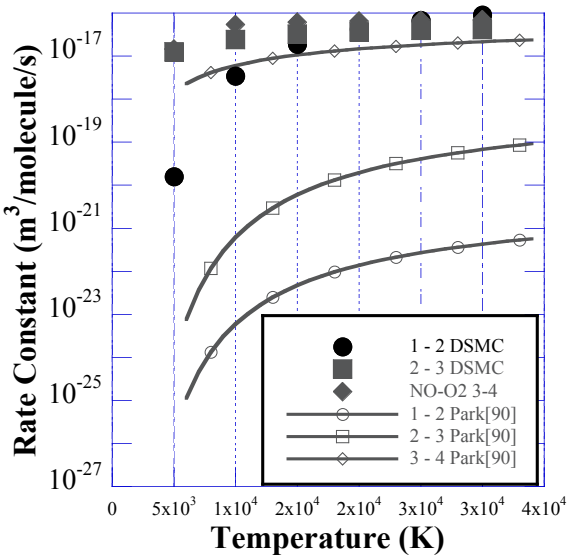

Figure 4.11: Comparison of sampled and reported electronic energy level transition rates for the nitric oxide when colliding with molecular nitrogen.

The current model also appears to have some difficulty in reproducing electronic energy level transitions in collisions of molecular oxygen, as shown in Figure 4.12.

However, even though these comparisons have been less than ideal, they are not completely unreliable considering the four to five order of magnitude spread in the rates previously reported from the literature.

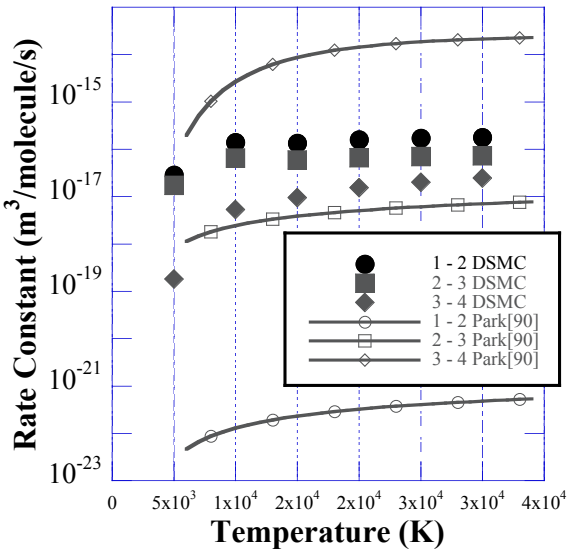

Figure 4.12: Comparison of sampled and reported electronic energy level transition rates for molecular oxygen when colliding with atomic oxygen.

4.3.3 Equilibrium conditions

In order for the electronic energy level procedures to be acceptable, they need to reproduce equilibrium conditions after the simulation has been allowed to run for a sufficient amount of time to ensure that detailed balance has been enforced. The first requirement is for the sampled translational and electronic temperatures to remain very near the input equilibrium temperature. The sampled translational, electron, and electronic temperatures for all of the species are presented in Table B.1 at 10,000, 20,000, and 30,000 K. All of the temperatures depart from the set equilibrium value by less than 0.5%.

The resultant population distribution for the first seven energy levels of all atomic and molecular species (where applicable) for a range of temperatures is compared to the Boltzmann distribution in Table B.2 through Table B.31. Again, the simulation represents the equilibrium state very well, with sampled departures from the Boltzmann distribution less than 1% for most levels where the number fraction in the state is above 1.0×10^{-3}. The larger departure from the equilibrium distribution is expected for levels with a very small population due to statistical noise.

4.4 Associative Ionization Reactions

Because of their low threshold energies, associative ionization reactions play an important role in determining the level of ionization and structure of the flow field at hypersonic reentry conditions. There exists very little experimental or computational data in the literature regarding the associative ionization reactions in air. The associative ionization reaction $N + O \leftrightarrow NO^+ + e^-$ has the lowest energy threshold, however the associative ionization reactions of $N + N \leftrightarrow N_2^+ + e^-$ and $O + O \leftrightarrow O_2^+ + e^-$ are also very important mechanisms in the current application. The sampled DSMC reaction rates of endothermic and exothermic reactions of the $N + O$ reaction are compared to measured rates from the literature in Figure 4.13 and Figure 4.14, respectively.

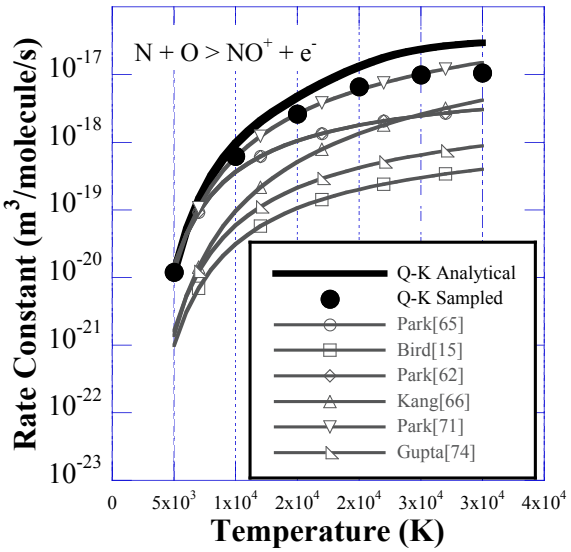

Figure 4.13: Endothermic associative reaction rates for $N + O \rightarrow NO^+ + e^-$ compared to rates from the literature.

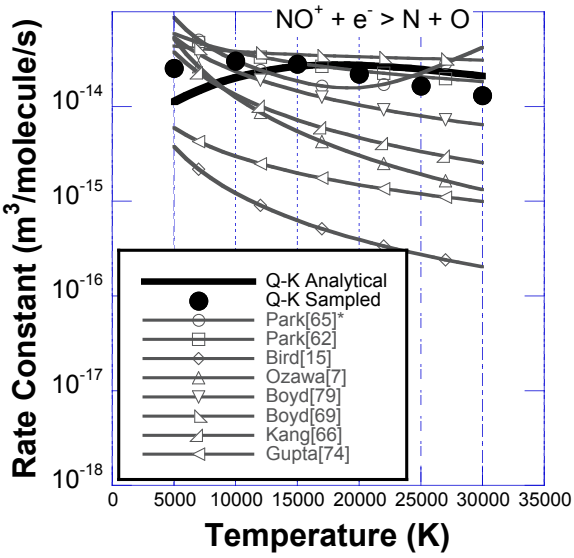

Figure 4.14: Exothermic associative reaction rates for $NO^+ + e^- \rightarrow N + O$ compared to rates from the literature.

In these figures, the black lines are the analytical solutions from Equations (3.2.3) and (3.2.6), the black symbols are the sampled rates from the DSMC code, and the first of the values from literature is the curve used by LAURA. As discussed earlier, there is a wide spread in the reaction rates reported in the literature. Given the assumed measurement uncertainty, the Q-K reaction rates are in good agreement with the rates from the literature.

4.5 Ionization Reactions

Another important reaction mechanism for ionized, hypersonic reentry problems is the ionization of an atom or molecule by direct impact. There is very limited data in the literature for heavy particle impact ionization and these reactions are not generally included in reentry computations, so they will not be discussed in this work. There is, however, an appreciable amount of data related to electron impact ionization reactions, especially for atomic species. The electron impact ionization reactions generally considered in reentry computations are those for atomic nitrogen and oxygen. Reaction rate curves for the electron impact ionization reaction for atomic oxygen are presented in Figure 4.15.

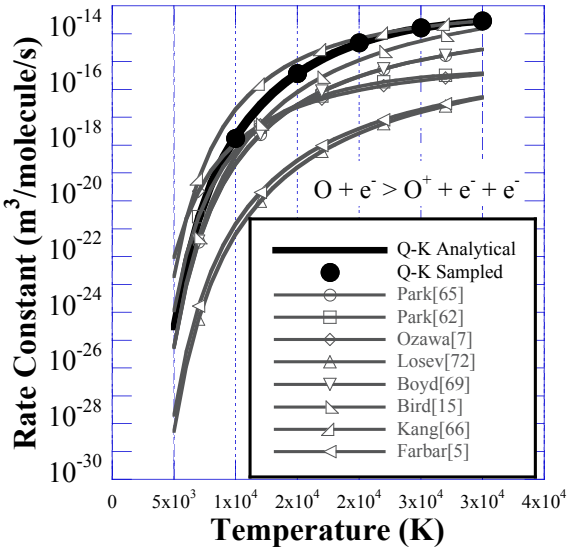

Figure 4.15: Endothermic ionization reaction rates for $O + e^- \rightarrow O^+ + e^- + e^-$ compared to rates from the literature.

4.6 Charge Exchange Reactions

In charge exchange reactions, a singly charged ion (such as N^+ or O^+) collides with a neutral atom or molecule and captures one of its electrons, thereby becoming a neutral atom. Only a small amount of energy is transferred to the electron donor, so the newly created neutral particle retains most of the original energy of the ion. These can therefore be an important mechanism for the creation of high-energy neutral particles. The measured reaction rates from the endothermic and exothermic charge exchange reactions corresponding to $N_2 + N^+ \rightarrow N_2^+ + N$ are shown in Figure 4.16 and Figure 4.17, respectively, compared to the values from the literature as shown.

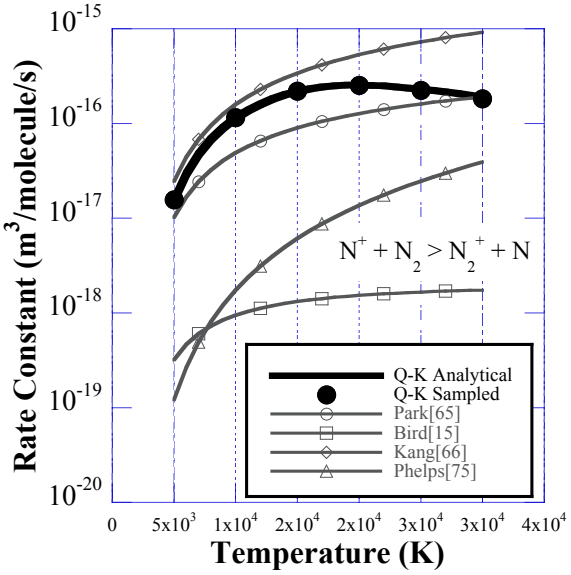

Figure 4.16: Endothermic charge exchange reaction rates for $N^+ + N_2 \rightarrow N_2^+ + N$ compared to rates from the literature.

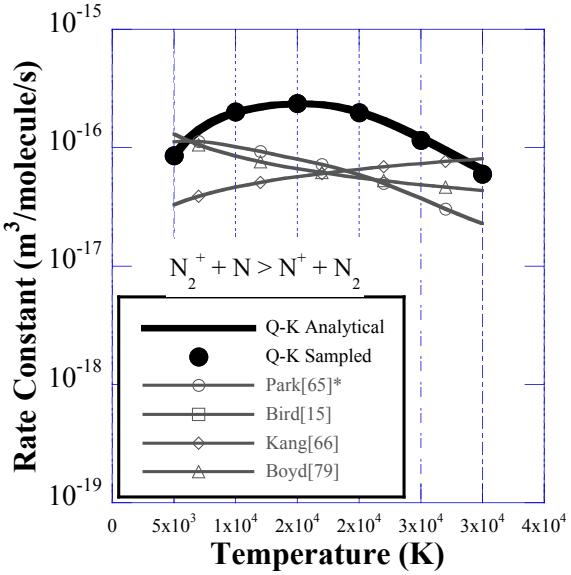

Figure 4.17: Exothermic charge exchange reaction rates for $N_2^+ + N \rightarrow N^+ + N_2$ compared to rates from the literature.

4.7 Exchange Reactions Involving Charged Species

The remainder of relevant chemical reactions involves various exchange reactions involving charged species. As an example, the endothermic and exothermic reaction rates for the reaction $NO^+ + N \leftrightarrow N_2^+ + O$ are shown in Figure 4.18 and Figure 4.19, respectively, compared to values from the literature as shown.

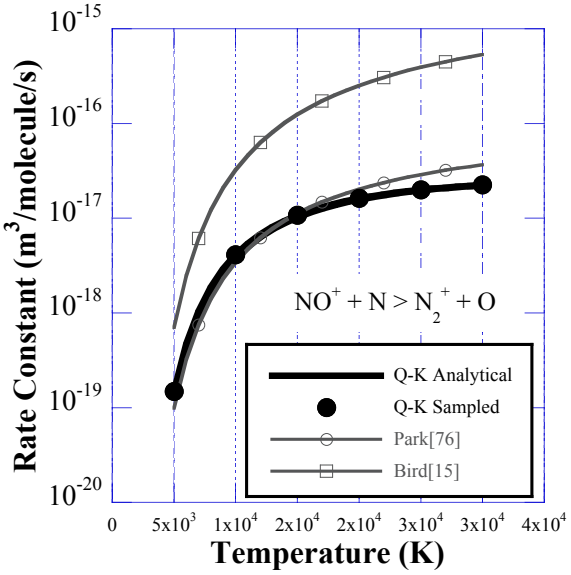

Figure 4.18: Endothermic reaction rate for the exchange reaction involving charged species $NO^+ + N \leftrightarrow N_2^+ + O$ with comparisons to rates from the literature.

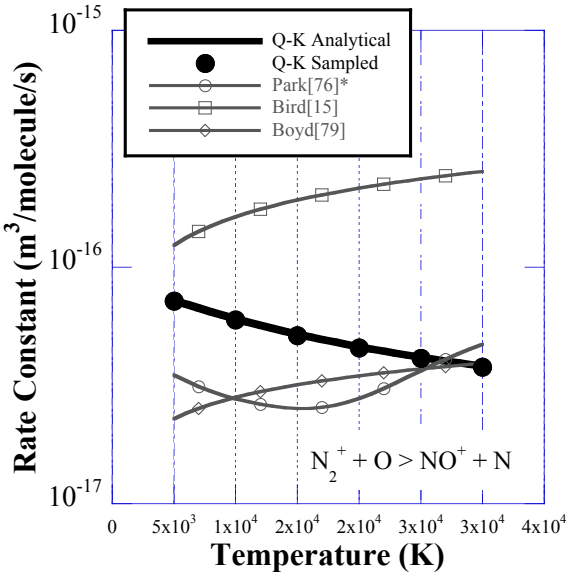

Figure 4.19: Exothermic reaction rate for the exchange reaction involving charged species $N_2^+ + O \leftrightarrow NO^+ + N$ with comparisons to rates from the literature.

Chapter 5: Modeling of the FIRE II Reentry Flow with Ionization and Electronic Energy Levels with DSMC

In this chapter, the newly developed DSMC models presented in previous chapters are exercised on a demanding near-continuum reenty flow field with ionization. These results are compared with results from traditional DSMC models, a solution of the FIRE II flow field obtained using current best practices in computational fluid dynamics (CFD), and values inferred from flight. Both flow field and surface parameters are examined. To this end, three DSMC cases are summarized in Table 5.1.

Table 5.1: List of DSMC FIRE II cases.

Case	Electronic Energy Model	Chemistry Model
Case 1	None	TCE
Case 2	Present	TCE
Case 3	Present	Q-K

5.1 The Project FIRE Flight Experiment

The Project FIRE (Flight Investigation Reentry Environment) was an Apollo-era flight experiment to measure the radiative and convective heating on spacecraft material during atmospheric reentry at lunar return speeds (11.35 km/s)[21]. Project FIRE consisted of two sub-orbital flight experiments launched April 14, 1964 and May 22, 1965 from Cape Kennedy, Florida. For the current study, computations are performed for the reentry conditions of the second flight at 1634 seconds, which corresponds to an altitude of 76.42 km, and conditions for the simulation are provided in Table 5.2. The geometry and dimensions of the second vehicle in the experimental series, FIRE II, are presented in Figure 5.1. The forebody of the FIRE II reentry vehicle consisted of three phenolic-asbestos heat shields sandwiched between beryllium calorimeters. The first two heat shield and calorimeter packages were designed to be ejected after the onset of melting, yielding heating data free of the effects of ablation and three separate data gathering periods. Calorimeter plugs and radiometers were located at various positions on the heat shields. The flight condition examined in this study occurred during the first data collection period.

Table 5.2: Free stream and surface parameters for FIRE II entry condition.

Time (s)	Altitude (km)	ρ_∞ (kg/m^3)	n_∞ (m^{-3})	V_∞ (m/s)	T_∞ (K)	Kn_D	T_{wall} (K)	X_{N2}	X_{O2}
1634	76.42	3.72E-05	7.73e20	11360	195	2.59E-03	615	0.76	0.24

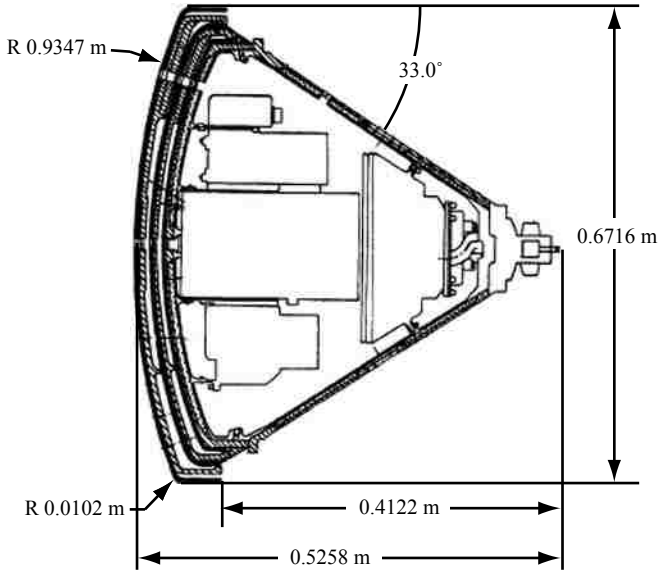

Figure 5.1: Schematic of FIRE II test vehicle.

5.2 Details of the Continuum Flow Model and Non-Equilibrium Radiation Model

Two different numerical approaches are applied: a CFD solution of the Navier-Stokes equations using the Langley Aerothermodynamic Upwind Relaxation Algorithm code and particle-based DSMC computations using the DAC code, which is the focus of this study. All computations presented herein were steady state and axisymmetric with the x-direction along the axis. In each case, an 11-species, 21-reaction, thermochemical non-equilibrium approach is adopted. The surface catalytic boundary condition used in the CFD solution was "fully-catalytic," which means that all atomic species recombine to their molecular counterpart (i.e., $N + N \rightarrow N_2$) and also charged heavy species recombine with electrons to form their charge neutral counterpart (i.e., $N^+ + e^- \rightarrow N$).

The Langley Aerothermodynamic Upwind Relaxation Algorithm (LAURA) is a high fidelity, structured grid computer code, specialized for hypersonic re-entry physics, utilizing state-of-the-art algorithms for computational fluid dynamic simulations[94, 95]. Key elements of LAURA include Roe's averaging[96] and Yee's Symmetric Total Variation Diminishing (STVD)[97] formulation of second-order, inviscid flux. Yee's STVD formulation has been found to be exceptionally robust and Courant number independent using first point-implicit and then line-implicit relaxation for hypersonic flow simulations.

A two-temperature thermochemical non-equilibrium model[95] is applied. The chemical reaction rates are compiled from previous studies (listed as the references for the first reaction rate parameters for each reaction in Table A.14). The thermophysical properties are taken from the work of Mcbride *et al*.[98] and Gupta *et*

al.[76]. Multicomponent diffusion is approximated using Sutton and Gnoffo's[99] approximate-corrected approach.

The shock-layer radiation is modeled with the HARA (High-temperature Aerothermodynamic RAdiation) code. The details of this code for treating air species are presented by Johnson *et al*.[19, 20]. Briefly, it is based on a set of atomic levels and lines obtained from the National Institute of Standards and Technology (NIST) online database[100] and the Opacity Project[101], as well as atomic bound-free cross sections from the TOPbase[102]. The negative nitrogen and oxygen ions are treated using cross sections suggested by Soon and Kunc[103] and Chauveau *et al*.[104], respectively. The molecular band systems are treated using a smeared-rotational band (SRB) model[105], which was shown by Johnston *et al*.[19] to be sufficient for treating VUV absorbing and optically-thin emitting band systems in air. The molecular data for modeling these band systems are obtained from Laux[106], except for the VUV N_2 systems, which are obtained from various other sources[107-109]. The non-Boltzmann modeling of the atomic and molecular electronic states is based on a set of electron-impact excitation rates compiled from the literature and presented in detail by Johnston *et al*.[20]. Following the work of Park[110], the quasi-steady state assumption is made when solving the Master Equation. The tangent-slab approximation is applied to calculate radiative flux and the divergence of the radiative flux.

5.3 DSMC Simulation Parameters

In this section, the parameters used in the simulation of the FIRE II flight experiment are discussed.

5.3.1 Collision Modeling

The baseline collision model implemented in DAC, for both neutral and charged species interactions, is that originally published by Bird[41], in which all particle interactions are treated using the VHS collision model. The reference diameters of the heavy ions O_2^+, N_2^+, O^+, N^+, and NO^+ are set equal to the diameters of their associated neutral particles, and the reference diameter of the electrons is set to 1e-10 m. This value of the electron reference diameter is much larger than the classical value of 6e-15 m, and is used to produce electron collision cross sections of the required magnitude within the mathematical framework of the VHS collision model. A complete list of the VHS reference diameters for all species and the parameters T_{ref} and ω is given in Table A.1. As shown previously, the present choice of electron reference diameter does not introduce significant error in the DSMC results.

5.3.2 Internal Energy Modeling

For the current thesis, the rotational collision number is set to unity. The reason for this is because the solutions are being compared to a computational fluid dynamics (CFD) solution where the translational and rotational temperatures are assumed equal. Therefore, for DSMC to best match CFD, the rotational energy is sampled from the

equilibrium distribution at each collision (Z_{rot} = 1.0). The vibrational energy relaxation model used is that based on the work of Millikan and White and the parameters used for each of the molecular species are presented in Table A.2.

One goal of this work is to examine the effects of adding an electronic energy transition algorithm to DSMC solutions of hypersonic (re)entry flows. To that end, the electronic energy levels of all relevant simulated species (O_2, N_2, O, N, NO, O_2^+, N_2^+, O^+, N^+, and NO^+) are included in Cases 2 and 3. The energy levels included can be viewed in Table A.4 through Table A.13. The energy levels for O and N were taken from Johnston[86], while the remaining species were taken from Hash[111]. A more comprehensive set of energy levels could be compiled for O^+ and N^+, but these are the energy levels used by the CFD code to be compared with, as well as the nonequilibrium radiation code.

5.3.3 Chemistry Modeling

The baseline chemistry model is the TCE model using the reaction rates used in LAURA. These rates are listed in Table A.14 as the first rate listed for each reaction. As discussed in Section 2.2.3, the exothermic (reverse) reaction rates are then determined by considering the statistical mechanics equilibrium constant, and then the coefficients are chosen from those in the literature to most closely match the rate as computed by statistical mechanics.

The other chemistry model, which is one of the main contributions, is the Q-K chemistry model and the extensions to charged species. The characteristic temperatures and reference parameters for vibrational relaxation can be found in Table A.1 and Table A.3, respectively. Additionally, the parameters required to account for the statistical mechanics equilibrium constant and adjust the activation energies for recombination and exchange/charge exchange can be found in Table A.16 and Table A.17, respectively. Comparisons of the Q-K reaction set to various rates found in the literature can be viewed in Appendix C.

5.3.4 Electric Field Modeling

The electric field model implemented in the current study, which was also added to DAC, is a hybrid of Bird's model[26] and that of Boyd[30]. In this model, the electron particles are moved along with their associated ion during the movement portion of the DSMC algorithm. However, the electrons retain their individual velocity components, which are used in the collision portion of the DSMC algorithm. Neither the electrons nor ions actually experience an electric field, in that their velocity components are not adjusted to account for an electric field as one is not computed.

5.3.5 Gas-Surface Interactions

The surface catalycity must be treated differently with the present DSMC simulations because the CFD solutions use the fully-catalytic surface boundary condition to account for the higher surface temperatures in the continuum regime. However, there

is evidence[25] that, for surface temperatures such as those at the higher altitudes for the FIRE II experiment, the catalycity of neutral atomic species recombining is much closer to zero. Therefore, the interaction of particles with the vehicle surface is managed by assuming both a fully catalytic surface as was used with the CFD solution for comparison and also a partially catalytic surface that only allows charged species to become neutralized. The fully catalytic simulations will be referred to simply by their case number (i.e., Case 1) and the partially catalytic simulations will have an extra notation indicating that it is partially catalytic (i.e., Case 1^{pc}). The remaining collisions (neutral molecules), along with the recombined particles, are then allowed to reflect diffusely from the surface, after thermally accommodating to the specified wall temperature.

5.4 FIRE II Simulations

In this section, a progression of DSMC solutions is discussed and compared with CFD beginning with a traditional DSMC solution without electronic energy levels (Case 1), followed by the addition of electronic energy levels (Case 2), concluding with the Q-K chemistry model (Case 3). At the end of the section, a discussion of the surface heating, both convective and radiative, is included where the DSMC rates are compared to both the CFD solution and values inferred from flight.

5.4.1 Baseline Solution

The baseline solution, referred to as Case 1 in Table 5.1, is the FIRE II simulation at 1634 seconds using the TCE chemistry model without the addition of electronic energy levels. Various temperatures for this case are compared to that from the CFD solution in Figure 5.2. Clearly, the exclusion of electronic energy levels from the DSMC solution changes the shock-layer profile. The shock standoff distance of the DSMC solution is nearly 40% greater than that of the CFD solution, while the shock-layer temperature is also greater than that predicted by CFD. It can be seen that, inside the shock layer of the DSMC solution, the temperatures are not in equilibrium. This has been reported in Refs. [25] and [4] as an effect of the addition of ionization physics at this altitude. There is some scatter present in the data for both the rotational and vibrational temperatures, which may be caused by the low number density of molecular species in the flow field. The spike in vibrational temperature outside of the shock layer is the result of trace species of vibrationally excited molecules that have escaped from the shock layer. This is a phenomenon typical of flows such as this in DSMC simulations. Since the physics are clearly not the same, comparisons of species concentrations are not provided for this case.

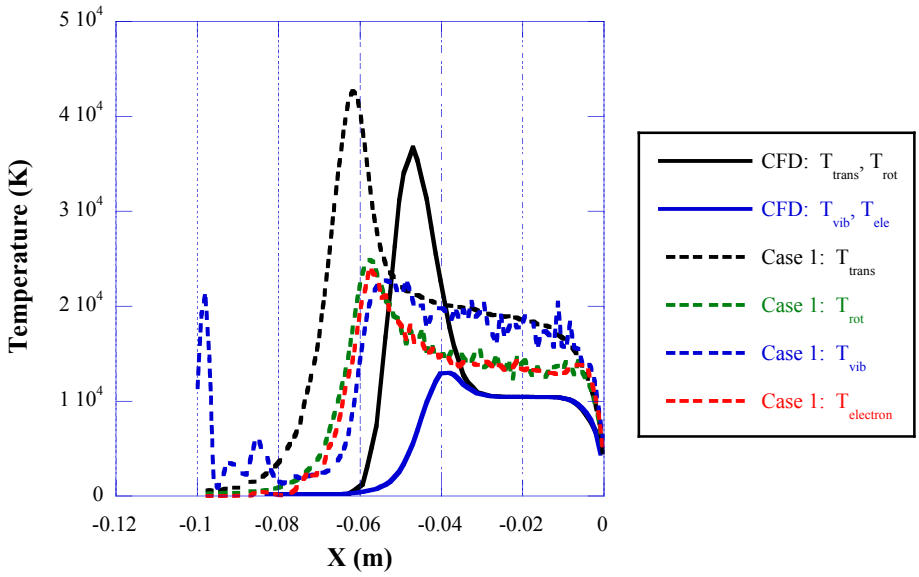

Figure 5.2: Translational temperature comparison between CFD and Case 1 (no electronic energy levels).

5.4.2 Addition of Electronic Energy Levels

Electronic energy levels were included in DSMC Case 2 and are more appropriate for comparison to the CFD solution. The various temperature profiles from CFD and Case 2 are compared in Figure 5.3. The DSMC shock standoff distance has been reduced as compared to Case 1 and now the location and magnitude of the peak translational temperatures of the CFD and DSMC Case 2 solutions compare quite well. The differences between the solutions are the larger equilibrium temperature within the shock layer and the increased electronic temperature that persists upstream of the location of maximum translational temperature, which is discussed below.

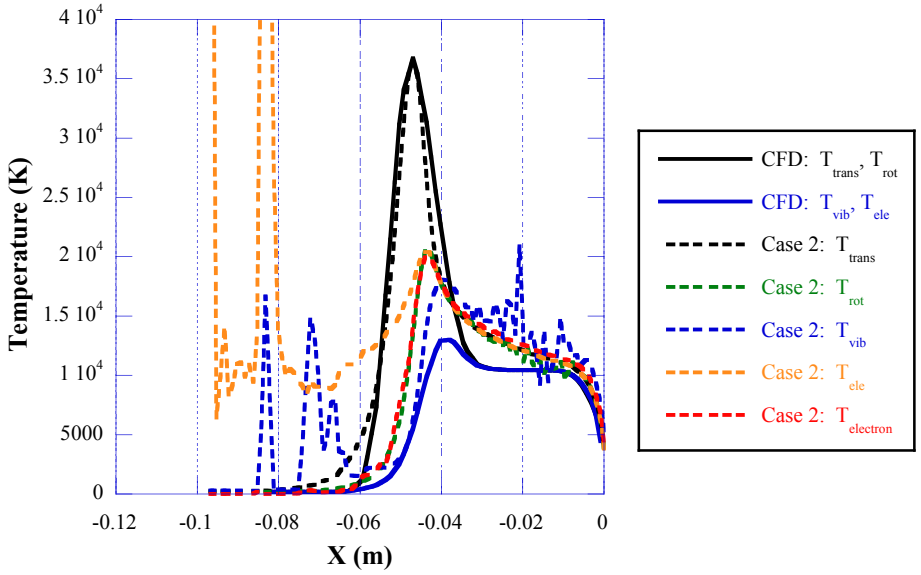

Figure 5.3: Comparison of temperature profiles between the CFD solution and Case 2 (electronic energy levels added).

Comparisons of species mole fractions between the CFD solution and Case 2 are presented in Figure 5.4 and Figure 5.5 for neutral and charged species, respectively. In general, the species fractions compare well. As with the vibrational and rotational temperatures, there is noise in the mole fractions extracted from the DSMC simulation below around 0.05% because of the low sample size of these species. The DSMC solution contains trace species further upstream of the shock front as compared to the CFD solution. This is most likely caused by rarefaction effects where there are insufficient collisions to keep all particles within the shock layer. This also accounts for the increased electronic temperatures upstream of the maximum translational temperature as seen in Figure 5.3, and is analogous to what occurs with the vibrational temperature upstream of the shock, except with the electronic energy levels, not only do the molecules carry energy upstream of the shock, but also the atomic species. Even for a small population of excited particles, the electronic temperature can be large.

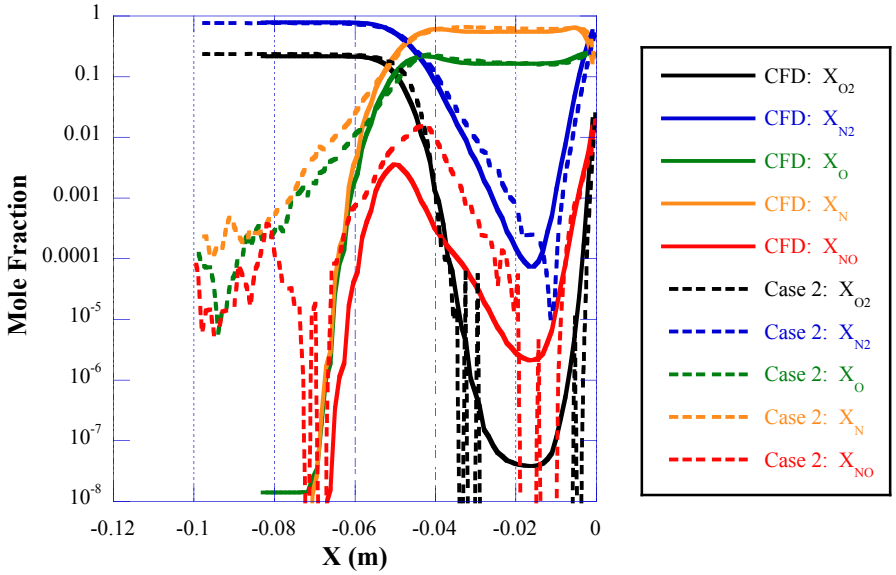

Figure 5.4: Comparison of neutral species mole fractions between the CFD solution and Case 2.

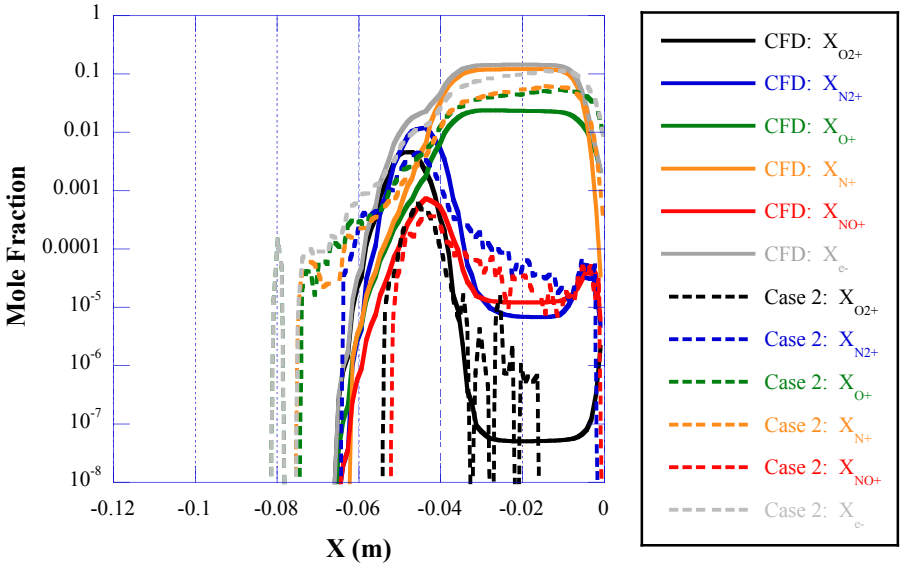

Figure 5.5: Comparison of charged species mole fractions between the CFD solution and Case 2.

5.4.3 Quantum-Kinetic Solution

As was discussed earlier, DSMC Case 3 switches chemistry modules from the traditional TCE model to the new Q-K model. The various temperature profiles from CFD and Case 3 are compared in Figure 5.6. For this case, the peak translational temperature is slightly lower and moved upstream as compared to the CFD solution. This discrepancy may attributable both to the difference in the resultant equilibrium reaction rates discussed in Chapter 4 and also because the Q-K model does not rely

on equilibrium-based information. If the Q-K reaction rates are compared to the reaction rates used in the CFD solution (the first referenced rate in each figure) in Appendix C, there can be a large discrepancy, even though the Q-K rate is generally still well within the spread of reported reaction rates.

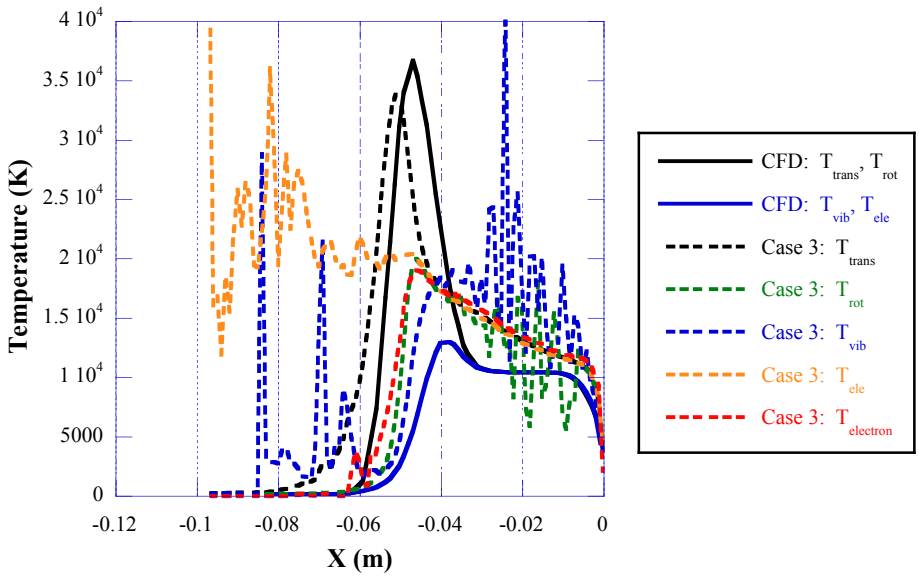

Figure 5.6: Comparison of temperature profiles between the CFD solution and Case 3 (with electronic energy levels and Q-K chemistry).

Comparisons of species mole fractions are presented between the CFD solution and DSMC Case 3 in Figure 5.7 and Figure 5.8 for neutral and charged species, respectively. Again, the mole fractions generally compare well between the CFD and Case 2 solutions with some notable differences. One difference is again the presence of trace species well upstream of the shock layer.

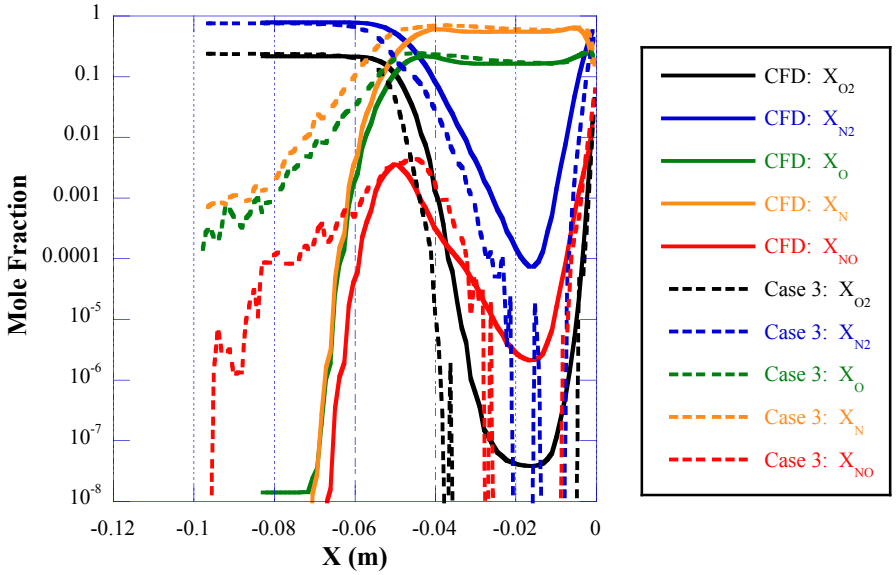

Figure 5.7: Comparison of neutral species mole fractions between the CFD solution and Case 3.

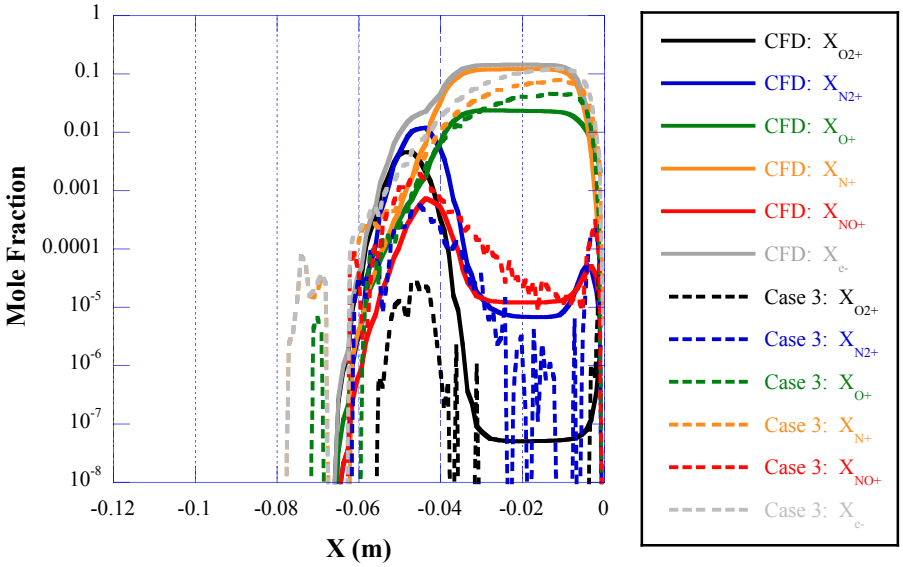

Figure 5.8: Comparison of charged species mole fractions between the CFD solution and Case 3.

5.4.4 Comparison of Surface Heating

The FIRE II calorimeter data presented by Cornette[21] provide heating values that contain the convective heating plus the contribution of the radiative flux absorbed by the beryllium calorimeter. In order to compare to these data, the code HARA was used to post-process the flow field solutions to obtain the non-equilibrium radiation heating to the surface. It was determined[21] that the fraction of the radiative flux absorbed by the calorimeter, α, was 0.72.

The computed heat flux to the surface of the vehicle is compared to the values inferred from the flight data at a radial location of approximately 0.02 m in Table 5.3. When comparing the convective heating component between the CFD and fully catalytic DSMC solutions including electronic energy levels, very good agreement is found. The solutions agree to within 1% of each other. However, DSMC Case 1, without electronic energy levels, has a convective heating rate approximately 15 W/cm^2 higher, again highlighting the fact that electronic energy levels are required for the simulation. When the cases with electronic energy levels are compared to the inferred flight value, the convective heating is over-predicted by 34%. If the partially catalytic solutions are then considered, they under-predict the convective heating by around 15%. Therefore, the surface of the flight vehicle was likely at least partially catalytic to atomic recombination.

The radiative heating component is also listed in Table 5.3 in the third column. Only the DSMC simulations with electronic energy levels modeled have been post-processed for radiative heating. Because of the differences in molar fractions between the DSMC simulations and the CFD solution, there is about a 10 W/cm^2 increase in radiative heating for the DSMC simulations. There are generally more species present in the shock layer that radiate in the DSMC simulations, such as N, O, and N_2^+. The increase in radiative heating for the partially catalytic DSMC simulations is accounted for by the increased levels of N and O near the surface since these species do not recombine upon colliding with the wall.

Table 5.3: FIRE II surface heating at r = 0.02 m.

Case	Convective Heating (W/cm^2)	Radiative Heating (W/cm^2)	$q_{conv}+\alpha q_{rad}$ (W/cm^2)
CFD	217	25	235
Case 1	230	---	---
Case 1^{pc}	148	---	---
Case 2	219	36	245
Case 2^{pc}	133	95	201
Case 3	217	35	242
Case 3^{pc}	137	72	189
Flight	162	18	175

Chapter 6: Conclusions

This chapter contains a summary of the results of this thesis, the original contributions made to the field, and identifies future research directions.

6.1 Summary of Results

Extensions to the recently introduced kinetic-theory approach for computing chemical reaction rates (the Q-K method) have been developed and validated for DSMC for electronic energy level transitions and reactions involving charged species. These new models make use of the principles of microscopic reversibility and molecular-level energy exchange to predict the probability that an energy level transition or a chemical reaction occurs during a collision between two particles. Procedures have been defined that are required to implement these models in the DSMC technique.

For each of these new Q-K reaction-rate models, comparisons have been made between the predicted analytic curves, the sampled transition or reaction rates from DSMC simulations, and rates obtained from the literature. The analytic and sampled values compare favorably to the rates from the literature; the historical rates often differ by several orders of magnitude for the same reactions. It should be noted again, however, that the Q-K model is phenomenological in nature and there may be cases for which it leads to rates that are outside of the range of uncertainty of the measured rates. Even so, the usefulness of these models has been shown as engineering models, especially where there are no data or the uncertainty in reported values is quite large. If there are reactions for which there is a high degree of certainty in the reported rate, they can be specified to use the TCE model.

The proposed extensions to the Q-K model were implemented in the DSMC Analysis Code (DAC) of NASA and tested on the Project Fire II flight experiment. The addition of electronic energy levels to the standard chemistry model resulted in better agreement between DSMC and CFD. Both the location and magnitude of the maximum translational temperature agree. The DSMC solution without electronic energy levels had predicted a higher peak translational temperature and shock thickness approximately 40% greater than the CFD solution. However, because of rarefaction effects, trace species with elevated electronic energies were found upstream of the shock layer, resulting in an elevated electronic temperature. Similar results were found when the chemistry model was changed from the TCE model to the Q-K model. The only major difference was a slightly thicker shock layer and lower peak translational temperature because of the differences in resultant reaction rates. Most likely, the Q-K model better represents the reaction rates because it is a phenomenological approach, whereas for the other models, the reaction rates are extrapolated from low temperature experiments.

Once surface convective heating had been obtained, the flow field was post-processed using the HARA non-equilibrium radiation solver to compare DSMC, CFD and values obtained from the flight experiment. The convective heating of the fully catalytic DSMC simulations with electronic energy levels included compared to within 1% of values obtained using CFD. These values are, however, around 34%

higher than the value inferred from flight. When a partially catalytic surface boundary condition is employed, allowing only electron/ion recombinations, the convective heating dropped to levels on the order of 15% lower than the flight value. Therefore, the fully catalytic and partially catalytic simulations have been shown to bound the flight value of convective heating. The radiative heating computed from the DSMC simulations is around 10 W/cm^2 higher than that of the CFD simulation, which is caused by slightly larger amounts of N, O, and N_2^+. However, the nonequilibrium radiation solver is required to make certain assumptions in its calculations, so a direct input of the sampled non-Boltzmann distribution of electronic energy levels from the DSMC simulation would negate the necessity of the assumptions.

6.2 Contributions

The ability to simulate rarefied, ionized, hypersonic flows has been added to the suite of simulation capabilities for the National Aeronautics and Space Administration. Specifically, physical models for the treatment of charged particles using the DSMC method have been implemented in DAC. It has been shown that the inclusion of electronic energy levels, which few other DSMC solvers have the capability to do, is necessary for lunar-reentry velocity missions for the accurate prediction of shock shape and surface heating. The ability to predict electronic energy level transitions and resulting distributions using only energy level data has been developed as a result of this thesis. Also, the QK chemistry model was extended to include reactions involving charged species. This model allows the inclusion of chemical reactions for which specific reaction rate data is not known and may be more appropriate for non-equilibrium conditions. Both electronic energy level transition rates and chemical reaction rates have been shown to agree well with rates from the literature.

Appendices

Appendix A: Species and Chemistry Data

Table A.1: Parameters used in the VHS molecular model and characteristic temperatures.

Species	T_{ref} (K)	d_{ref} (m)	ω	Θ_{rot} (K)	Θ_{vib} (K)	Θ_{diss} (K)	Θ_{ion} (K)
O_2	288.0	3.96E-10	0.77	2.080	2256.0	59500.0	140066.5
N_2	288.0	4.07E-10	0.74	2.874	3371.0	11355.0	180798.3
O	288.0	3.00E-10	0.75	-	-	-	158053.5
N	288.0	3.00E-10	0.75	-	-	-	168613.6
NO	288.0	4.00E-10	0.79	2.080	2719.0	75500.0	107457.8
O_2^+	288.0	3.96E-10	0.77	2.080	2256.0	59500.0	-
N_2^+	288.0	4.07E-10	0.74	2.874	3371.0	11355.0	-
O^+	288.0	3.00E-10	0.75	-	-	-	-
N^+	288.0	3.00E-10	0.75	-	-	-	-
NO^+	288.0	4.00E-10	0.79	2.080	2719.0	75500.0	-
e^-	288.0	1.00E-10	0.70	-	-	-	-

Table A.2: Internal energy relaxation parameters.

Species	Z_{rot}	$Z_{vib} = \left(C_1/T^{\omega}\right)\exp\left(C_2 T^{-1/3}\right)$	
		C_1	C_2
O_2	1	56.5	153.5
N_2	1	9.1	220
NO	1	9.1	220
O_2^+	1	56.5	153.5
N_2^+	1	9.1	220
NO^+	1	9.1	220

Table A.3: Parameters used in new vibrational relaxation model.

	O_2	N_2	NO
Z_{ref}	17900.0	52500.0	123000.0
T_{ref} (K)	2256.0	3371.0	2791.0
Θ_d (K)	59500.0	113500.0	75500.0

Table A.4: Electronic energy levels of O_2.

Level	g	E_{el} (J)	State
1	3	0.0000E+01	$X^3\Sigma_g^-$
2	2	1.5728E-19	$a^1\Delta_g$
3	1	2.6211E-19	$b^1\Sigma_g^+$
4	1	6.5663E-19	$c^1\Sigma_u^-$
5	6	6.8912E-19	$A'^3\Delta_u$
6	3	7.0306E-19	$A^3\Sigma_u^+$

Level	g	E_{el} (J)	State
7	3	9.9267E-19	$B^3\Sigma_u^-$

Table A.5: Electronic energy levels of N_2.

Level	g	E_{el} (J)	State
1	1	0.0000E+01	$X^1\Sigma_g^+$
2	3	9.9727E-19	$A^3\Sigma_u^+$
3	6	1.1843E-18	$B^3\Pi_g$
4	6	1.1881E-18	$W^3\Delta_u$
5	3	1.3165E-18	$B'^3\Sigma_u^-$
6	1	1.3538E-18	$a'^1\Sigma_u^-$
7	2	1.3763E-18	$a^1\Pi_g$
8	2	1.4483E-18	$w^1\Delta_u$
9	5	1.5415E-18	$A'^5\Sigma_g^+$
10	1	1.6925E-18	$^1\Sigma_g^+$
11	6	1.7242E-18	$G^3\Delta_g$
12	6	1.7707E-18	$C^3\Pi_u$
13	10	1.8474E-18	$C''^5\Pi_u$
14	6	1.9388E-18	$C'^3\Pi_u$
15	6	2.0778E-18	$H^3\Phi_u$

Table A.6: Electronic energy levels of O.

Level	g	E (J)	Core	Config.	Term
1	9	1.55E-21	$2s^2$	$2p^4$	^3P
2	5	3.15E-19	$2s^2$	$2p^4$	^1D
3	1	6.71E-19	$2s^2$	$2p^4$	^1S
4	5	1.47E-18	$2s^3 2p^2$	3s	$^5S^o$
5	3	1.53E-18	$2s^3 2p^2$	3s	$^3S^o$
6	15	1.72E-18	2s	3p	^5P
7	9	1.76E-18	$2s^3 2p^2$	3p	^3P
8	5	1.90E-18	$2s^3 2p^2$	4s	$^5S^o$
9	3	1.91E-18	$2s^3 2p^2$	4s	$^3S^o$
10	25	1.94E-18	$2s^3 2p^2$	3d	$^5D^o$
11	15	1.94E-18	$2s^3 2p^2$	3d	$^3D^o$
12	15	1.97E-18	$2s^3 2p^2$	4p	^5P
13	9	1.98E-18	$2s^3 2p^2$	4p	^3P
14	15	2.01E-18	$2s^3 2p^2$	3s	$^3D^o$
15	5	2.03E-18	$2s^3 2p^2$	5s	$^5S^o$
16	3	2.03E-18	$2s^3 2p^2$	5s	$^3S^o$
17	5	2.04E-18	$2s^3 2p^2$	3s	$^1D^o$
18	25	2.04E-18	$2s^3 2p^2$	4d	$^5D^o$

Level	g	E (J)	Core	Config.	Term
19	15	2.04E-18	$2s^3 2p^2$	4d	$^3D^o$
20	35	2.05E-18	$2s^3 2p^2$	4f	^5F
21	21	2.05E-18	$2s^3 2p^2$	4f	^3F
22	15	2.06E-18	$2s^3 2p^2$	5p	^5P
23	9	2.06E-18	$2s^3 2p^2$	5p	^3P
24	25	2.09E-18	$2s^3 2p^2$	5d	$^5D^o$
25	15	2.09E-18	$2s^3 2p^2$	5d	$^3D^o$
26	35	2.09E-18	$2s^3 2p^2$	5f	^5F
27	21	2.09E-18	$2s^3 2p^2$	5f	^3F
28	288	2.12E-18	$2s^3 2p^2$	n=6	-
29	392	2.14E-18	$2s^3 2p^2$	n=7	-
30	512	2.15E-18	$2s^3 2p^2$	n=8	-
31	648	2.15E-18	$2s^3 2p^2$	n=9	-
32	800	2.16E-18	$2s^3 2p^2$	n=10	-

Table A.7: Electronic energy levels of N.

Level	g	E_{el} (J)	Core	Config.	Term
1	4	0.0000E+01	$2s^2$	$2p^3$	$^4S^o$
2	10	3.8195E-19	$2s^2$	$2p^3$	$^2D^o$
3	6	5.7287E-19	$2s^2$	$2p^3$	$^2P^o$
4	12	1.6554E-18	$2s^2 2p^2$	3s	^4P
5	6	1.7122E-18	$2s^2 2p^2$	3s	^2P
6	12	1.7507E-18	2s	$2p^4$	^4P
7	2	1.8589E-18	$2s^2 2p^2$	3p	$^2S^o$
8	20	1.8839E-18	$2s^2 2p^2$	3p	$^4D^o$
9	12	1.8973E-18	$2s^2 2p^2$	3p	$^4P^o$
10	4	1.9219E-18	$2s^2 2p^2$	3p	$^4S^o$
11	10	1.9235E-18	$2s^2 2p^2$	3p	$^2D^o$
12	6	1.9426E-18	$2s^2 2p^2$	3p	$^2P^o$
13	10	1.9798E-18	$2s^2 2p^2$	3s	^2D
14	12	2.0598E-18	$2s^2 2p^2$	4s	^4P
15	6	2.0698E-18	$2s^2 2p^2$	4s	^2P
16	6	2.0784E-18	$2s^2 2p^2$	3d	^2P
17	28	2.0802E-18	$2s^2 2p^2$	3d	^4F
18	14	2.0828E-18	$2s^2 2p^2$	3d	^2F
19	12	2.0828E-18	$2s^2 2p^2$	3d	^4P
20	20	2.0859E-18	$2s^2 2p^2$	3d	^4D
21	10	2.0884E-18	$2s^2 2p^2$	3d	^2D
22	2	2.1151E-18	$2s^2 2p^2$	4p	$^2S^o$
23	20	2.1220E-18	$2s^2 2p^2$	4p	$^4D^o$
24	12	2.1258E-18	$2s^2 2p^2$	4p	$^4P^o$
25	10	2.1300E-18	$2s^2 2p^2$	4p	$^2D^o$
26	4	2.1343E-18	$2s^2 2p^2$	4p	$^4S^o$
27	6	2.1377E-18	$2s^2 2p^2$	4p	$^2P^o$
28	90	2.1912E-18	$2s^2 2p^2$	$4d^2P,4d^4F,4d^4D,4d^4F,4d^4P,4d^2D$	
29	126	2.1946E-18	$2s^2 2p^2$	$4f^4D,4f^4F,4f^4G,4f^2D,4f^2F,4f^2G$	
30	450	2.2368E-18	$2s^2 2p^2$	n=5	
31	648	2.2703E-18	$2s^2 2p^2$	n=6	
32	822	2.2864E-18	$2s^2 2p^2$	n=7	
33	1152	2.2968E-18	$2s^2 2p^2$	n=8	
34	1458	2.3040E-18	$2s^2 2p^2$	n=9	

Level	g	E_{el} (J)	Core	Config.	Term
35	1800	2.3091E-18	$2s^2 2p^2$	n=10	

Table A.8: Electronic energy levels of NO.

Level	g	E_{el} (J)	State
1	4	0.0000E+01	$X^2\Pi_r$
2	8	7.5485E-19	$a^4\Pi_i$
3	2	8.7218E-19	$A^2\Sigma^+$
4	4	9.1115E-19	$B^2\Pi_r$
5	4	9.5349E-19	$b^4\Sigma^-$
6	4	9.7336E-19	$L'^2\Phi$
7	4	1.0343E-18	$C^2\Pi$
8	2	1.0533E-18	$D^2\Sigma$
9	4	1.1979E-18	$B'^2\Delta$
10	2	1.2032E-18	$E^2\Sigma^+$
11	4	1.2269E-18	$F^2\Delta$
12	4	1.2401E-18	$H^2\Pi$
13	2	1.2410E-18	$H'^2\Sigma^+$
14	2	1.2485E-18	$G^2\Sigma^-$
15	2	1.2515E-18	$I^2\Sigma^+$
16	4	1.2580E-18	$L^2\Pi$

Table A.9: Electronic energy levels of O_2^+.

Level	g	E_{el} (J)	State
1	4	0.0000E+01	$X^2\Pi_g$
2	8	6.5380E-19	$a^4\Pi_u$
3	4	8.0594E-19	$A^2\Pi_u$
4	6	8.0650E-19	${}^6\Sigma_u^+$
5	4	8.6013E-19	$b^4\Sigma_g^+$
6	2	9.2966E-19	$B^2\Sigma_u^+$
7	4	9.8329E-19	$c^4\Sigma_g^-$
8	4	1.0568E-18	$C^2\Phi_u$
9	4	1.2177E-18	$D^2\Pi_u$
10	4	1.2276E-18	$E^2\Delta_g$
11	8	1.3011E-18	$d^4\Delta_g$
12	4	1.3111E-18	$F^2\Pi_g$
13	2	1.3243E-18	$G^2\Sigma_g^-$

Level	g	E_{el} (J)	State
14	2	1.3786E-18	$H^2\Sigma_g^+$
15	4	1.4302E-18	$e^4\Sigma_u^+$

Table A.10: Electronic energy levels of N_2^+.

Level	g	E_{el} (J)	State
1	2	0.0000E+01	$X^2\Sigma_g^+$
2	4	1.8211E-19	$A^2\Pi_u$
3	2	5.0578E-19	$B^2\Sigma_u^+$
4	4	5.0654E-19	$a^4\Sigma_u^+$
5	8	8.2636E-19	$b^4\Pi_g$
6	8	9.1377E-19	$c^4\Pi_u$
7	4	1.0492E-18	$C^2\Pi_g$
8	4	1.0528E-18	$d^4\Sigma_u^-$
9	4	1.1323E-18	$e^4\Sigma_g^+$
10	4	1.1621E-18	$D^2\Phi_u$
11	8	1.1919E-18	$f^4\Pi_u$
12	8	1.2316E-18	$g^4\Delta_u$
13	4	1.2713E-18	$E^2\Delta_u$
14	4	1.2733E-18	$E^2\Delta_u$
15	2	1.2831E-18	$E^2\Delta_u$
16	2	1.3309E-18	$E^2\Delta_u$
17	4	1.4302E-18	$E^2\Delta_u$

Table A.11: Electronic energy levels of O^+.

Level	g	E_{el} (J)	Core	Config.	Term
1	4	0.0000E+01	$2s^2$	$2p^3$	$^4S^o$
2	10	5.3270E-19	$2s^2$	$2p^3$	$^2D^o$
3	6	8.0386E-19	$2s^2$	$2p^3$	$^2P^o$

Table A.12: Electronic energy levels of N^+.

Level	g	E_{el} (J)	Core	Config.	Term
1	9	0.0000E+01	$2s^2$	$2p^2$	^3P
2	5	3.0424E-19	$2s^2$	$2p^2$	^1D
3	1	6.4929E-19	$2s^2$	$2p^2$	^1S
4	15	1.8324E-18	2s	$2p^3$	$^3D^o$
5	9	2.1696E-18	2s	$2p^3$	$^3P^o$
6	5	2.8642E-18	2s	$2p^3$	$^1D^o$

Level	g	E_{el} (J)	Core	Config.	Term
7	12	2.9610E-18	$2s^2 2p$	3s	$^3P^o$

Table A.13: Electronic energy levels of NO^+.

Level	g	E_{el} (J)	State
1	1	0.0000E+01	$X^1\Sigma^+$
2	3	1.0367E-18	$a^3\Sigma^+$
3	6	1.1771E-18	$b^3\Pi$
4	6	1.2293E-18	$c^3\Delta$
5	3	1.3457E-18	$d^3\Sigma^-$
6	1	1.3814E-18	$B^1\Sigma^-$
7	2	1.4194E-18	$C^1\Delta$
8	2	1.4595E-18	$D^1\Pi$

Table A.14: Endothermic chemical reaction rate coefficients (m^3/molecule/s) used in the TCE model (the first rate listed for each reaction is the rate used in the simulations). $k_f = aT^b \exp(-E_a/kT)$

Number	Reaction	a	b	$\overline{\zeta}$	E_a (J)	E_{rx} (J)	Reference
1	$O_2 + O_2 \rightarrow O + O + O_2$	3.3211E-09	-1.50	1.5	8.1995E-19	-8.1995E-19	Park[63]
		4.5800E-11	-1.00		8.1970E-19	-8.1970E-19	Bird[15]
		5.9780E-12	-1.00		8.2150E-19	-8.2150E-19	Kang[64]
		5.3930E-11	-1.00		8.1970E-19	-8.1970E-19	Gimelshein[65]
2	$O_2 + N_2 \rightarrow O + O + N_2$	3.3211E-09	-1.50	1.5	8.1995E-19	-8.1995E-19	Park[63]
		4.5800E-11	-1.00		8.1970E-19	-8.1970E-19	Bird[15]
		5.9780E-12	-1.00		8.2150E-19	-8.2150E-19	Kang[64]
		1.1980E-11	-1.00		8.1970E-19	-8.1970E-19	Gimelshein[65]
3	$O_2 + O \rightarrow O + O + O$	1.6605E-08	-1.50	1.0	8.1995E-19	-8.1995E-19	Park[63]
		1.3750E-10	-1.00		8.1970E-19	-8.1970E-19	Bird[15]
		5.9780E-12	-1.00		8.2150E-19	-8.2150E-19	Kang[64]
		3.3200E-09	-1.50		8.2140E-19	-8.2140E-19	Ozawa[9]
		1.4980E-10	-1.00		8.1970E-19	-8.1970E-19	Gimelshein[65]
		4.5700E-11	-1.00		8.1970E-19	-8.1970E-19	Johnston[66]
4	$O_2 + N \rightarrow O + O + N$	1.6605E-08	-1.50	1.0	8.1995E-19	-8.1995E-19	Park[63]
		1.3750E-10	-1.00		8.1970E-19	-8.1970E-19	Bird[15]
		5.9780E-12	-1.00		8.2150E-19	-8.2150E-19	Kang[64]
		3.3200E-09	-1.50		8.2140E-19	-8.2140E-19	Ozawa[9]
		5.9930E-12	-1.00		8.1970E-19	-8.1970E-19	Gimelshein[65]
5	$O_2 + NO \rightarrow O + O + NO$	3.3211E-09	-1.50	1.0	8.1995E-19	-8.1995E-19	Park[63]
		4.5800E-11	-1.00		8.1970E-19	-8.1970E-19	Bird[15]
		5.9780E-12	-1.00		8.2150E-19	-8.2150E-19	Kang[64]
		5.9930E-12	-1.00		8.1970E-19	-8.1970E-19	Gimelshein[65]
6	$O_2 + O_2^+ \rightarrow O + O + O_2^+$	3.3211E-09	-1.50	1.5	8.1995E-19	-8.1995E-19	Park[63]
		4.5800E-11	-1.00		8.1970E-19	-8.1970E-19	Bird[15]
		5.9780E-12	-1.00		8.2150E-19	-8.2150E-19	Kang[64]
		5.3930E-11	-1.00		8.1970E-19	-8.1970E-19	Gimelshein[65]

Number	Reaction	a	b	$\overline{\zeta}$	E_a (J)	E_{rx} (J)	Reference
7	$O_2 + N_2^+ \rightarrow O + O + N_2^+$	3.3211E-09	-1.50	1.5	8.1995E-19	-8.1995E-19	Park[63]
		4.5800E-11	-1.00		8.1970E-19	-8.1970E-19	Bird[15]
		5.9780E-12	-1.00		8.2150E-19	-8.2150E-19	Kang[64]
		1.1980E-11	-1.00		8.1970E-19	-8.1970E-19	Gimelshein[65]
8	$O_2 + O^+ \rightarrow O + O + O^+$	1.6605E-08	-1.50	1.0	8.1995E-19	-8.1995E-19	Park[63]
		1.3750E-10	-1.00		8.1970E-19	-8.1970E-19	Bird[15]
		5.9780E-12	-1.00		8.2150E-19	-8.2150E-19	Kang[64]
		3.3200E-09	-1.50		8.2140E-19	-8.2140E-19	Ozawa[9]
		1.4980E-10	-1.00		8.1970E-19	-8.1970E-19	Gimelshein[65]
		4.5700E-11	-1.00		8.1970E-19	-8.1970E-19	Johnston[66]
9	$O_2 + N^+ \rightarrow O + O + N^+$	1.6605E-08	-1.50	1.0	8.1995E-19	-8.1995E-19	Park[63]
		1.3750E-10	-1.00		8.1970E-19	-8.1970E-19	Bird[15]
		5.9780E-12	-1.00		8.2150E-19	-8.2150E-19	Kang[64]
		3.3200E-09	-1.50		8.2140E-19	-8.2140E-19	Ozawa[9]
		5.9930E-12	-1.00		8.1970E-19	-8.1970E-19	Gimelshein[65]
10	$O_2 + NO^+ \rightarrow O + O + NO^+$	3.3211E-09	-1.50	1.0	8.1995E-19	-8.1995E-19	Park[63]
		4.5800E-11	-1.00		8.1970E-19	-8.1970E-19	Bird[15]
		5.9780E-12	-1.00		8.2150E-19	-8.2150E-19	Kang[64]
		5.9930E-12	-1.00		8.1970E-19	-8.1970E-19	Gimelshein[65]
11	$N_2 + O_2 \rightarrow N + N + O_2$	1.1620E-08	-1.60	0.5	1.5630E-18	-1.5630E-18	Park[63]
		6.1700E-09	-1.60		1.5610E-18	-1.5610E-18	Bird[15]
		3.1550E-13	-0.50		1.5600E-18	-1.5600E-18	Kang[64]
		4.9800E-08	-1.60		1.5630E-18	-1.5630E-18	Ozawa[9]
		7.9700E-13	-0.50		1.5610E-18	-1.5610E-18	Boyd[67]
		3.1870E-13	-0.50		1.5610E-18	-1.5610E-18	Gimelshein[65]
12	$N_2 + N_2 \rightarrow N + N + N_2$	1.1620E-08	-1.60	1.0	1.5630E-18	-1.5630E-18	Park[63]
		6.1700E-09	-1.60		1.5610E-18	-1.5610E-18	Bird[15]
		3.1550E-13	-0.50		1.5600E-18	-1.5600E-18	Kang[64]
		1.1600E-08	-1.60		1.5630E-18	-1.5630E-18	Ozawa[9]
		7.9700E-13	-0.50		1.5610E-18	-1.5610E-18	Boyd[67]
13	$N_2 + O \rightarrow N + N + O$	4.9980E-08	-1.60	0.5	1.5630E-18	-1.5630E-18	Park[63]
		1.8500E-08	-1.60		1.5610E-18	-1.5610E-18	Bird[15]
		3.1550E-13	-0.50		1.5600E-18	-1.5600E-18	Kang[64]
		7.1400E-08	-1.50		1.5630E-18	-1.5630E-18	Boyd[67]
		3.1870E-13	-0.50		1.5610E-18	-1.5610E-18	Gimelshein[65]
14	$N_2 + N \rightarrow N + N + N$	4.9980E-08	-1.60	1.0	1.5630E-18	-1.5630E-18	Park[63]
		1.8500E-08	-1.60		1.5610E-18	-1.5610E-18	Bird[15]
		6.7830E-08	-1.50		1.5600E-18	-1.5600E-18	Kang[64]
		7.1400E-08	-1.50		1.5630E-18	-1.5630E-18	Boyd[67]
		6.9000E-08	-1.50		1.5610E-18	-1.5610E-18	Gimelshein[65]
15	$N_2 + NO \rightarrow N + N + NO$	1.1620E-08	-1.60	0.5	1.5630E-18	-1.5630E-18	Park[63]
		6.1700E-09	-1.60		1.5610E-18	-1.5610E-18	Bird[15]
		3.1550E-13	-0.50		1.5600E-18	-1.5600E-18	Kang[64]
		4.9800E-08	-1.60		1.5630E-18	-1.5630E-18	Ozawa[9]
		7.9700E-13	-0.50		1.5610E-18	-1.5610E-18	Boyd[67]
		3.1870E-13	-0.50		1.5610E-18	-1.5610E-18	Gimelshein[65]
16	$N_2 + O_2^+ \rightarrow N + N + O_2^+$	1.1620E-08	-1.60	0.5	1.5630E-18	-1.5630E-18	Park[63]
		6.1700E-09	-1.60		1.5610E-18	-1.5610E-18	Bird[15]

Number	Reaction	a	b	$\overline{\zeta}$	E_a (J)	E_{rx} (J)	Reference
		3.1550E-13	-0.50		1.5600E-18	-1.5600E-18	Kang[64]
		4.9800E-08	-1.60		1.5630E-18	-1.5630E-18	Ozawa[9]
		7.9700E-13	-0.50		1.5610E-18	-1.5610E-18	Boyd[67]
		3.1870E-13	-0.50		1.5610E-18	-1.5610E-18	Gimelshein[65]
17	$N_2 + N_2^+ \rightarrow N + N + N_2^+$	1.1620E-08	-1.60	1.0	1.5630E-18	-1.5630E-18	Park[63]
		6.1700E-09	-1.60		1.5610E-18	-1.5610E-18	Bird[15]
		3.1550E-13	-0.50		1.5600E-18	-1.5600E-18	Kang[64]
		1.1600E-08	-1.60		1.5630E-18	-1.5630E-18	Ozawa[9]
		7.9700E-13	-0.50		1.5610E-18	-1.5610E-18	Boyd[67]
18	$N_2 + O^+ \rightarrow N + N + O^+$	4.9980E-08	-1.60	0.5	1.5630E-18	-1.5630E-18	Park[63]
		1.8500E-08	-1.60		1.5610E-18	-1.5610E-18	Bird[15]
		3.1550E-13	-0.50		1.5600E-18	-1.5600E-18	Kang[64]
		7.1400E-08	-1.50		1.5630E-18	-1.5630E-18	Boyd[67]
		3.1870E-13	-0.50		1.5610E-18	-1.5610E-18	Gimelshein[65]
19	$N_2 + N^+ \rightarrow N + N + N^+$	4.9980E-08	-1.60	1.0	1.5630E-18	-1.5630E-18	Park[63]
		1.8500E-08	-1.60		1.5610E-18	-1.5610E-18	Bird[15]
		6.7830E-08	-1.50		1.5600E-18	-1.5600E-18	Kang[64]
		7.1400E-08	-1.50		1.5630E-18	-1.5630E-18	Boyd[67]
		6.9000E-08	-1.50		1.5610E-18	-1.5610E-18	Gimelshein[65]
20	$N_2 + NO^+ \rightarrow N + N + NO^+$	1.1620E-08	-1.60	0.5	1.5630E-18	-1.5630E-18	Park[63]
		6.1700E-09	-1.60		1.5610E-18	-1.5610E-18	Bird[15]
		3.1550E-13	-0.50		1.5600E-18	-1.5600E-18	Kang[64]
		4.9800E-08	-1.60		1.5630E-18	-1.5630E-18	Ozawa[9]
		7.9700E-13	-0.50		1.5610E-18	-1.5610E-18	Boyd[67]
		3.1870E-13	-0.50		1.5610E-18	-1.5610E-18	Gimelshein[65]
21	$N_2 + e^- \rightarrow N + N + e^-$	9.9670E-27	2.60	0.5	1.5630E-18	-1.5630E-18	Bourdon[68]
		4.9800E-06	-1.60		1.5610E-18	-1.5630E-18	Ozawa[9]
		1.4900E-05	-1.60		1.5610E-18	-1.5610E-18	Park[69]
		1.3450E-10	-1.28		1.5630E-18	-1.5630E-18	Losev[70]
22	$NO + O_2 \rightarrow N + O + O_2$	3.8300E-13	-0.50	1.0	1.0420E-18	-1.0420E-18	Fujita[71]
		6.4760E-10	-1.50		1.0420E-18	-1.0420E-18	Kang[64]
		3.3200E-09	-1.50		8.2140E-19	-8.2140E-19	Ozawa[9]
		8.3000E-15	0.00		1.0420E-18	-1.0420E-18	Park[69]
		6.5900E-10	-1.50		1.0430E-18	-1.0430E-18	Gimelshein[65]
23	$NO + N_2 \rightarrow N + O + N_2$	3.8300E-13	-0.50	1.0	1.0420E-18	-1.0420E-18	Fujita[71]
		6.4760E-10	-1.50		1.0420E-18	-1.0420E-18	Kang[64]
		3.3200E-09	-1.50		8.2140E-19	-8.2140E-19	Ozawa[9]
		8.3000E-15	0.00		1.0420E-18	-1.0420E-18	Park[69]
		6.5900E-10	-1.50		1.0430E-18	-1.0430E-18	Gimelshein[65]
24	$NO + O \rightarrow N + O + O$	7.6600E-13	-0.50	1.0	1.0420E-18	-1.0420E-18	Fujita[71]
		6.4760E-10	-1.50		1.0420E-18	-1.0420E-18	Kang[64]
		8.3000E-15	0.00		1.0420E-18	-1.0420E-18	Ozawa[9]
		1.8300E-13	0.00		1.0420E-18	-1.0420E-18	Park[69]
		1.3180E-08	-1.50		1.0430E-18	-1.0430E-18	Gimelshein[65]
25	$NO + N \rightarrow N + O + N$	7.6600E-13	-0.50	1.0	1.0420E-18	-1.0420E-18	Fujita[71]
		6.4760E-10	-1.50		1.0420E-18	-1.0420E-18	Kang[64]
		3.3200E-09	-1.50		8.2140E-19	-8.2140E-19	Ozawa[9]
		1.8300E-13	0.00		1.0420E-18	-1.0420E-18	Park[69]

Number	Reaction	a	b	$\overline{\zeta}$	E_a (J)	E_{rx} (J)	Reference
		1.3180E-08	-1.50		1.0430E-18	-1.0430E-18	Gimelshein[65]
26	$NO + NO \rightarrow N + O + NO$	3.8300E-13	-0.50	1.0	1.0420E-18	-1.0420E-18	Fujita[71]
		6.4760E-10	-1.50		1.0420E-18	-1.0420E-18	Kang[64]
		3.3200E-09	-1.50		8.2140E-19	-8.2140E-19	Ozawa[9]
		8.3000E-15	0.00		1.0420E-18	-1.0420E-18	Park[69]
		1.3180E-08	-1.50		1.0430E-18	-1.0430E-18	Gimelshein[65]
27	$NO + O_2^+ \rightarrow N + O + O_2^+$	3.8300E-13	-0.50	1.0	1.0420E-18	-1.0420E-18	Fujita[71]
		3.8300E-13	-0.50		1.0430E-18	-1.0430E-18	Bird[15]
		6.4760E-10	-1.50		1.0420E-18	-1.0420E-18	Kang[64]
		3.3200E-09	-1.50		8.2140E-19	-8.2140E-19	Ozawa[9]
		8.3000E-15	0.00		1.0420E-18	-1.0420E-18	Park[69]
		6.5900E-10	-1.50		1.0430E-18	-1.0430E-18	Gimelshein[65]
28	$NO + N_2^+ \rightarrow N + O + N_2^+$	3.8300E-13	-0.50	1.0	1.0420E-18	-1.0420E-18	Fujita[71]
		3.8300E-13	-0.50		1.0430E-18	-1.0430E-18	Bird[15]
		6.4760E-10	-1.50		1.0420E-18	-1.0420E-18	Kang[64]
		3.3200E-09	-1.50		8.2140E-19	-8.2140E-19	Ozawa[9]
		8.3000E-15	0.00		1.0420E-18	-1.0420E-18	Park[69]
		6.5900E-10	-1.50		1.0430E-18	-1.0430E-18	Gimelshein[65]
29	$NO + O^+ \rightarrow N + O + O^+$	7.6600E-13	-0.50	1.0	1.0420E-18	-1.0420E-18	Fujita[71]
		7.6600E-13	-0.50		1.0430E-18	-1.0430E-18	Bird[15]
		6.4760E-10	-1.50		1.0420E-18	-1.0420E-18	Kang[64]
		8.3000E-15	0.00		1.0420E-18	-1.0420E-18	Ozawa[9]
		1.8300E-13	0.00		1.0420E-18	-1.0420E-18	Park[69]
		1.3180E-08	-1.50		1.0430E-18	-1.0430E-18	Gimelshein[65]
30	$NO + N^+ \rightarrow N + O + N^+$	7.6600E-13	-0.50	1.0	1.0420E-18	-1.0420E-18	Fujita[71]
		7.6600E-13	-0.50		1.0430E-18	-1.0430E-18	Bird[15]
		6.4760E-10	-1.50		1.0420E-18	-1.0420E-18	Kang[64]
		3.3200E-09	-1.50		8.2140E-19	-8.2140E-19	Ozawa[9]
		1.8300E-13	0.00		1.0420E-18	-1.0420E-18	Park[69]
		1.3180E-08	-1.50		1.0430E-18	-1.0430E-18	Gimelshein[65]
31	$NO + NO^+ \rightarrow N + O + NO^+$	3.8300E-13	-0.50	1.0	1.0420E-18	-1.0420E-18	Fujita[71]
		3.8300E-13	-0.50		1.0430E-18	-1.0430E-18	Bird[15]
		6.4760E-10	-1.50		1.0420E-18	-1.0420E-18	Kang[64]
		3.3200E-09	-1.50		8.2140E-19	-8.2140E-19	Ozawa[9]
		8.3000E-15	0.00		1.0420E-18	-1.0420E-18	Park[69]
		1.3180E-08	-1.50		1.0430E-18	-1.0430E-18	Gimelshein[65]
32	$N + e^- \rightarrow N^+ + e^- + e^-$	5.8100E-08	-1.00	0.0	2.3220E-18	-2.3220E-18	Park[63]
		4.1500E+03	-3.82		2.3300E-18	-2.3300E-18	Park[60]
		9.0000E-11	-1.00		1.5000E-18	-1.5000E-18	Ozawa[7]
		2.9890E-17	0.60		2.3300E-18	-2.3300E-18	Losev[70]
		5.8100E-08	-1.00		2.3300E-18	-2.3300E-18	Boyd[67]
		1.0000E-14	0.00		2.3300E-18	-2.3300E-18	Bird[15]
		1.8270E+02	-3.14		2.3330E-18	-2.3300E-18	Kang[64]
		8.4340E-14	0.00		2.3300E-18	-2.3300E-18	Farbar[5]
33	$O + e^- \rightarrow O^+ + e^- + e^-$	1.5900E-08	-1.00	0.0	2.1880E-18	-2.1880E-18	Park[63]
		6.4800E+03	-3.78		2.1900E-18	-2.1900E-18	Park[60]
		3.0000E-10	-1.00		1.4000E-18	-1.4000E-18	Ozawa[7]
		8.6350E-18	0.68		2.1810E-18	-2.1810E-18	Losev[70]

Number	Reaction	a	b	$\overline{\zeta}$	E_a (J)	E_{rx} (J)	Reference
		1.5900E-08	-1.00		2.1810E-18	-2.1810E-18	Boyd[67]
		3.0000E-12	0.00		2.1810E-18	-2.1810E-18	Bird[15]
		5.9780E+01	-2.91		2.1810E-18	-2.1810E-18	Kang[64]
		1.0540E-14	0.00		2.1810E-18	-2.1810E-18	Farbar[5]
34	$N_2 + O \rightarrow NO + N$	9.9630E-17	0.10	0.0	5.2470E-19	-5.2470E-19	Fujita[71]
		5.3000E-17	0.10		5.1750E-19	-5.1750E-19	Bird[15]
		1.1620E-16	0.00		5.2460E-19	-5.2460E-19	Kang[64]
		9.4500E-18	0.42		5.9280E-19	-5.9280E-19	Ozawa[9]
		1.0600E-12	-1.00		5.1750E-19	-5.1750E-19	Park[69]
		1.1200E-16	0.00		5.1750E-19	-5.1750E-19	Gimelshein[65]
35	$NO + O \rightarrow O_2 + N$	1.3950E-17	0.00	0.0	2.6790E-19	-2.6790E-19	Park[63]
		3.6000E-22	1.29		2.2380E-19	-2.2380E-19	Bird[15]
		5.3140E-21	1.00		2.7200E-19	-2.7200E-19	Kang[64]
		5.2790E-21	1.00		2.7190E-19	-2.7190E-19	Gimelshein[65]
36	$N + N \rightarrow N_2^+ + e^-$	7.3060E-23	1.50	0.0	9.3190E-19	-9.3190E-19	Park[63]
		3.3870E-17	0.00		9.3200E-19	-9.3200E-19	Park[60]
		2.9800E-20	0.77		9.3400E-19	-9.3400E-19	Bird[15]
		2.3250E-17	0.00		9.3610E-19	-9.3610E-19	Kang[64]
37	$N + O \rightarrow NO^+ + e^-$	8.8010E-18	0.00	0.0	4.4040E-19	-4.4040E-19	Park[63]
		8.7660E-18	0.00		4.4000E-19	-4.4000E-19	Park[60]
		1.4600E-21	1.00		4.4000E-19	-4.4000E-19	Park[69]
		2.5500E-20	0.37		4.4220E-19	-4.4220E-19	Bird[15]
		2.3250E-24	1.50		4.4040E-19	-4.4040E-19	Kang[64]
		1.4990E-20	0.50		4.4730E-19	-4.4730E-19	Gupta[72]
38	$O + O \rightarrow O_2^+ + e^-$	1.1790E-27	2.70	0.0	1.1130E-18	-1.1130E-18	Fujita[71]
		1.8300E-17	0.00		1.1100E-18	-1.1100E-18	Park[60]
		6.4200E-22	0.49		1.1200E-18	-1.1200E-18	Bird[15]
		2.6570E-13	-0.98		1.1160E-18	-1.1160E-18	Kang[64]
39	$N^+ + N_2 \rightarrow N_2^+ + N$	1.6610E-18	0.50	1.0	1.6840E-19	-1.6840E-18	Park[63]
		1.6700E-17	-0.18		1.6700E-19	-1.6700E-19	Bird[15]
		2.3250E-26	2.10		1.6700E-19	-1.6700E-19	Phelps[73]
		3.3540E-19	0.81		1.7950E-19	-1.7950E-19	Kang[64]
40	$O^+ + N_2 \rightarrow N_2^+ + O$	1.5110E-18	0.36	1.0	3.1480E-19	-3.1480E-19	Park[74]
		1.4940E-18	0.36		3.1480E-19	-3.1480E-19	Losev[70]
		1.0550E-16	-0.21		3.0600E-19	-3.0600E-19	Bird[15]
		5.6460E-11	-2.00		3.1750E-19	-3.1750E-19	Kang[64]
41	$O^+ + NO \rightarrow N^+ + O_2$	2.3240E-25	1.90	1.0	3.6730E-19	-3.6730E-19	Park[74]
42	$NO^+ + N \rightarrow N_2^+ + O$	1.1960E-16	0.00	1.0	4.9010E-19	-4.1090E-19	Park[74]
		2.8300E-17	0.40		4.9010E-19	-4.9010E-19	Bird[15]
43	$NO^+ + N \rightarrow O^+ + N_2$	5.6460E-17	-1.08	1.0	1.7670E-19	-1.7670E-19	Park[74]
44	$NO^+ + O \rightarrow N^+ + O_2$	1.6610E-18	0.50	1.0	1.0660E-18	-1.0660E-18	Park[74]
		2.2250E-17	0.31		1.0670E-18	-1.0670E-18	Kang[64]
45	$NO^+ + O \rightarrow O_2^+ + N$	1.1960E-17	0.29	1.0	6.7100E-19	-6.7100E-19	Fujita[71]
46	$NO^+ + O_2 \rightarrow O_2^+ + NO$	3.9850E-17	0.41	1.5	5.4010E-19	-5.4010E-19	Park[74]
		3.9850E-17	0.00		4.5010E-19	-4.5010E-19	Losev[70]
		1.7200E-14	-0.17		4.4730E-19	-4.4730E-19	Bird[15]
		2.9890E-15	0.17		4.5560E-19	-4.5560E-19	Kang[64]
47	$O_2^+ + N \rightarrow N^+ + O_2$	1.4450E-16	0.14	1.0	3.9490E-19	-3.9490E-19	Park[74]

Number	Reaction	a	b	$\overline{\zeta}$	E_a (J)	E_{rx} (J)	Reference
48	$O_2^+ + N_2 \rightarrow N_2^+ + O_2$	1.6440E-17	0.00	1.5	5.6190E-19	-5.6190E-19	Park[74]
49	$O_2^+ + O \rightarrow O^+ + O_2$	6.6420E-18	-0.09	1.0	2.4850E-19	-2.4850E-19	Park[75]
		1.8900E-16	-0.52		2.5900E-19	-2.5900E-19	Bird[15]
		4.8490E-12	-1.11		3.8650E-19	-3.8650E-19	Kang[64]

Table A.15: Exothermic chemical reaction rate coefficients (m^3/molecule/s) used in the TCE model. $k_r = aT^b \exp(-E_a/kT)$

Number	Reaction	a	b	$\overline{\zeta}$	E_a (J)	E_{rx} (J)	Reference
50	$O + O + T \rightarrow O_2 + T$	6.3050E-44	-0.50	0.0	0.0000E+01	8.1995E-19	Farbar[6]
		8.3000E-45	-0.50		0.0000E+01	8.1995E-19	Gupta[76]
51	$N + N + T \rightarrow N_2 + T$	5.6910E-40	-1.50	0.0	0.0000E+01	1.5630E-18	Farbar[6]
		3.0060E-44	-0.50		0.0000E+01	1.5630E-18	Gupta[76]
52	$N + O + T \rightarrow NO + T$	1.5830E-43	-0.50	0.0	0.0000E+01	1.0420E-18	Farbar[6]
		2.7850E-40	-1.50		0.0000E+01	1.0420E-18	Gupta[76]
53	$NO + N \rightarrow N_2 + O$	2.4900E-17	0.10	0.0	0.0000E+01	5.1750E-19	Carlson[78]
		2.0200E-17	0.10		0.0000E+01	5.9280E-19	Bird[15]
		4.0600E-12	-1.36		0.0000E+01	5.1750E-19	Boyd[67]
		2.4900E-17	0.00		0.0000E+01	5.1750E-19	Gimelshein[65]
54	$O_2 + N \rightarrow NO + O$	5.2000E-22	1.29	0.0	4.9680E-20	2.2380E-19	Bird[15]
		4.1300E-21	1.18		0.0000E+01	5.5300E-20	Ozawa[9]
		4.6000E-15	-0.55		0.0000E+01	2.2380E-20	Boyd[67]
		1.5980E-18	0.50		4.9680E-20	2.7190E-19	Gimelshein[65]
55	$N_2^+ + e^- \rightarrow N + N$	4.4830E-12	-0.50	0.0	0.0000E+01	9.3400E-19	Park[60]
		8.8800E-10	-1.23		0.0000E+01	9.3400E-19	Bird[15]
		1.0000E-08	-1.43		0.0000E+01	9.3400E-19	Ozawa[7]
		7.2740E-12	-0.65		0.0000E+01	9.3400E-19	Boyd[77]
		1.5700E-17	0.85		0.0000E+01	9.3400E-19	Boyd[67]
		2.4910E-08	-1.50		0.0000E+01	9.3400E-19	Kang[64]
56	$NO^+ + e^- \rightarrow N + O$	1.4940E-11	-0.65	0.0	0.0000E+01	4.4220E-19	Park[60]
		4.0300E-09	-1.63		0.0000E+01	4.4220E-19	Bird[15]
		2.0000E-06	-2.05		0.0000E+01	4.4220E-19	Ozawa[7]
		1.3210E-09	-1.19		0.0000E+01	4.4220E-19	Boyd[77]
		2.2000E-13	-0.19		0.0000E+01	4.4220E-19	Boyd[67]
		1.3280E-08	-1.50		0.0000E+01	4.4220E-19	Kang[64]
		2.9890E-11	-1.00		0.0000E+01	4.4730E-19	Gupta[72]
57	$O_2^+ + e^- \rightarrow O + O$	2.4900E-12	-0.50	0.0	0.0000E+01	1.1200E-18	Park[60]
		3.8300E-09	-1.51		0.0000E+01	1.1200E-18	Bird[15]
		6.0000E-08	-1.60		0.0000E+01	1.1200E-18	Ozawa[7]
		1.4530E-04	-2.41		0.0000E+01	1.1200E-18	Boyd[77]
		9.2200E-15	0.29		0.0000E+01	1.1200E-18	Boyd[67]
		1.3280E-08	-1.50		0.0000E+01	1.1160E-18	Gupta[72]
58	$N_2^+ + N \rightarrow N^+ + N2$	2.3700E-18	-0.52	1.0	0.0000E+01	1.6700E-19	Bird[15]
		2.3430E-14	-0.61		0.0000E+01	1.6700E-19	Boyd[77]
		4.6500E-19	0.50		0.0000E+01	1.6700E-19	Kang[64]
59	$N_2^+ + O \rightarrow O^+ + N_2$	1.7700E-17	-0.21	1.0	0.0000E+01	3.1480E-19	Bird[15]
		1.9780E-18	0.11		0.0000E+01	3.1480E-19	Boyd[77]
		4.1180E-11	-2.20		0.0000E+01	3.1480E-19	Kang[64]
60	$N^+ + O_2 \rightarrow O^+ + NO$	2.4430E-26	2.10	1.0	0.0000E+01	2.1120E-19	Boyd[77]
61	$N_2^+ + O \rightarrow NO^+ + N$	4.1000E-18	0.40	1.0	0.0000E+01	4.9010E-19	Bird[15]

Number	Reaction	a	b	$\overline{\zeta}$	E_a (J)	E_{rx} (J)	Reference
		1.7440E-18	0.30		0.0000E+01	4.9010E-19	Boyd[77]
62	$O^+ + N_2 \rightarrow NO^+ + N$	3.9700E-18	-0.71	1.0	0.0000E+01	1.7670E-19	Boyd[77]
63	$N^+ + O_2 \rightarrow NO^+ + O$	3.0400E-18	0.29	1.0	0.0000E+01	1.0660E-18	Boyd[67]
		1.6610E-16	0.00		0.0000E+01	1.0670E-18	Kang[64]
64	$O_2^+ + N \rightarrow NO^+ + O$	8.9180E-13	-0.97	1.0	0.0000E+01	6.7090E-19	Boyd[77]
65	$O_2^+ + NO \rightarrow NO^+ + O_2$	3.9900E-17	0.41	1.5	0.0000E+01	4.5010E-19	Ozawa[9]
		6.1950E-16	-0.05		0.0000E+01	4.5010E-19	Boyd[77]
		4.4700E-15	-0.17		0.0000E+01	4.5010E-19	Carlson[78]
		2.9890E-17	0.50		0.0000E+01	4.5010E-19	Kang[64]
66	$N^+ + O_2 \rightarrow O_2^+ + N$			1.0			
67	$N_2^+ + O_2 \rightarrow O_2^+ + N_2$	4.5890E-18	-0.04	1.5	0.0000E+01	5.6190E-19	Boyd[77]
68	$O^+ + O_2 \rightarrow O_2^+ + O$	1.8900E-16	-0.52	1.0	0.0000E+01	2.5900E-19	Bird[15]
		4.9930E-18	-0.00		0.0000E+01	2.5900E-19	Boyd[77]
		4.6500E-19	0.50		0.0000E+01	2.5900E-19	Kang[64]
		4.9900E-14	0.00		0.0000E+01	2.5900E-19	Boyd[67]

Table A.16: Coefficients required for the collision volume in Q-K recombination reactions ($V_{coll} = aT^b V_{ref}$).

Number	Reaction	a	b
50	$O + O + O_2 \rightarrow O_2 + O_2$	0.040	-1.30
	$O + O + N_2 \rightarrow O_2 + N_2$	0.070	-1.20
	$O + O + O \rightarrow O_2 + O$	0.080	-1.20
	$O + O + N \rightarrow O_2 + N$	0.090	-1.20
	$O + O + NO \rightarrow O_2 + NO$	0.065	-1.20
	$O + O + O_2^+ \rightarrow O_2 + O_2^+$	0.040	-1.30
	$O + O + N_2^+ \rightarrow O_2 + N_2^+$	0.070	-1.20
	$O + O + O^+ \rightarrow O_2 + O^+$	0.080	-1.20
	$O + O + N^+ \rightarrow O_2 + N^+$	0.090	-1.20
	$O + O + NO^+ \rightarrow O_2 + NO^+$	0.065	-1.20
	$O + O + e^- \rightarrow O_2 + e^-$	0.000	0.00
51	$N + N + O_2 \rightarrow N_2 + O_2$	0.150	-2.05
	$N + N + N_2 \rightarrow N_2 + N_2$	0.090	-2.10
	$N + N + O \rightarrow N_2 + O$	0.160	-2.00
	$N + N + N \rightarrow N_2 + N$	0.170	-2.00
	$N + N + NO \rightarrow N_2 + NO$	0.170	-2.10
	$N + N + O_2^+ \rightarrow N_2 + O_2^+$	0.150	-2.05
	$N + N + N_2^+ \rightarrow N_2 + N_2^+$	0.090	-2.10
	$N + N + O^+ \rightarrow N_2 + O^+$	0.160	-2.00
	$N + N + N^+ \rightarrow N_2 + N^+$	0.170	-2.00
	$N + N + NO^+ \rightarrow N_2 + NO^+$	0.170	-2.10
	N + N + e- → N_2 + e-	0.000	0.00
52	$N + O + O_2 \rightarrow NO + O_2$	0.300	-1.90
	$N + O + N_2 \rightarrow NO + N_2$	0.400	-2.00
	$N + O + O \rightarrow NO + O$	0.300	-1.75
	$N + O + N \rightarrow NO + N$	0.300	-1.75
	$N + O + NO \rightarrow NO + NO$	0.150	-1.90
	$N + O + O_2^+ \rightarrow NO + O_2^+$	0.300	-1.90
	$N + O + N_2^+ \rightarrow NO + N_2^+$	0.400	-2.00
	$N + O + O^+ \rightarrow NO + O^+$	0.300	-1.75
	$N + O + N^+ \rightarrow NO + N^+$	0.300	-1.75

Number	Reaction	*a*	*b*
	$N + O + NO^+ \rightarrow NO + NO^+$	0.150	-1.90
	$N + O + e^- \rightarrow NO + e^-$	0.000	0.00

Table A.17: Coefficients required for the collision volume in Q-K exchange reactions ($E_a = a(T/T_{ref})^b|E_{exch}|$; $E_a = E_a - E_{exch}$ if $E_{exch} < 0.0$).

Number	Reaction	*a*	*b*	E_{exch} (J)
34	$N_2 + O \rightarrow NO + N$	0.150	0.00	-5.2465E-19
35	$NO + O \rightarrow O_2 + N$	0.100	0.68	-2.6785E-19
39	$N^+ + N_2 \rightarrow N_2^+ + N$	0.400	0.10	-1.6844E-19
40	$O^+ + N_2 \rightarrow N_2^+ + O$	0.500	0.20	-3.1479E-19
41	$O^+ + NO \rightarrow N^+ + O_2$	0.100	0.50	-3.6725E-19
42	$NO^+ + N \rightarrow N_2^+ + O$	0.050	0.00	-4.9013E-19
43	$NO^+ + N \rightarrow O^+ + N_2$	0.050	0.70	-1.7672E-19
44	$NO^+ + O \rightarrow N^+ + O_2$	0.000	0.00	-1.0659E-19
45	$NO^+ + O \rightarrow O_2^+ + N$	0.000	0.00	-6.7100E-19
46	$NO^+ + O_2 \rightarrow O_2^+ + NO$	0.000	0.00	-4.5009E-19
47	$O_2^+ + N \rightarrow N^+ + O_2$	0.020	0.10	-3.9487E-19
48	$O_2^+ + N_2 \rightarrow N_2^+ + O_2$	0.050	0.55	-5.6192E-19
49	$O_2^+ + O \rightarrow O^+ + O_2$	0.700	0.15	-2.4852E-19
53	$NO + N \rightarrow N_2 + O$	0.025	0.90	5.2465E-19
54	$O_2 + N \rightarrow NO + O$	0.100	0.48	2.6785E-19
58	$N_2^+ + N \rightarrow N^+ + N_2$	0.400	0.25	1.6844E-19
59	$N_2^+ + O \rightarrow O^+ + N_2$	0.600	0.35	3.1479E-19
60	$N^+ + O_2 \rightarrow O^+ + NO$	0.150	0.40	3.6725E-19
61	$N_2^+ + O \rightarrow NO^+ + N$	0.020	0.80	4.9013E-19
62	$O^+ + N_2 \rightarrow NO^+ + N$	0.000	0.00	1.7672E-19
63	$N^+ + O_2 \rightarrow NO^+ + O$	0.000	0.00	1.0659E-18
64	$O_2^+ + N \rightarrow NO^+ + O$	0.000	0.00	6.7100E-19
65	$O_2^+ + NO \rightarrow NO^+ + O_2$	0.070	0.50	5.4009E-19
66	$N^+ + O_2 \rightarrow O_2^+ + N$	0.000	0.00	3.9487E-19
67	$N_2^+ + O_2 \rightarrow O_2^+ + N_2$	0.200	0.30	5.6192E-19
68	$O^+ + O_2 \rightarrow O_2^+ + O$	0.500	0.10	2.4852E-19

Appendix B: Quantum-Kinetic Electronic Energy Level Transition Rates.

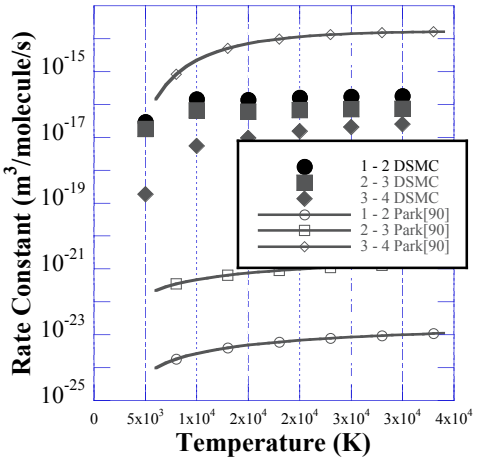

Figure B.1: Transitions for $O_2 + O_2$.

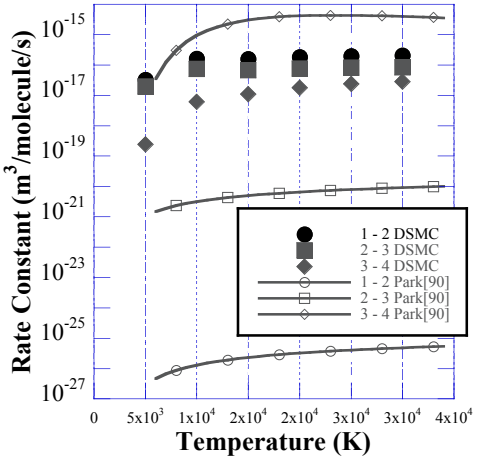

Figure B.2: Transitions for $O_2 + N_2$.

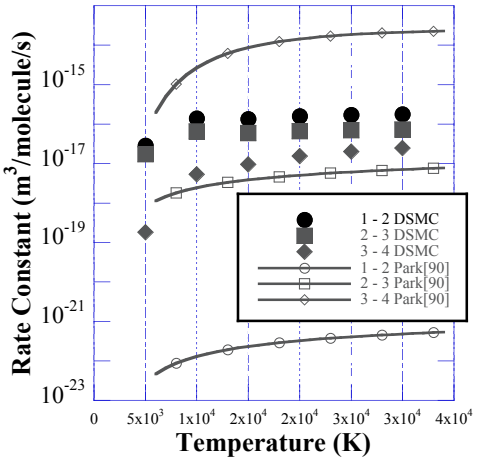

Figure B.3: Transitions for $O_2 + O$.

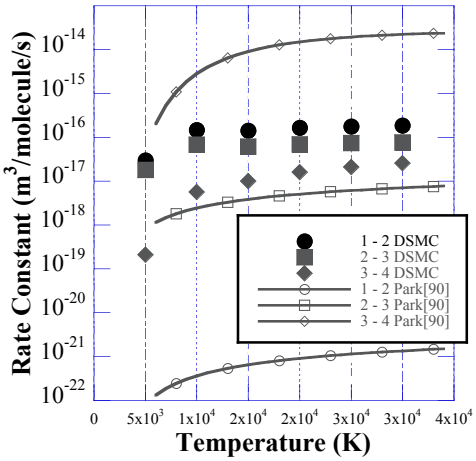

Figure B.4: Transitions for $O_2 + N$.

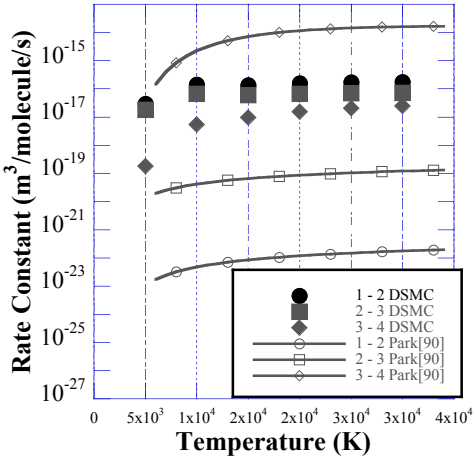

Figure B.5: Transitions for $O_2 + NO$.

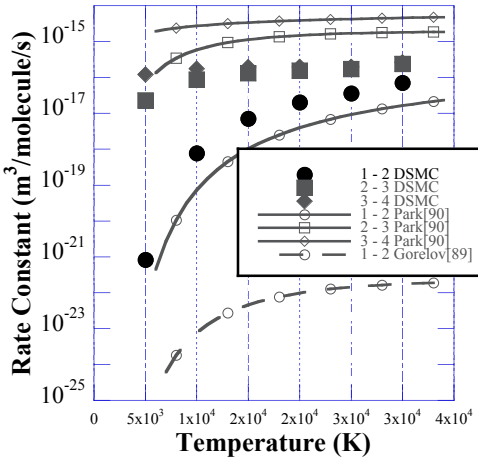

Figure B.6: Transitions for $N_2 + O_2$.

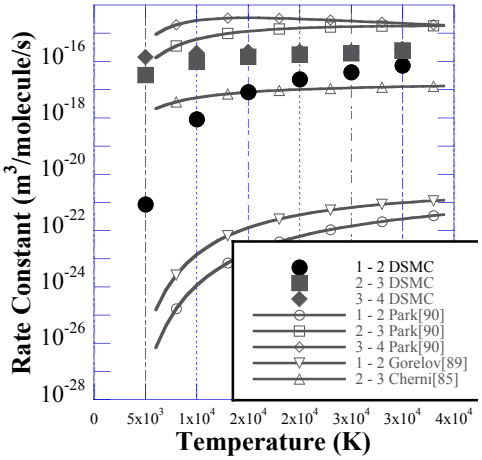

Figure B.7: Transitions for $N_2 + N_2$.

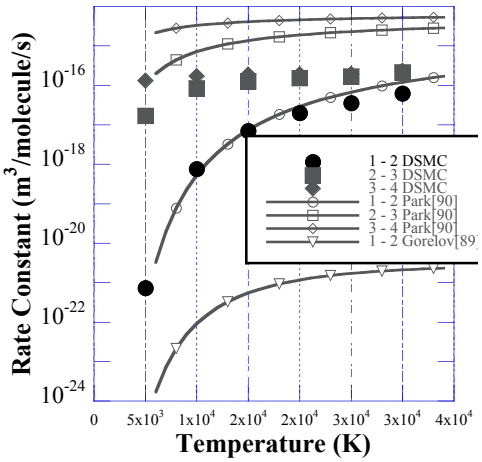

Figure B.8: Transitions for $N_2 + O$.

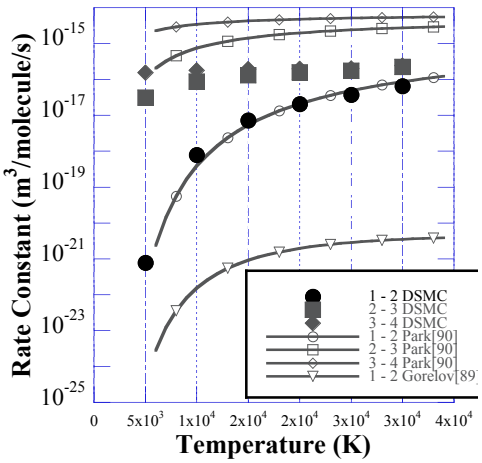

Figure B.9: Transitions for $N_2 + N$.

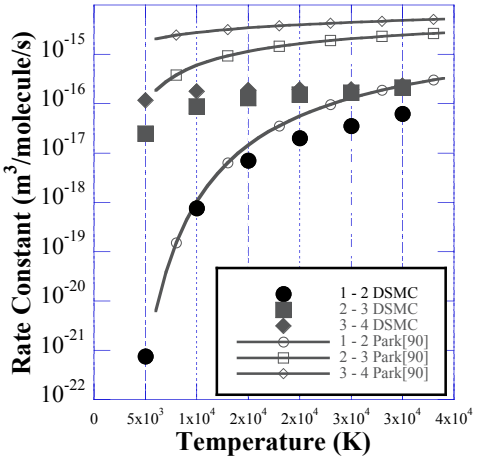

Figure B.10: Transitions for $N_2 + NO$.

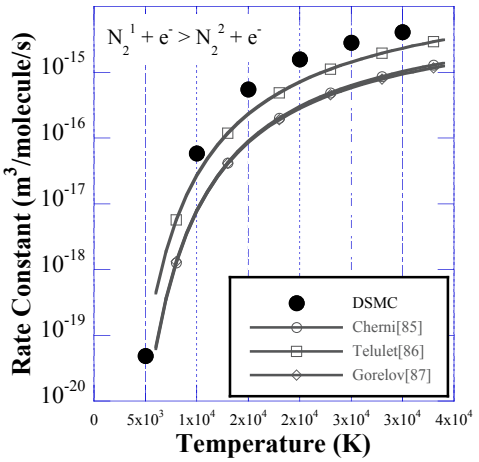

Figure B.11: Transition from level 1-2 for $N_2 + e$.

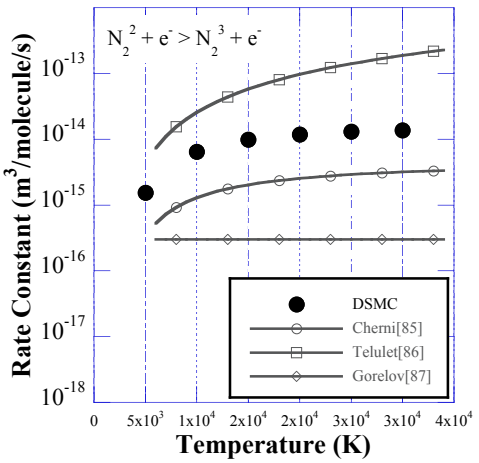

Figure B.12: Transition from level 2-3 for $N_2 + e$.

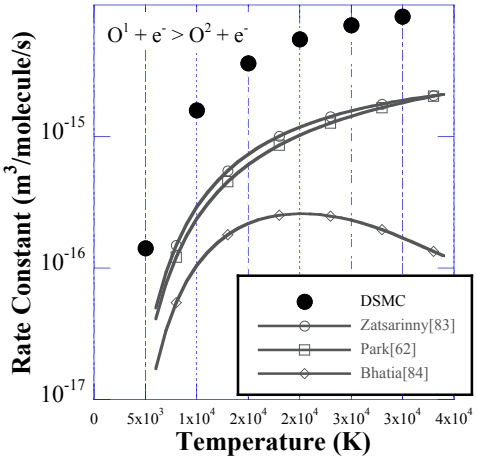

Figure B.13: Transition from level 1-2 for O + e.

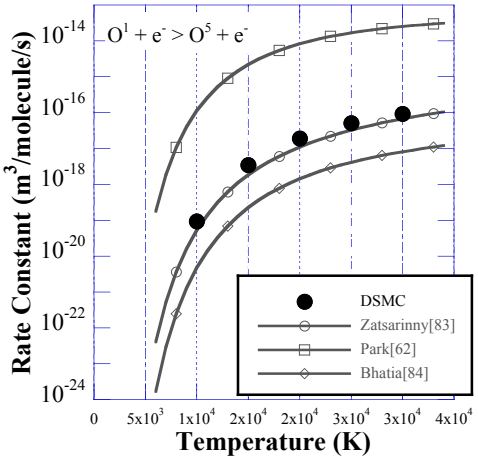

Figure B.16: Transition from level 1-5 for O + e.

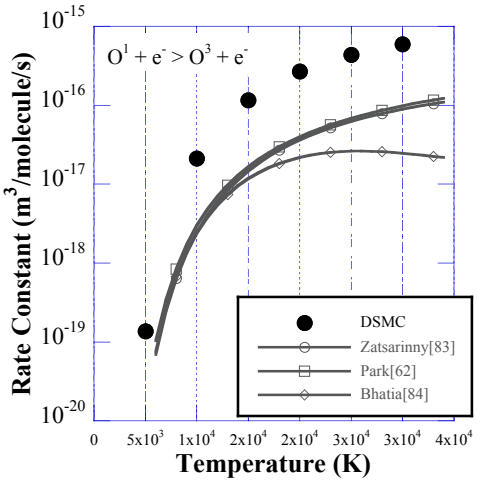

Figure B.14: Transition from level 1-3 for O + e.

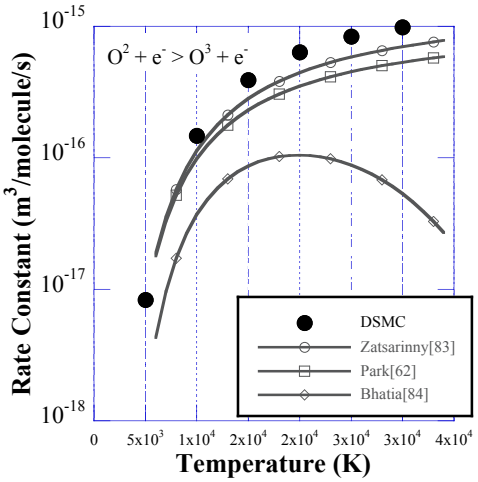

Figure B.17: Transition from level 2-3 for O + e.

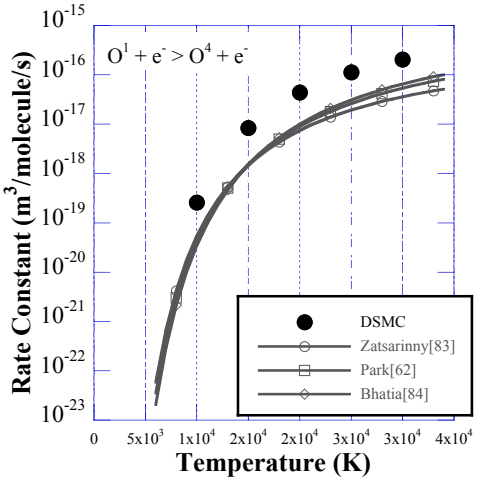

Figure B.15: Transition from level 1-4 for O + e.

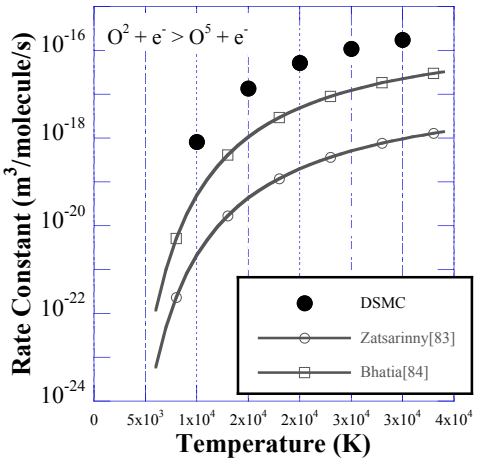

Figure B.18: Transition from level 2-5 for O + e.

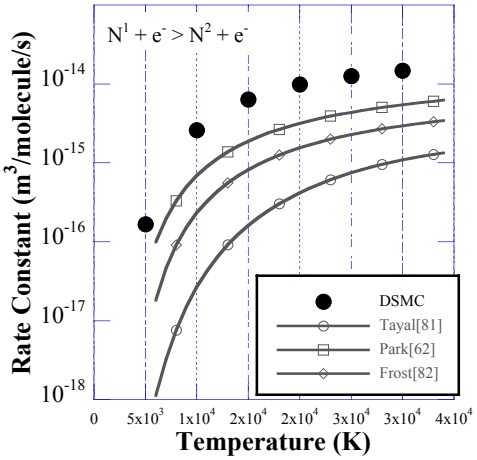

Figure B.19: Transition from level 1-2 for N + e.

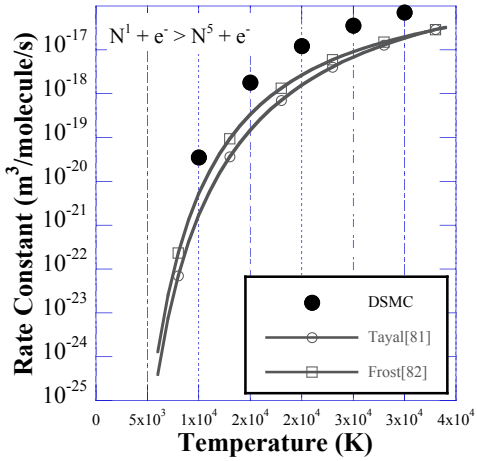

Figure B.22: Transition from level 1-5 for N + e.

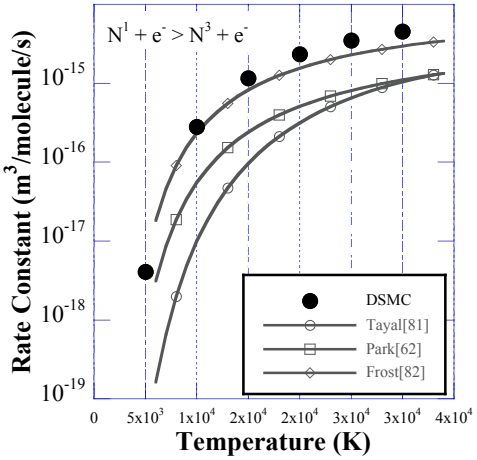

Figure B.20: Transition from level 1-3 for N + e.

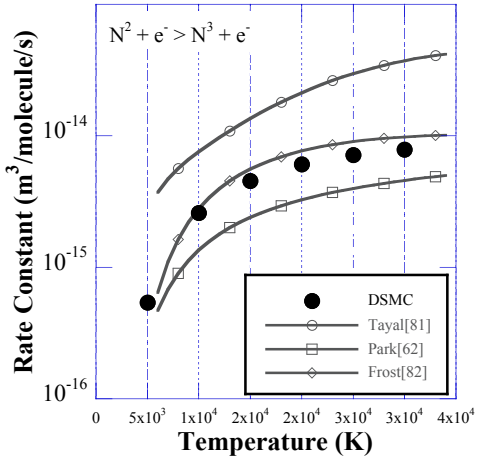

Figure B.23: Transition from level 2-3 for N + e.

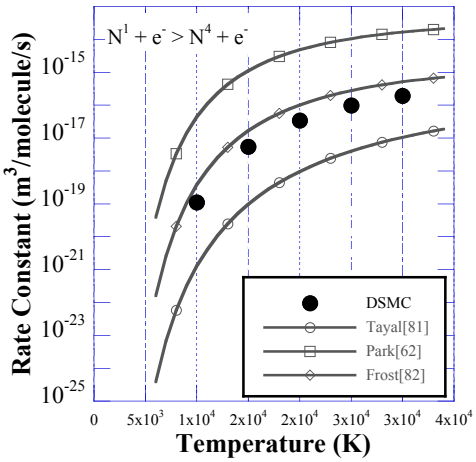

Figure B.21: Transition from level 1-4 for N + e.

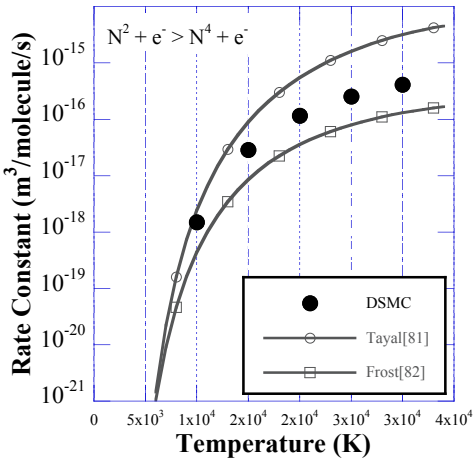

Figure B.24: Transition from level 2-4 for N + e.

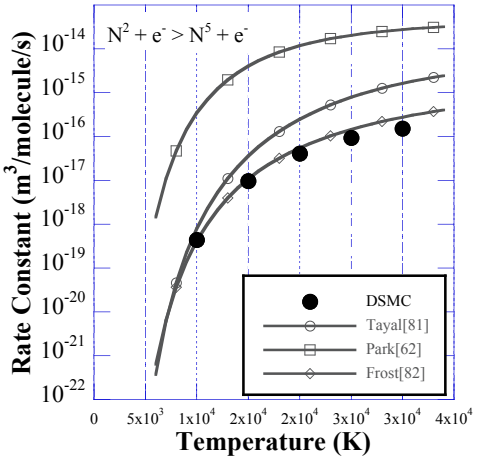

Figure B.25: Transition from level 2-5 for N + e.

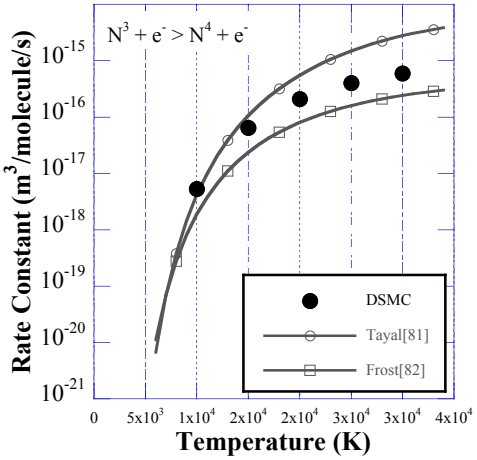

Figure B.26: Transition from level 3-4 for N + e.

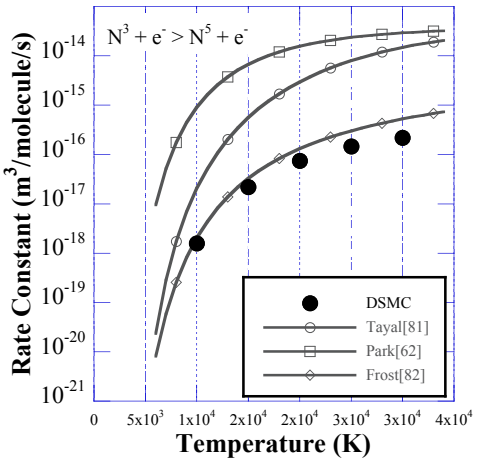

Figure B.27: Transition from level 3-5 for N + e.

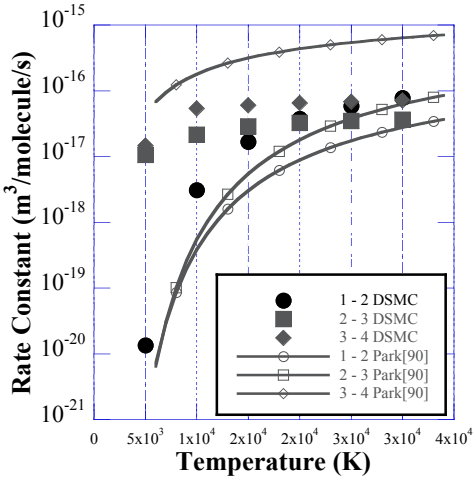

Figure B.28: Transitions for NO + O_2.

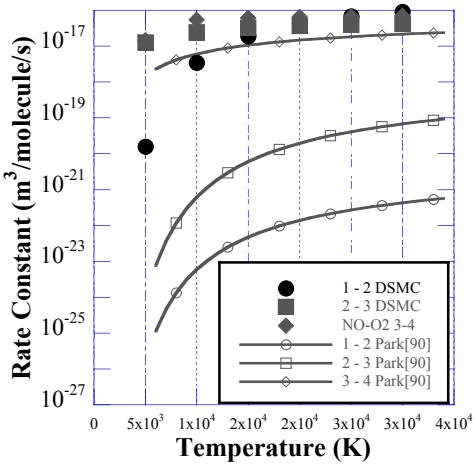

Figure B.29: Transitions for NO + N_2.

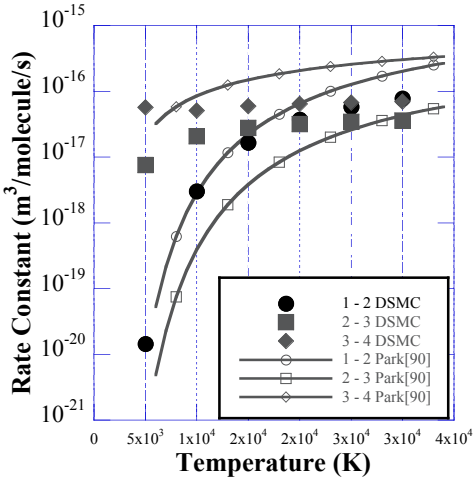

Figure B.30: Transitions for NO + O.

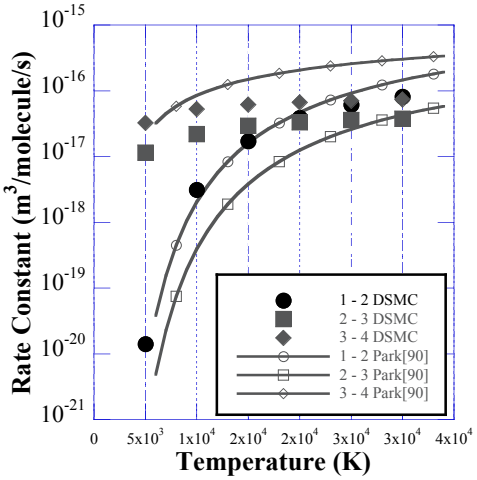

Figure B.31: Transitions for NO + N.

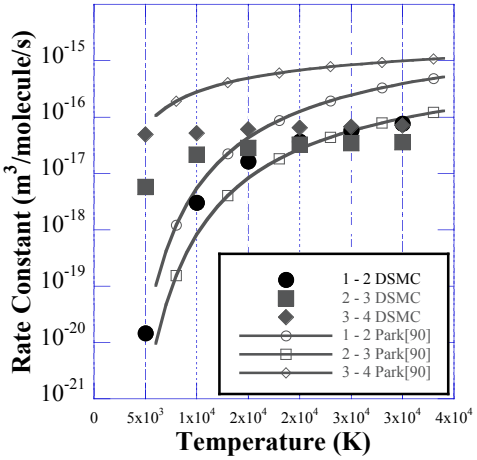

Figure B.32: Transitions for NO + NO.

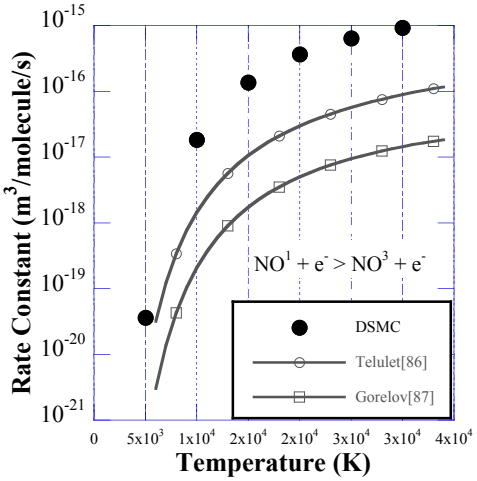

Figure B.33: Transition from level 1-3 for NO + e.

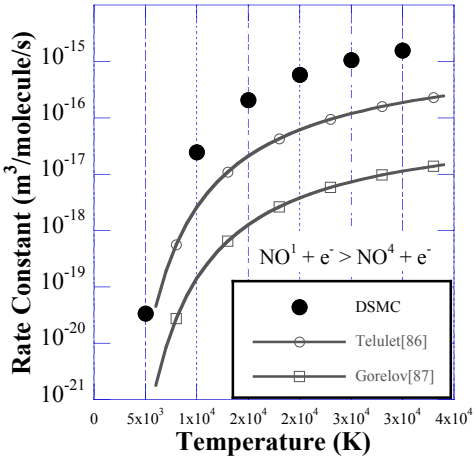

Figure B.34: Transition from level 1-4 for NO + e.

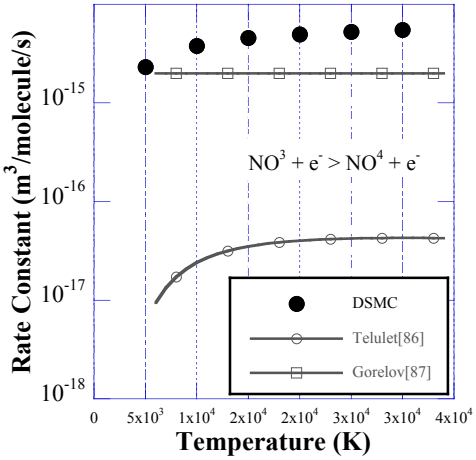

Figure B.35: Transition from level 3-4 for NO + e.

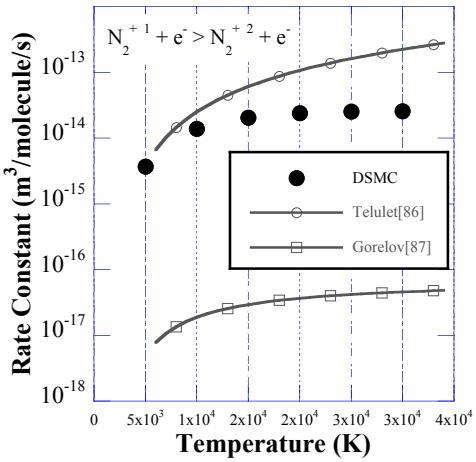

Figure B.36: Transition from level 1-2 for N_2^+ + e.

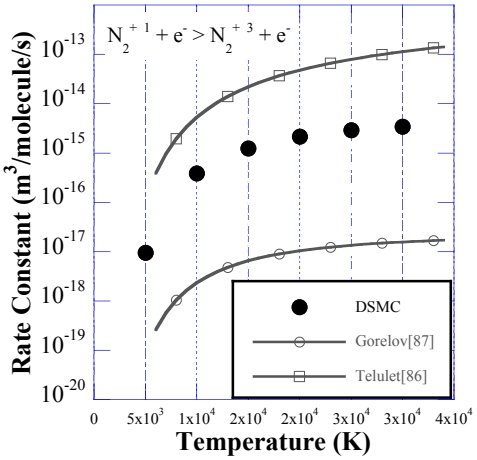

Figure B.37: Transition from level 1-3 for $N_2^+ + e$.

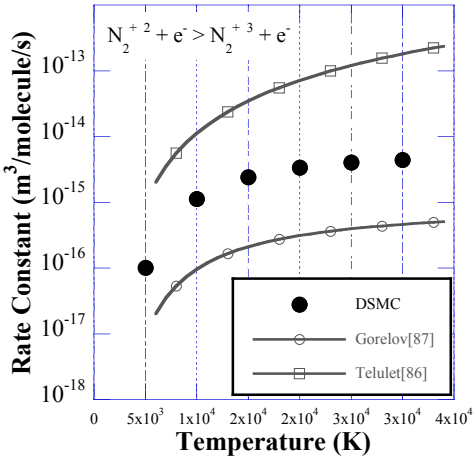

Figure B.38: Transition from level 2-3 for $N_2^+ + e$.

Table B.1: Sampled temperatures and their departure from the set equilibrium temperature.

$T_{equilibrium}$ (K)	10000.00	% Difference	20000.00	% Difference	30000.00	% Difference
T_{tr} (K)	9949.81	-0.502%	19918.00	-0.410%	29901.50	-0.328%
$T_{electron}$ (K)	9953.79	-0.462%	19927.70	-0.361%	29942.00	-0.193%
$T_{el,O2}$ (K)	10000.40	0.004%	20018.80	0.094%	30301.90	1.006%
$T_{el,\ N2}$ (K)	10011.80	0.118%	20017.00	0.085%	30060.00	0.200%
$T_{el,\ O}$ (K)	10019.80	0.198%	19992.40	-0.038%	29967.50	-0.108%
$T_{el,\ N}$ (K)	10009.50	0.095%	19996.20	-0.019%	30040.60	0.135%
$T_{el,\ NO}$ (K)	10011.20	0.112%	20037.70	0.189%	30119.40	0.398%
$T_{el,O2+}$ (K)	10012.50	0.125%	20046.50	0.233%	30140.30	0.468%
$T_{el,\ N2+}$ (K)	10015.70	0.157%	20031.50	0.158%	30106.20	0.354%
$T_{el,\ O+}$ (K)	10011.30	0.113%	19993.80	-0.031%	29923.40	-0.255%
$T_{el,\ N+}$ (K)	10022.70	0.227%	19989.50	-0.053%	29896.20	-0.346%
$T_{el,\ NO+}$ (K)	10011.20	0.112%	20014.50	0.073%	30062.80	0.209%

Table B.2: Sampled and Boltzmann distributions for O_2 at 10,000 K.

Level	Sampled	Boltzmann	% Difference
1	7.7708E-01	7.7719E-01	-0.014%
2	1.6583E-01	1.6585E-01	-0.010%
3	3.8865E-02	3.8807E-02	0.149%
4	2.2448E-03	2.2280E-03	0.754%
5	1.0584E-02	1.0566E-02	0.175%
6	4.8032E-03	4.7751E-03	0.588%
7	5.9326E-04	5.8615E-04	1.212%

Table B.3: Sampled and Boltzmann distributions for O_2 at 20,000 K.

Level	Sampled	Boltzmann	% Difference
1	5.5362E-01	5.5315E-01	0.086%
2	2.0892E-01	2.0863E-01	0.138%
3	7.1264E-02	7.1363E-02	-0.138%
4	1.7149E-02	1.7099E-02	0.292%
5	9.0780E-02	9.1209E-02	-0.470%
6	4.3126E-02	4.3358E-02	-0.535%
7	1.5139E-02	1.5191E-02	-0.342%

Table B.4: Sampled and Boltzmann distributions for O_2 at 30,000 K.

Level	Sampled	Boltzmann	% Difference
1	4.2546E-01	4.2474E-01	0.170%
2	1.9476E-01	1.9370E-01	0.550%
3	7.5215E-02	7.5191E-02	0.032%
4	2.9078E-02	2.9007E-02	0.245%
5	1.6010E-01	1.6091E-01	-0.506%
6	7.7062E-02	7.7793E-02	-0.939%
7	3.8326E-02	3.8662E-02	-0.869%

Table B.5: Sampled and Boltzmann distributions for N_2 at 10,000 K.

Level	Sampled	Boltzmann	% Difference
1	9.9500E-01	9.9505E-01	-0.005%
2	2.1963E-03	2.1776E-03	0.859%
3	1.1353E-03	1.1238E-03	1.026%
4	1.1045E-03	1.0937E-03	0.992%
5	2.1789E-04	2.1573E-04	1.000%
6	5.5589E-05	5.4867E-05	1.316%
7	9.4670E-05	9.3263E-05	1.509%

Table B.6: Sampled and Boltzmann distributions for N_2 at 20,000 K.

Level	Sampled	Boltzmann	% Difference
1	7.3201E-01	7.3248E-01	-0.064%
2	5.9496E-02	5.9350E-02	0.246%
3	6.0508E-02	6.0296E-02	0.352%
4	5.9591E-02	5.9482E-02	0.183%
5	1.8720E-02	1.8681E-02	0.211%
6	5.4476E-03	5.4391E-03	0.156%
7	1.0032E-02	1.0029E-02	0.034%

Table B.7: Sampled and Boltzmann distribution for N_2 at 30,000 K.

Level	Sampled	Boltzmann	% Difference
1	3.6019E-01	3.6023E-01	-0.011%
2	9.7743E-02	9.7283E-02	0.473%
3	1.2460E-01	1.2387E-01	0.592%
4	1.2323E-01	1.2275E-01	0.391%
5	4.5125E-02	4.5014E-02	0.246%
6	1.3711E-02	1.3711E-02	0.001%
7	2.5906E-02	2.5975E-02	-0.265%

Table B.8: Sampled and Boltzmann distributions for O at 10,000 K.

Level	Sampled	Boltzmann	% Difference
1	9.4529E-01	9.4553E-01	-0.025%
2	5.3797E-02	5.3567E-02	0.430%
3	8.1975E-04	8.1264E-04	0.875%
4	1.3074E-05	1.2912E-05	1.258%
5	5.1522E-06	5.0119E-06	2.799%
6	6.0933E-06	6.0882E-06	0.084%
7	2.7848E-06	2.7387E-06	1.682%

Table B.9: Sampled and Boltzmann distributions for O at 20,000 K.

Level	Sampled	Boltzmann	% Difference
1	7.4519E-01	7.4541E-01	-0.029%
2	1.3215E-01	1.3224E-01	-0.070%
3	7.2810E-03	7.2842E-03	-0.044%
4	2.0615E-03	2.0531E-03	0.409%
5	9.9362E-04	9.9083E-04	0.282%
6	2.4553E-03	2.4419E-03	0.550%
7	1.2762E-03	1.2686E-03	0.597%

Table B.10: Sampled and Boltzmann distributions for O at 30,000 K.

Level	Sampled	Boltzmann	% Difference
1	3.0872E-01	3.0795E-01	0.250%
2	8.0065E-02	7.9930E-02	0.170%
3	6.7504E-03	6.7670E-03	-0.245%
4	4.9942E-03	4.9743E-03	0.399%
5	2.5918E-03	2.5813E-03	0.406%
6	8.1065E-03	8.0535E-03	0.658%
7	4.4226E-03	4.3898E-03	0.748%

Table B.11: Sampled and Boltzmann distributions for N at 10,000 K.

Level	Sampled	Boltzmann	% Difference
1	8.4636E-01	8.4671E-01	-0.042%
2	1.3341E-01	1.3311E-01	0.225%
3	2.0090E-02	2.0036E-02	0.271%
4	1.5808E-05	1.5762E-05	0.292%
5	5.2667E-06	5.2246E-06	0.807%
6	7.9995E-06	7.9046E-06	1.201%
7	6.2563E-07	6.0151E-07	4.011%

Table B.12: Sampled and Boltzmann distributions for N at 20,000 K.

Level	Sampled	Boltzmann	% Difference
1	4.3952E-01	4.3890E-01	0.141%
2	2.7547E-01	2.7515E-01	0.116%
3	8.2188E-02	8.2688E-02	-0.605%
4	3.2850E-03	3.2799E-03	0.155%
5	1.3379E-03	1.3353E-03	0.198%
6	2.3279E-03	2.3227E-03	0.223%
7	2.6346E-04	2.6158E-04	0.719%

Table B.13: Sampled and Boltzmann distributions for N at 30,000 K.

Level	Sampled	Boltzmann	% Difference
1	1.0682E-01	1.0620E-01	0.580%
2	1.0632E-01	1.0558E-01	0.697%
3	3.9934E-02	3.9954E-02	-0.051%
4	5.8929E-03	5.8551E-03	0.646%
5	2.5708E-03	2.5524E-03	0.722%
6	4.6881E-03	4.6517E-03	0.783%
7	6.0134E-04	5.9704E-04	0.720%

Table B.14: Sampled and Boltzmann distributions for NO at 10,000 K.

Level	Sampled	Boltzmann	% Difference
1	9.8591E-01	9.8601E-01	-0.010%
2	8.3771E-03	8.3267E-03	0.605%
3	8.9642E-04	8.8993E-04	0.730%
4	1.3534E-03	1.3421E-03	0.843%
5	9.9780E-04	9.8763E-04	1.030%
6	8.6417E-04	8.5528E-04	1.040%
7	5.5615E-04	5.5025E-04	1.073%

Table B.15: Sampled and Boltzmann distributions for NO at 20,000 K.

Level	Sampled	Boltzmann	% Difference
1	7.3783E-01	7.3899E-01	-0.157%
2	9.6384E-02	9.6040E-02	0.359%
3	1.5806E-02	1.5699E-02	0.684%
4	2.7450E-02	2.7264E-02	0.683%
5	2.3546E-02	2.3388E-02	0.675%
6	2.1886E-02	2.1765E-02	0.557%
7	1.7534E-02	1.7457E-02	0.439%

Table B.16: Sampled and Boltzmann distributions for NO at 30,000 K.

Level	Sampled	Boltzmann	% Difference
1	4.7041E-01	4.7202E-01	-0.342%
2	1.5317E-01	1.5259E-01	0.383%
3	2.9009E-02	2.8737E-02	0.948%
4	5.2855E-02	5.2311E-02	1.040%
5	4.7618E-02	4.7228E-02	0.826%
6	4.5222E-02	4.5016E-02	0.457%
7	3.8913E-02	3.8862E-02	0.132%

Table B.17: Sampled and Boltzmann distributions for O_2^+ at 10,000 K.

Level	Sampled	Boltzmann	% Difference
1	9.7135E-01	9.7155E-01	-0.020%
2	1.7156E-02	1.7058E-02	0.577%
3	2.8567E-03	2.8334E-03	0.821%
4	4.2667E-03	4.2331E-03	0.795%
5	1.9302E-03	1.9136E-03	0.867%
6	5.8441E-04	5.7826E-04	1.063%
7	7.9150E-04	7.8423E-04	0.927%

Table B.18: Sampled and Boltzmann distributions for O_2^+ at 20,000 K.

Level	Sampled	Boltzmann	% Difference
1	6.6647E-01	6.6768E-01	-0.181%
2	1.2558E-01	1.2512E-01	0.372%
3	3.6258E-02	3.6057E-02	0.557%
4	5.4176E-02	5.3977E-02	0.369%
5	2.9739E-02	2.9632E-02	0.361%
6	1.1570E-02	1.1518E-02	0.451%
7	1.9025E-02	1.8970E-02	0.293%

Table B.19: Sampled and Boltzmann distributions for O_2^+ at 30,000 K.

Level	Sampled	Boltzmann	% Difference
1	4.1158E-01	4.1287E-01	-0.313%
2	1.7107E-01	1.7034E-01	0.427%
3	5.9420E-02	5.8989E-02	0.731%
4	8.8882E-02	8.8364E-02	0.586%
5	5.1954E-02	5.1754E-02	0.386%
6	2.1926E-02	2.1879E-02	0.217%
7	3.8413E-02	3.8443E-02	-0.077%

Table B.20: Sampled and Boltzmann distributions for N_2^+ at 10,000 K.

Level	Sampled	Boltzmann	% Difference
1	6.1227E-01	6.1286E-01	-0.096%
2	3.2813E-01	3.2776E-01	0.113%
3	1.5790E-02	1.5718E-02	0.457%
4	3.1316E-02	3.1262E-02	0.173%
5	6.2032E-03	6.1665E-03	0.596%
6	3.2954E-03	3.2741E-03	0.649%
7	6.1995E-04	6.1403E-04	0.964%

Table B.21: Sampled and Boltzmann distributions for N_2^+ at 20,000 K.

Level	Sampled	Boltzmann	% Difference
1	3.1457E-01	3.1438E-01	0.059%
2	3.2567E-01	3.2514E-01	0.163%
3	5.0346E-02	5.0348E-02	-0.003%
4	1.0017E-01	1.0042E-01	-0.245%
5	6.3131E-02	6.3071E-02	0.096%
6	4.5969E-02	4.5958E-02	0.025%
7	1.4075E-02	1.4073E-02	0.014%

Table B.22: Sampled and Boltzmann distributions for N_2^+ at 30,000 K.

Level	Sampled	Boltzmann	% Difference
1	1.8259E-01	1.8224E-01	0.195%
2	2.3563E-01	2.3481E-01	0.349%
3	5.3865E-02	5.3742E-02	0.229%
4	1.0748E-01	1.0728E-01	0.183%
5	9.9579E-02	9.9136E-02	0.447%
6	8.0402E-02	8.0276E-02	0.157%
7	2.8918E-02	2.8946E-02	-0.098%

Table B.23: Sampled and Boltzmann distributions for O^+ at 10,000 K.

Level	Sampled	Boltzmann	% Difference
1	9.4566E-01	9.4590E-01	-0.025%
2	5.0110E-02	4.9904E-02	0.414%
3	4.2276E-03	4.2007E-03	0.641%

Table B.24: Sampled and Boltzmann distributions for O^+ at 20,000 K.

Level	Sampled	Boltzmann	% Difference
1	6.9240E-01	6.9214E-01	0.037%
2	2.5131E-01	2.5137E-01	-0.023%
3	5.6287E-02	5.6491E-02	-0.361%

Table B.25: Sampled and Boltzmann distributions for O^+ at 30,000 K.

Level	Sampled	Boltzmann	% Difference
1	5.2579E-01	5.2459E-01	0.229%
2	3.6206E-01	3.6242E-01	-0.099%
3	1.1216E-01	1.1299E-01	-0.735%

Table B.26: Sampled and Boltzmann distributions for N^+ at 10,000 K.

Level	Sampled	Boltzmann	% Difference
1	9.4103E-01	9.4131E-01	-0.030%
2	5.8007E-02	5.7735E-02	0.471%
3	9.5709E-04	9.4864E-04	0.891%
4	2.7276E-06	2.7013E-06	0.974%
5	1.3391E-07	1.4098E-07	-5.016%
6	0.0000E+01	5.1142E-10	-100.000%
7	9.9063E-10	6.0919E-10	62.615%

Table B.27: Sampled and Boltzmann distributions for N^+ at 20,000 K.

Level	Sampled	Boltzmann	% Difference
1	8.3493E-01	8.3487E-01	0.008%
2	1.5404E-01	1.5411E-01	-0.046%
3	8.8414E-03	8.8344E-03	0.079%
4	1.8248E-03	1.8258E-03	-0.056%
5	3.2492E-04	3.2310E-04	0.565%
6	1.4622E-05	1.4505E-05	0.810%
7	2.4824E-05	2.4524E-05	1.222%

Table B.28: Sampled and Boltzmann distributions for N^+ at 30,000 K.

Level	Sampled	Boltzmann	% Difference
1	7.6006E-01	7.5955E-01	0.067%
2	2.0205E-01	2.0243E-01	-0.188%
3	1.7556E-02	1.7600E-02	-0.251%
4	1.5094E-02	1.5173E-02	-0.519%
5	4.0278E-03	4.0337E-03	-0.145%
6	4.1872E-04	4.1885E-04	-0.031%
7	7.9535E-04	7.9589E-04	-0.068%

Table B.29: Sampled and Boltzmann distributions for NO^+ at 10,000 K.

Level	Sampled	Boltzmann	% Difference
1	9.9599E-01	9.9603E-01	-0.004%
2	1.6518E-03	1.6379E-03	0.849%
3	1.1971E-03	1.1854E-03	0.988%
4	8.2190E-04	8.1217E-04	1.198%
5	1.7649E-04	1.7472E-04	1.015%
6	4.5549E-05	4.4971E-05	1.285%
7	6.9164E-05	6.8332E-05	1.218%

Table B.30: Sampled and Boltzmann distributions for NO^+ at 20,000 K.

Level	Sampled	Boltzmann	% Difference
1	7.8349E-01	7.8358E-01	-0.012%
2	5.5182E-02	5.5037E-02	0.263%
3	6.6323E-02	6.6215E-02	0.163%
4	5.4691E-02	5.4809E-02	-0.215%
5	1.7924E-02	1.7975E-02	-0.286%
6	5.2648E-03	5.2652E-03	-0.008%
7	9.1870E-03	9.1786E-03	0.091%

Table B.31: Sampled and Boltzmann distributions for NO^+ at 30,000 K.

Level	Sampled	Boltzmann	% Difference
1	4.5955E-01	4.5873E-01	0.178%
2	1.1342E-01	1.1263E-01	0.703%
3	1.6075E-01	1.6052E-01	0.145%
4	1.4048E-01	1.4151E-01	-0.728%
5	5.2954E-02	5.3415E-02	-0.862%
6	1.6242E-02	1.6335E-02	-0.568%
7	2.9677E-02	2.9810E-02	-0.446%

Appendix C: Quantum-Kinetic Reaction Rates.

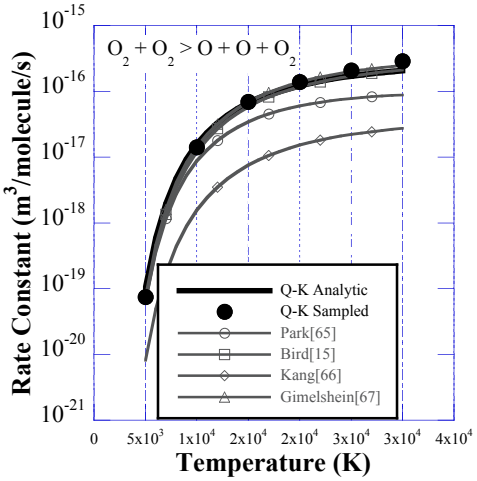

Figure C.1: Q-K reaction rates for reaction 1.

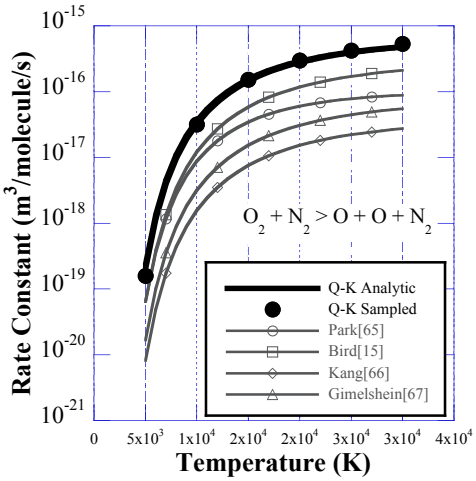

Figure C.2: Q-K reaction rates for reaction 2.

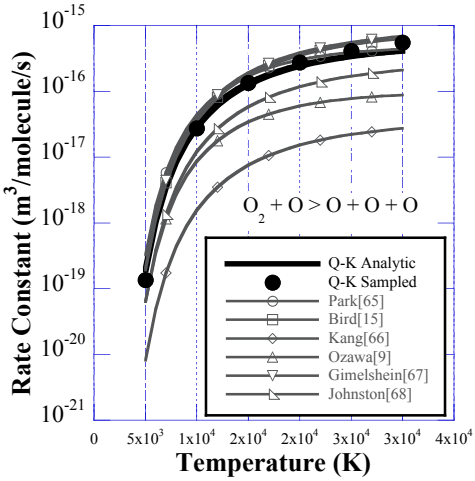

Figure C.3: Q-K reaction rates for reaction 3.

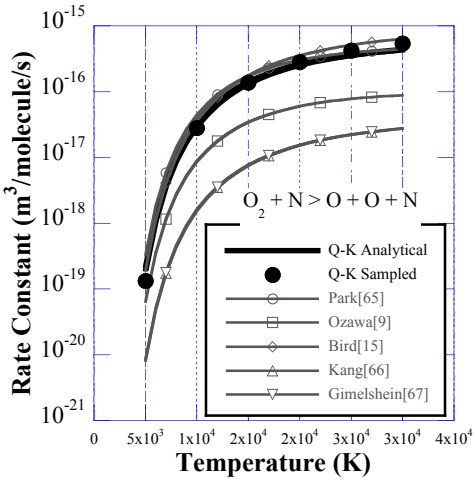

Figure C.4: Q-K reaction rates for reaction 4.

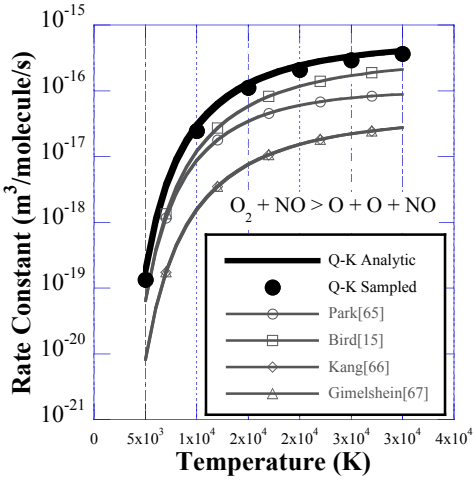

Figure C.5: Q-K reaction rates for reaction 5.

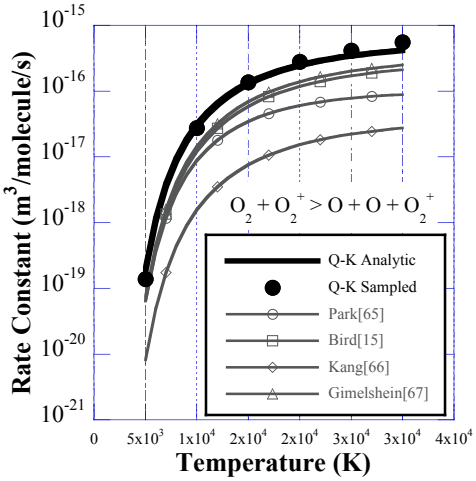

Figure C.6: Q-K reaction rates for reaction 6.

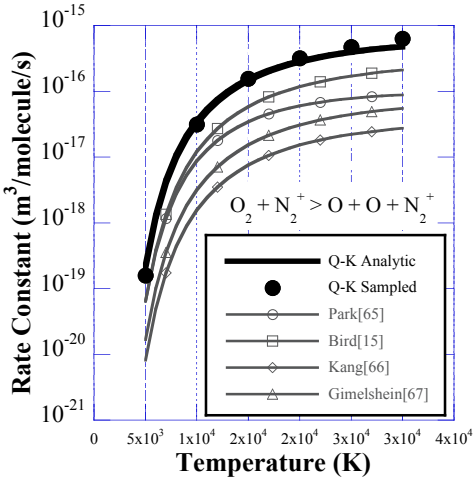

Figure C.7: Q-K reaction rates for reaction 7.

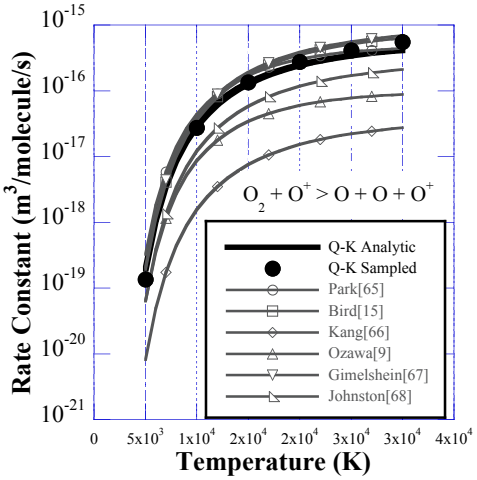

Figure C.8: Q-K reaction rates for reaction 8.

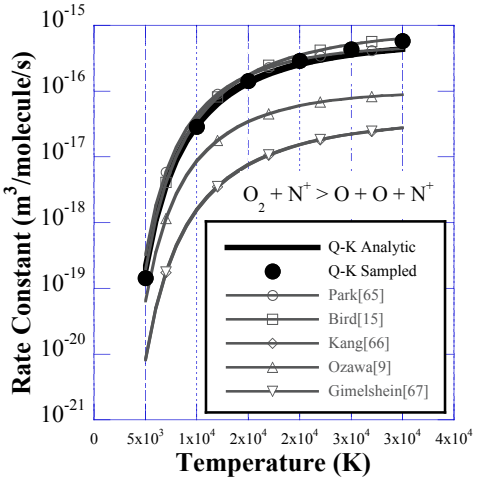

Figure C.9: Q-K reaction rates for reaction 9.

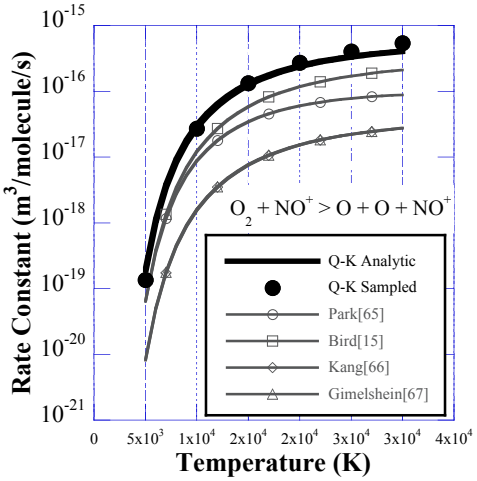

Figure C.10: Q-K reaction rates for reaction 10.

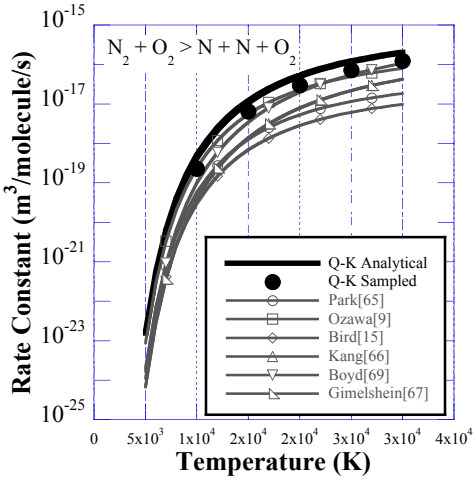

Figure C.11: Q-K reaction rates for reaction 11.

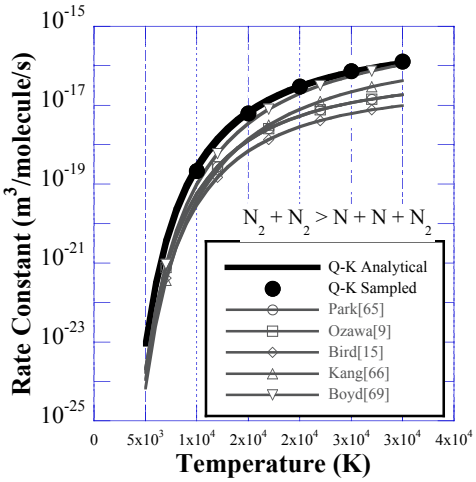

Figure C.12: Q-K reaction rates for reaction 12.

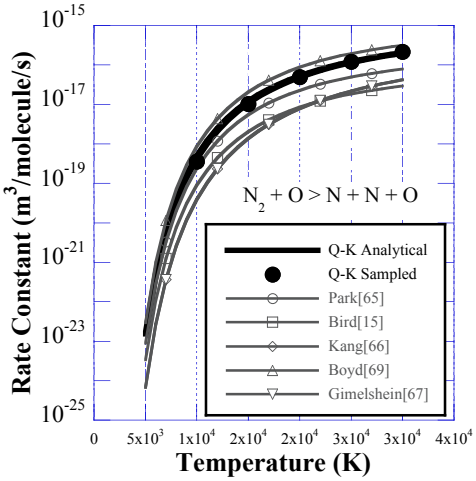

Figure C.13: Q-K reaction rates for reaction 13.

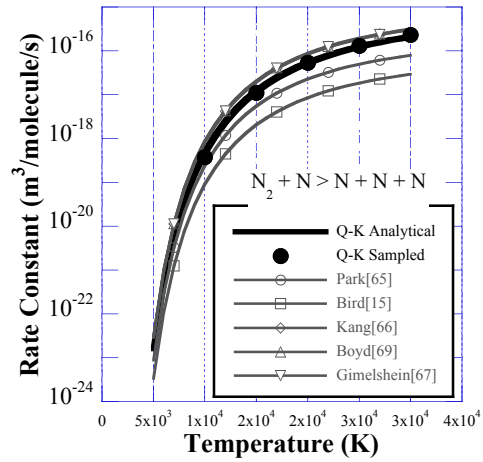

Figure C.14: Q-K reaction rates for reaction 14.

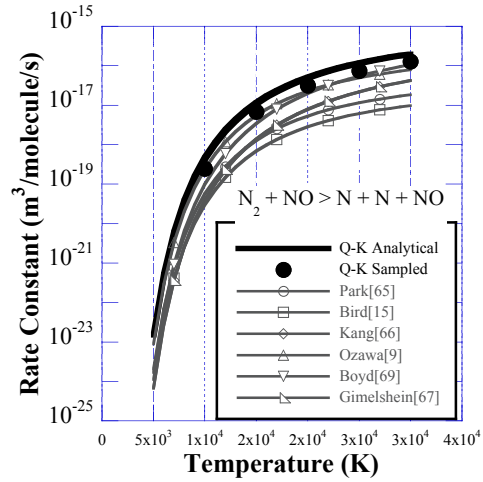

Figure C.15: Q-K reaction rates for reaction 15.

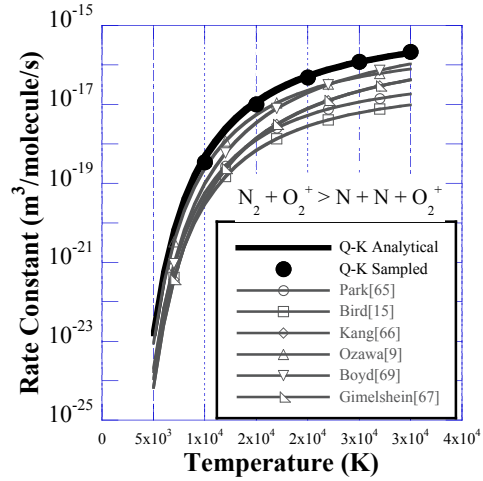

Figure C.16: Q-K reaction rates for reaction 16.

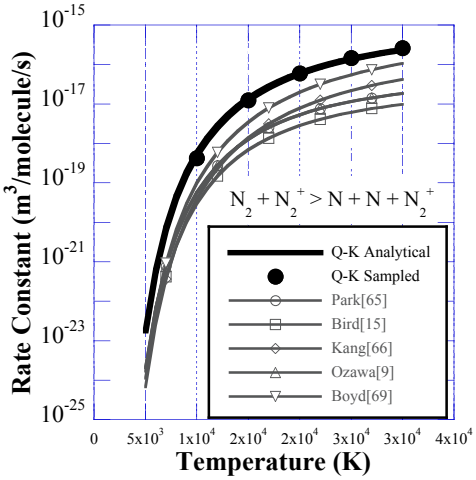

Figure C.17: Q-K reaction rates for reaction 17.

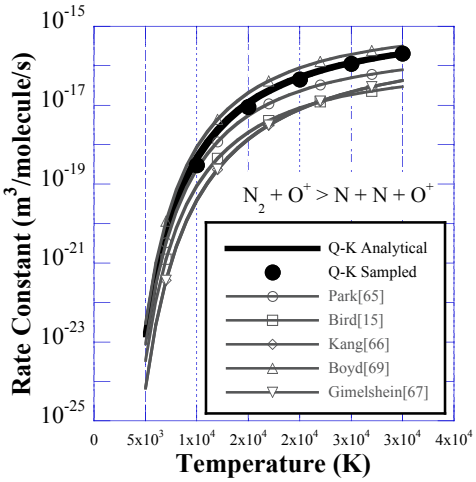

Figure C.18: Q-K reaction rates for reaction 18.

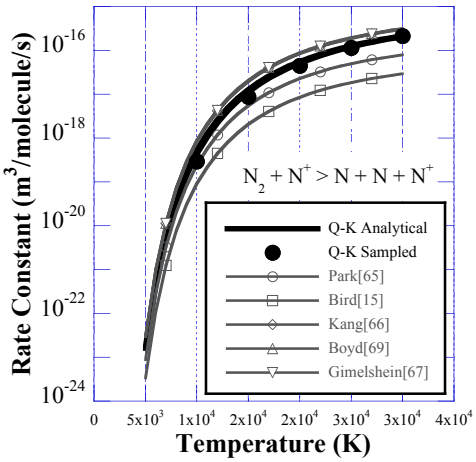

Figure C.19: Q-K reaction rates for reaction 19.

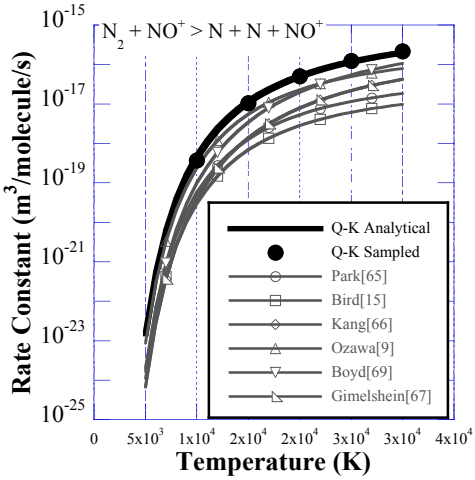

Figure C.20: Q-K reaction rates for reaction 20.

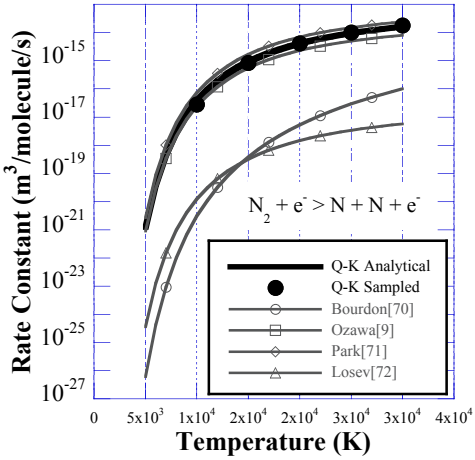

Figure C.21: Q-K reaction rates for reaction 21.

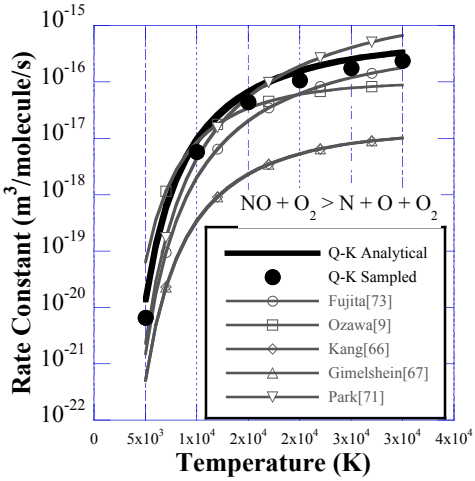

Figure C.22: Q-K reaction rates for reaction 22.

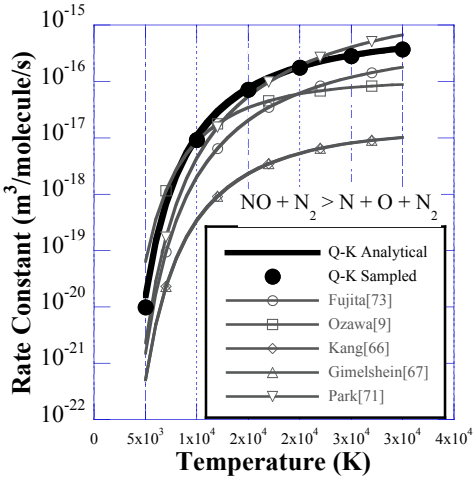

Figure C.23: Q-K reaction rates for reaction 23.

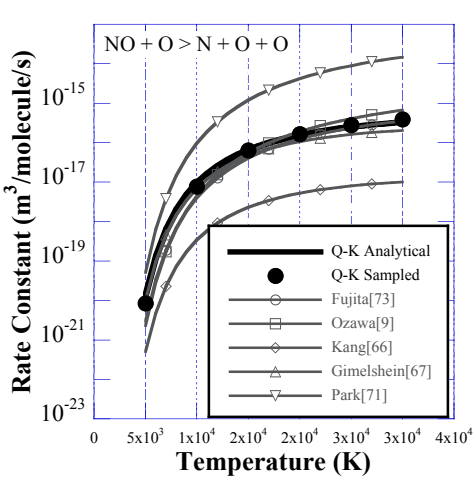

Figure C.24: Q-K reaction rates for reaction 24.

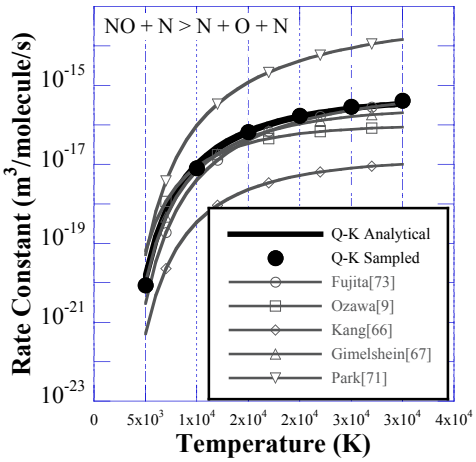

Figure C.25: Q-K reaction rates for reaction 25.

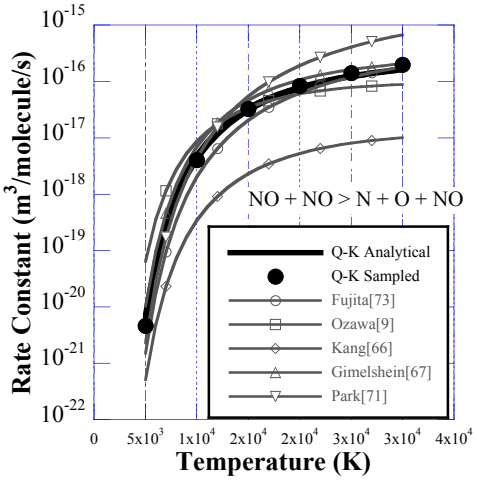

Figure C.26: Q-K reaction rates for reaction 26.

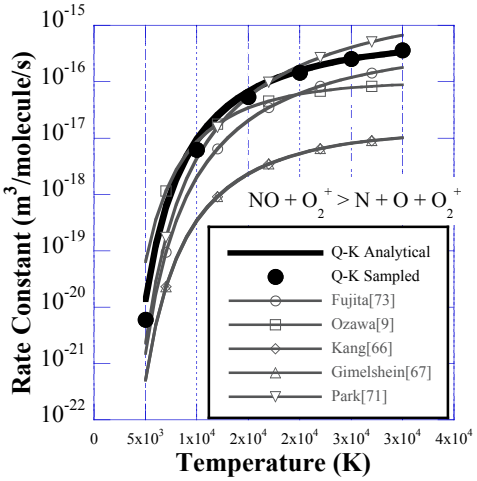

Figure C.27: Q-K reaction rates for reaction 27.

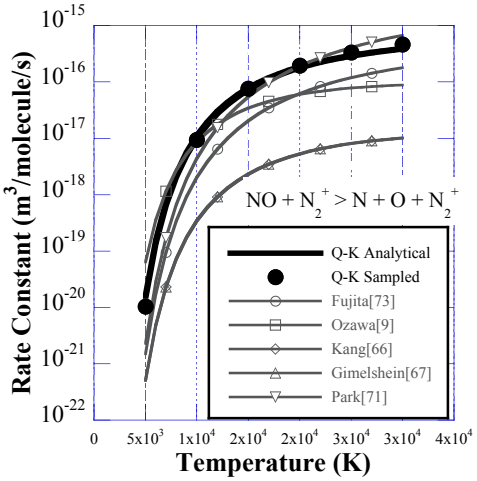

Figure C.28: Q-K reaction rates for reaction 28.

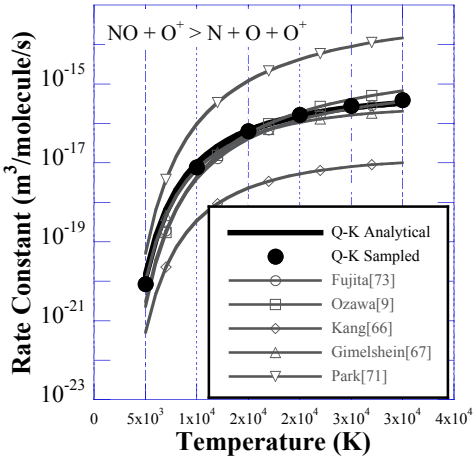

Figure C.29: Q-K reaction rates for reaction 29.

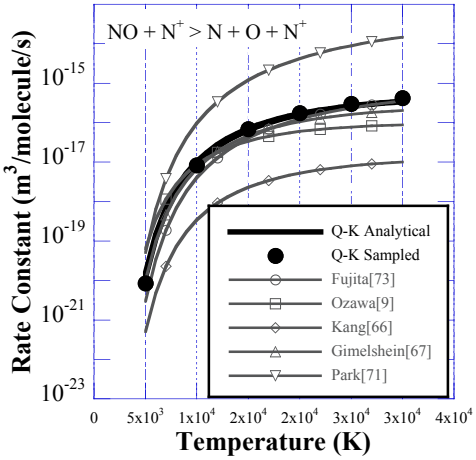

Figure C.30: Q-K reaction rates for reaction 30.

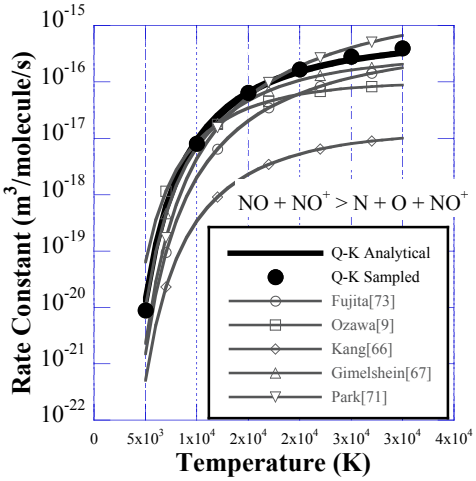

Figure C.31: Q-K reaction rates for reaction 31.

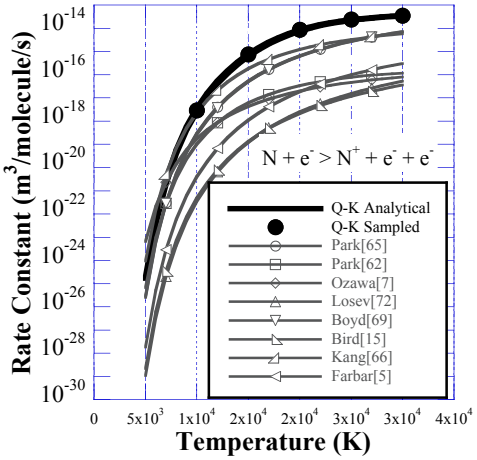

Figure C.32: Q-K reaction rates for reaction 32.

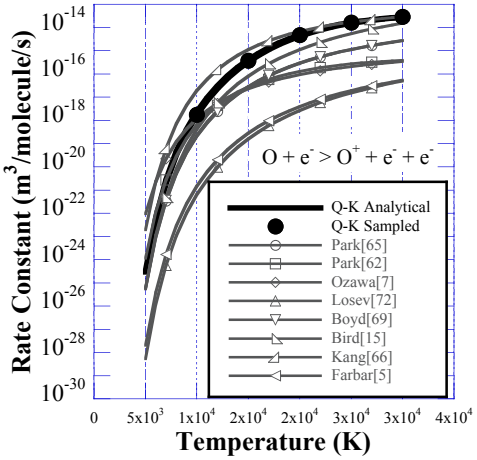

Figure C.33: Q-K reaction rates for reaction 33.

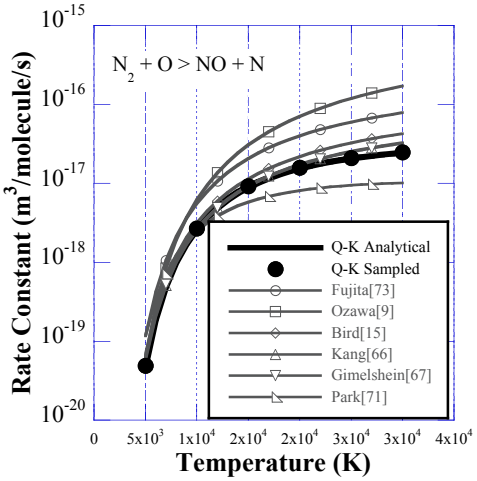

Figure C.34: Q-K reaction rates for reaction 34.

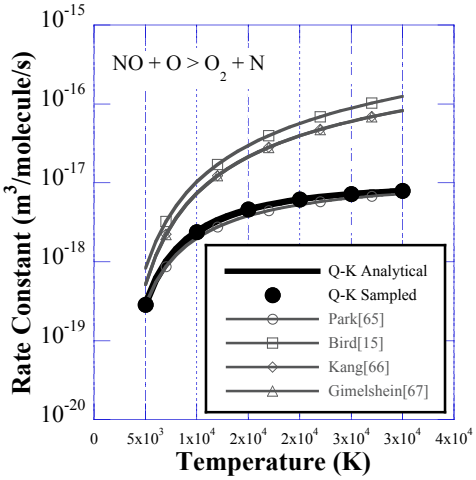

Figure C.35: Q-K reaction rates for reaction 35.

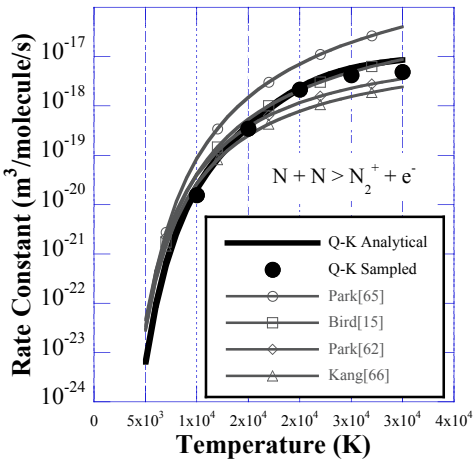

Figure C.36: Q-K reaction rates for reaction 36.

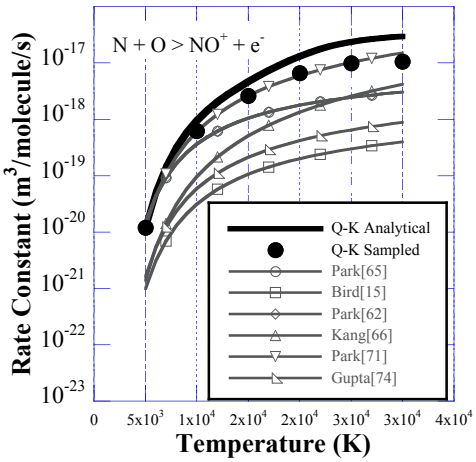

Figure C.37: Q-K reaction rates for reaction 37.

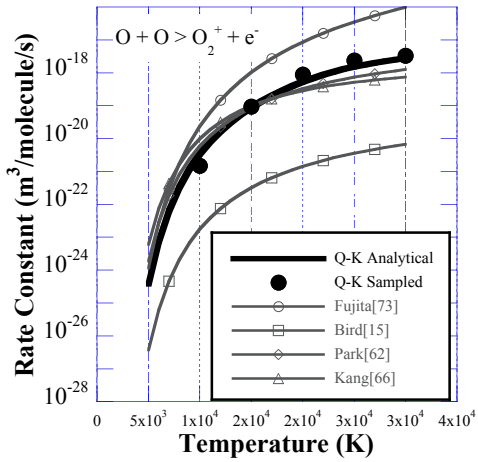

Figure C.38: Q-K reaction rates for reaction 38.

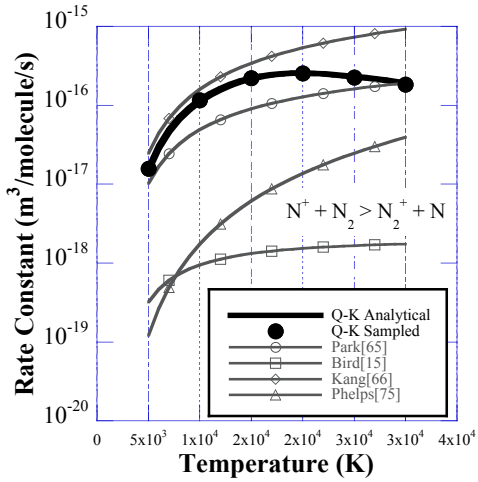

Figure C.39: Q-K reaction rates for reaction 39.

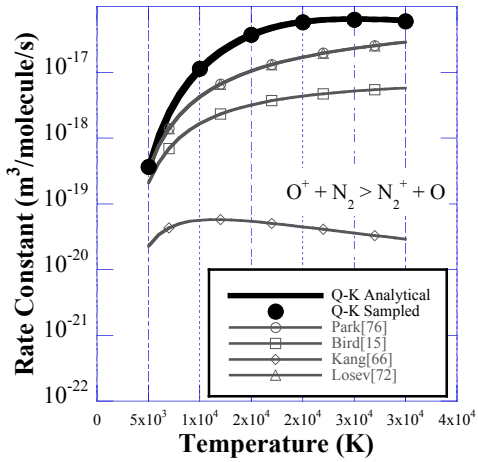

Figure C.40: Q-K reaction rates for reaction 40.

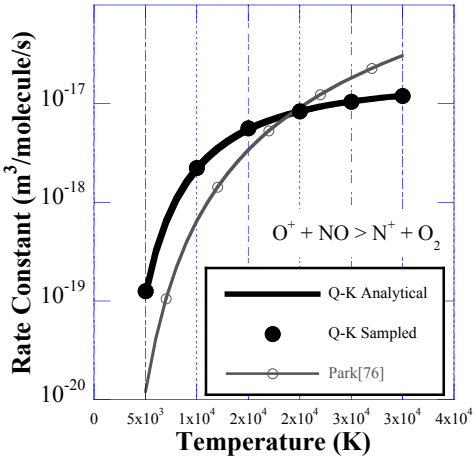

Figure C.41: Q-K reaction rates for reaction 41.

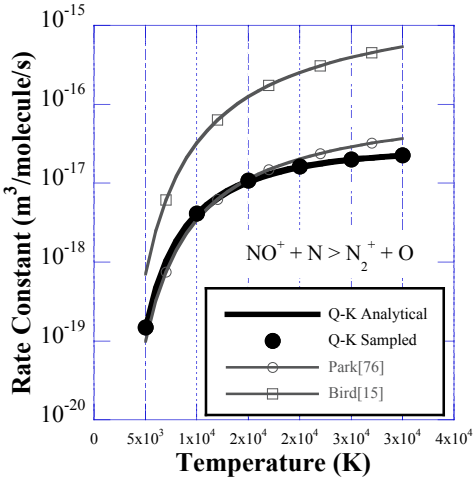

Figure C.42: Q-K reaction rates for reaction 42.

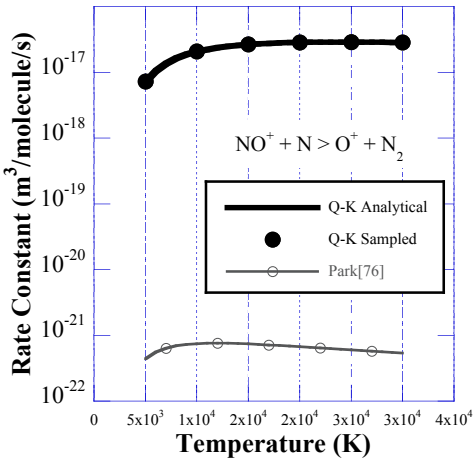

Figure C.43: Q-K reaction rates for reaction 43.

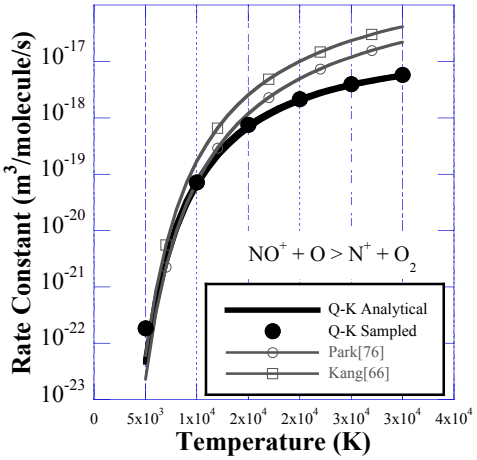

Figure C.44: Q-K reaction rates for reaction 44.

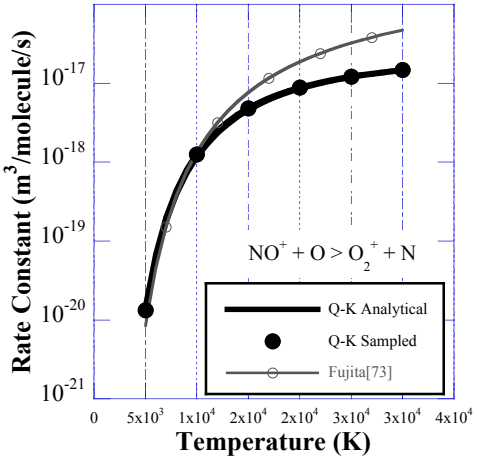

Figure C.45: Q-K reaction rates for reaction 45.

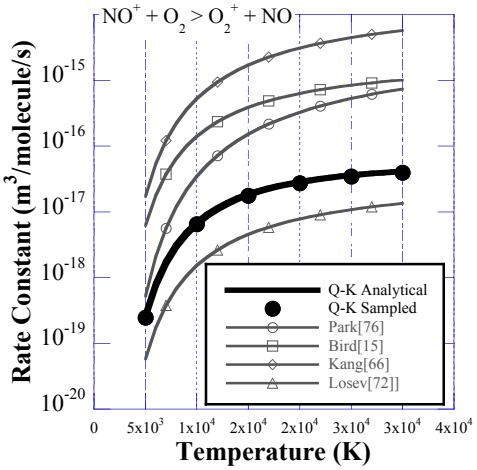

Figure C.46: Q-K reaction rates for reaction 46.

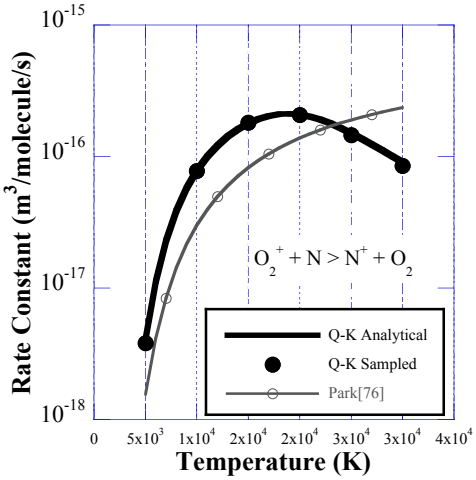

Figure C.47: Q-K reaction rates for reaction 47.

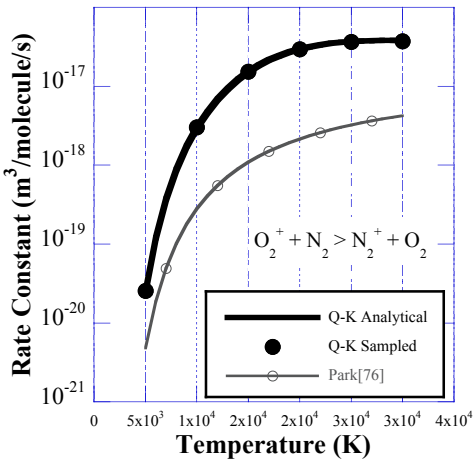

Figure C.48: Q-K reaction rates for reaction 48.

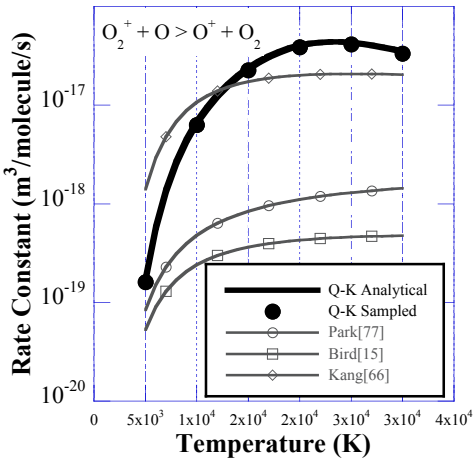

Figure C.49: Q-K reaction rates for reaction 49.

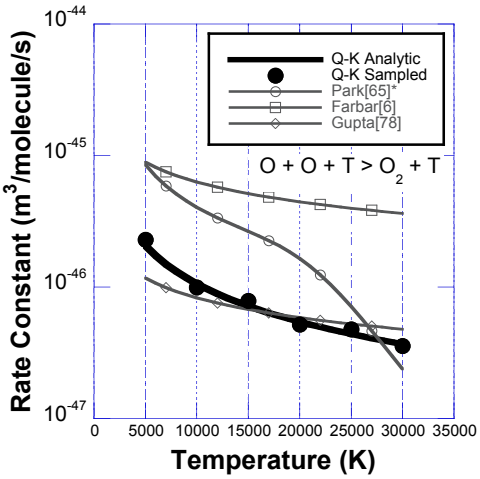

Figure C.50: Q-K reaction rates for reaction 50.

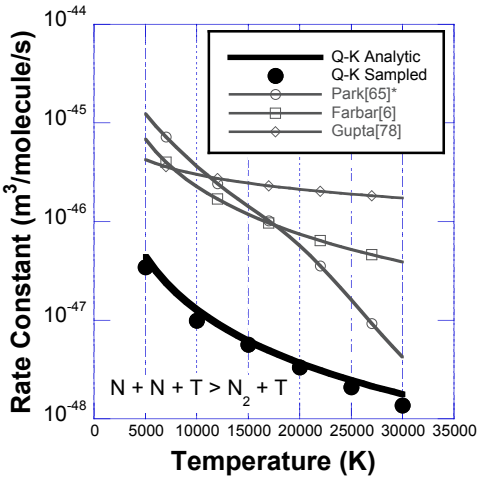

Figure C.51: Q-K reaction rates for reaction 51.

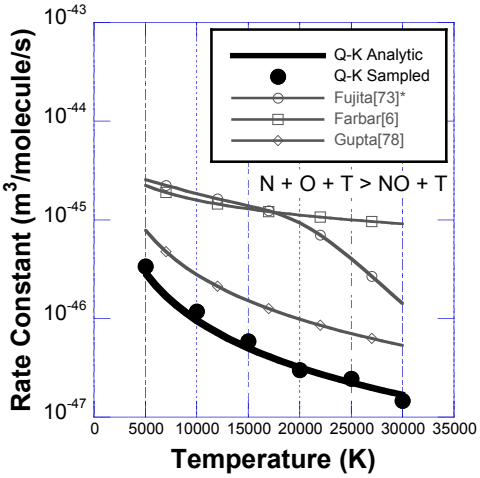

Figure C.52: Q-K reaction rates for reaction 52.

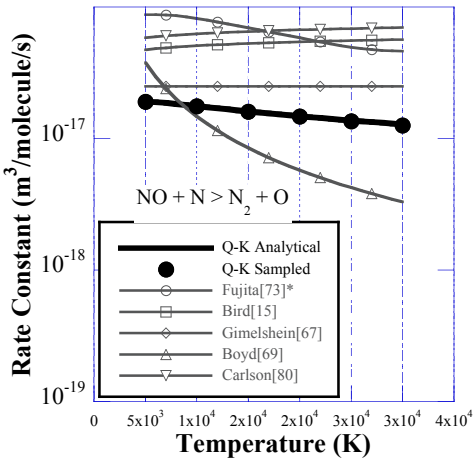

Figure C.53: Q-K reaction rates for reaction 53.

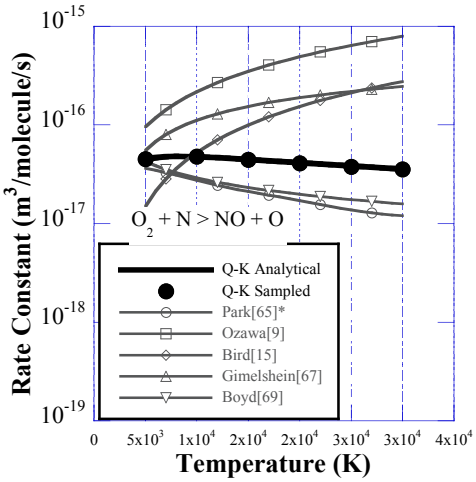

Figure C.54: Q-K reaction rates for reaction 54.

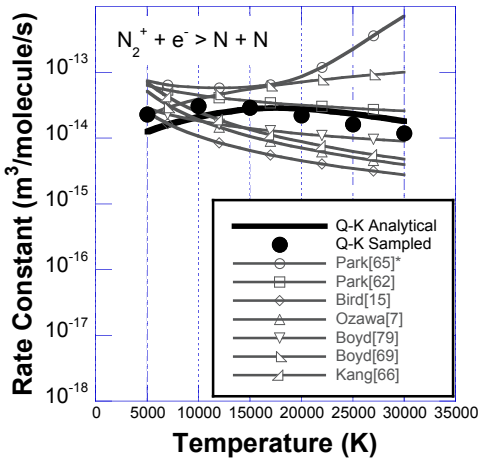

Figure C.55: Q-K reaction rates for reaction 55.

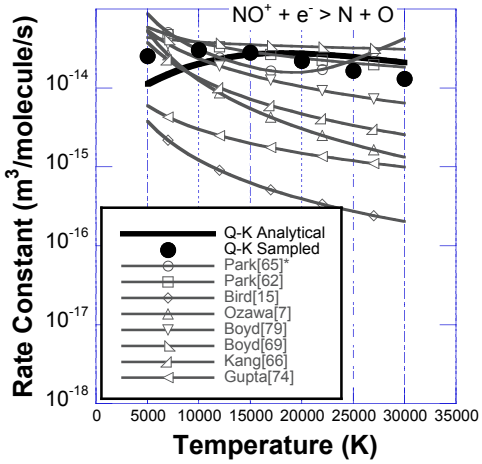

Figure C.56: Q-K reaction rates for reaction 56.

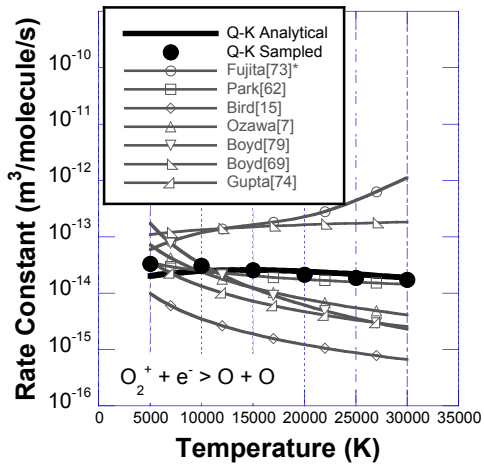

Figure C.57: Q-K reaction rates for reaction 57.

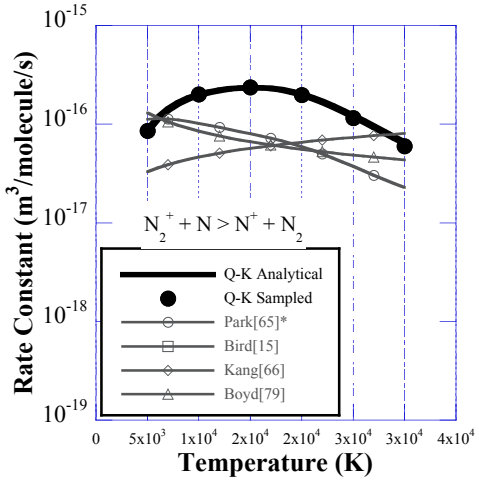

Figure C.58: Q-K reaction rates for reaction 58.

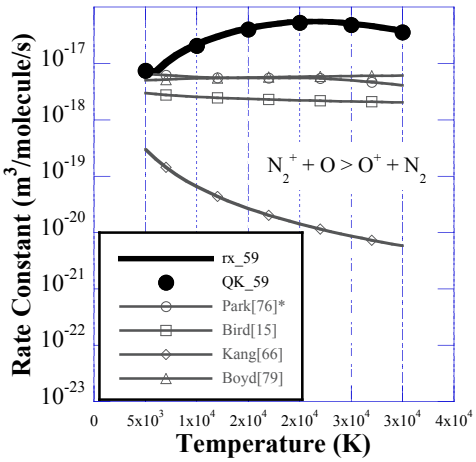

Figure C.59: Q-K reaction rates for reaction 59.

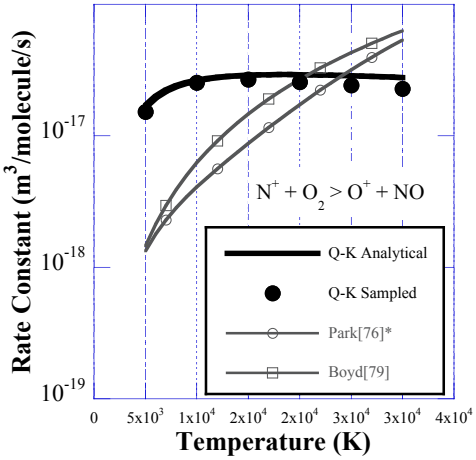

Figure C.60: Q-K reaction rates for reaction 60.

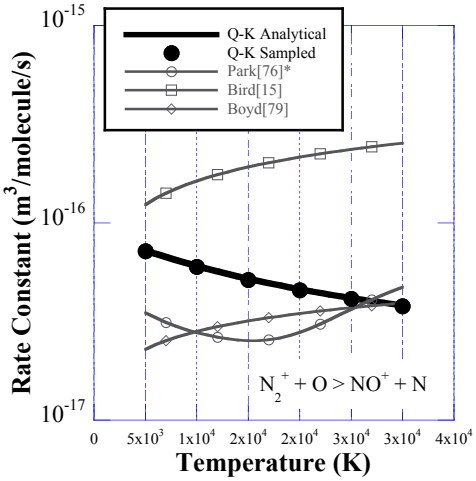

Figure C.61: Q-K reaction rates for reaction 61.

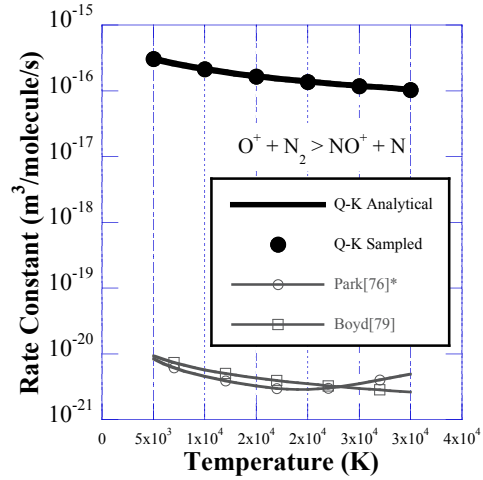

Figure C.62: Q-K reaction rates for reaction 62.

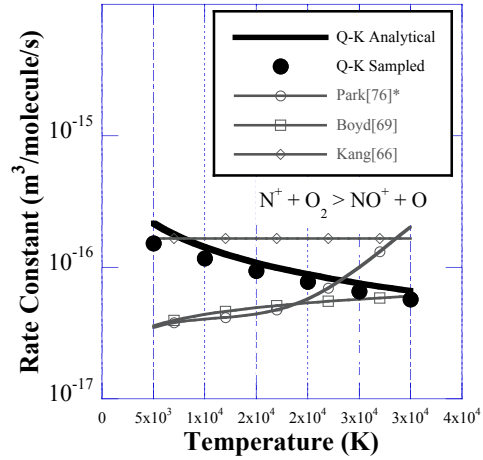

Figure C.63: Q-K reaction rates for reaction 63.

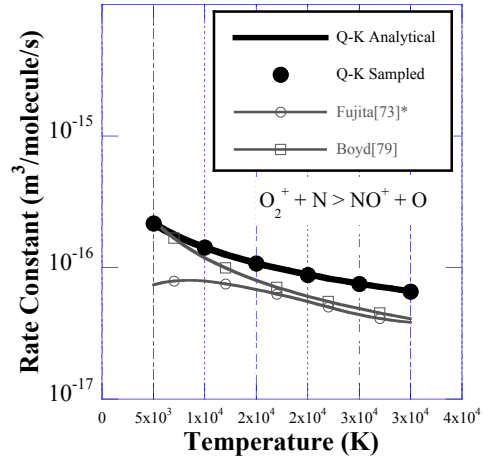

Figure C.64: Q-K reaction rates for reaction 64.

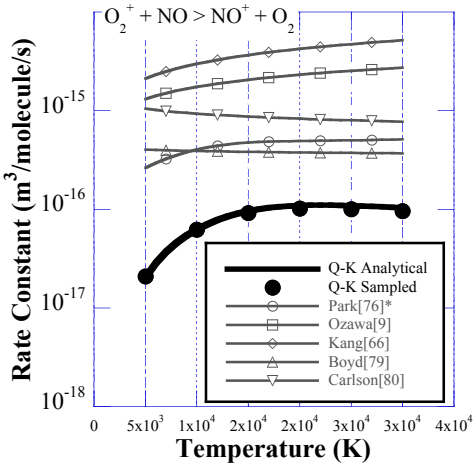

Figure C.65: Q-K reaction rates for reaction 65.

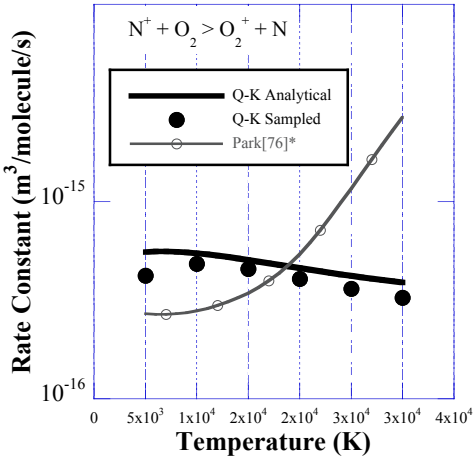

Figure C.66: Q-K reaction rates for reaction 66.

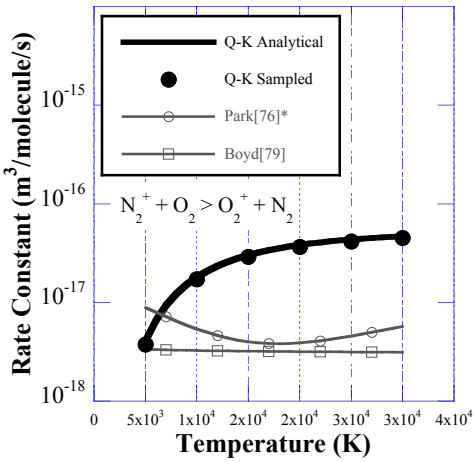

Figure C.67: Q-K reaction rates for reaction 67.

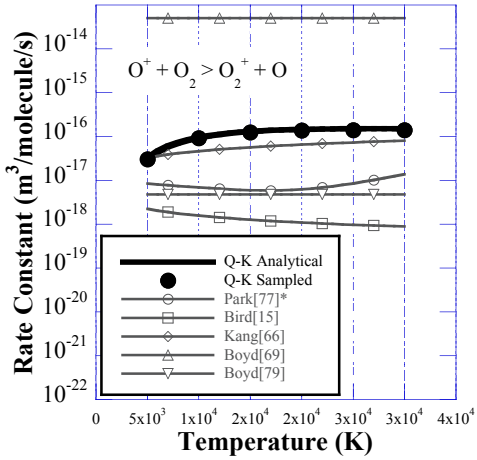

Figure C.68: Q-K reaction rates for reaction 68.

Bibliography

1. Bose, D., et al., *Uncertainty Assessment of Hypersonic Aerothermodynamics Prediction Capability*, in *42nd AIAA Thermophysics Conference*2011, AIAA Paper No. 2011-3141: Honolulu, HI.
2. Bird, G.A., *Molecular Dynamics and the Direct Simulation of Gas Flows*. 1994, Oxford, UK: Oxford University Press.
3. Ozawa, T., et al., *Quasi-Classical Trajectory Modeling of OH Production in Direct Simulation Monte Carlo.* Journal of Thermophysics and Heat Transfer, 2005. **19**(2): p. 235-244.
4. Farbar, E.D., *Kinetic Simulation of Rarefied and Weakly Ionized Hypersonic Fow Fields*, in *Aerospace Engineering*2010, The University of Michigan: Ann Arbor, MI. p. 170.
5. Farbar, E.D. and I.D. Boyd, *Simulation of Reactions Involving Charged Particles in Hypersonic Rarefied Flows*, 2009, AIAA Paper No. 2009-267.
6. Farbar, E.D. and I.D. Boyd, *Simulation of FIREII II Reentry Flow Using the Direct Simulation Monte Carlo Method*, 2008, AIAA Paper No. 2008-4103.
7. Ozawa, T., et al., *DSMC-CFD Comparison of a High Altitude, Extreme-Mach Number Reentry Flow*, 2008, AIAA Paper No. 2008-1216.
8. Ozawa, T., J. Zhong, and D.A. Levin, *Development of kinetic-based energy exchange models for noncontinuum, ionized hypersonic flows.* Physics of Fluids, 2008. **20**.
9. Ozawa, T., et al., *Modeling of the Stardust Reentry Flows with Ionization in DSMC*, in *45th AIAA Aerospace Sciences Meeting and Exhibit*2007, AIAA Paper No. 2007-611: Reno, NV.
10. Bird, G.A. *A Comparison of Collision Energy-based and Temperature-based Procedures in DSMC*. in *26th Symposium on Rarefied Gas Dynamics*. 2009. Kyoto, Japan: American Institue of Physics.
11. Bird, G.A. *Chemical Reactions in DSMC*. in *27th Symposium on Rarefied Gas Dynamics*. 2010. Pacific Grove, CA: American Institute of Physics.
12. Bird, G.A. *The Quantum-Kinetic Chemistry Model*. in *27th International Symposium on Rarefied Gas Dynamics*. 2010. Pacific Grove, CA.
13. Bird, G.A., *The Q-K Model for Gas-Phase Chemical Reaction Rates.* Physics of Fluids, 2011. **23**(10): p. 106101.
14. Gallis, M.A., R.B. Bond, and J.R. Torczynski, *A kinetic-theory approach for computing chemical-reaction rates in upper-atmosphere hypersonic flows.* The Journal of Chemical Physics, 2009. **131**(12): p. 124311.
15. Bird, G.A., *Nonequilibrium Radiation During Re-Entry at 10 km/s*, 1987, AIAA Paper No. 1987-1543.
16. Gallis, M.A. and J.K. Harvey, *Nonequilibrium Thermal Radiation from Air Shock Layers Modeled with Direct Simulation Monte Carlo.* Journal of Thermophysics and Heat Transfer, 1994. **8**(4): p. 765-772.

17. Carlson, A.B. and H.A. Hassan, *Radiation Modeling with Direct Simulation Monte Carlo.* Journal of Thermophysics and Heat Transfer, 1992. **6**: p. 631-636.
18. Ozawa, T., et al., *Development of Coupled Particle Hypersonic Flowfield-Photon Monte Carlo Radiation Methods.* Journal of Thermophysics and Heat Transfer, 2010. **24**(3): p. 612-622.
19. Johnston, C.O., B.R. Hollis, and K. Sutton, *Spectrum Modeling for Air Shock-Layer Radiation at Lunar-Return Conditions.* Journal of Spacecraft and Rockets, 2008. **45**(5): p. 865-878.
20. Johnston, C.O., B.R. Hollis, and K. Sutton, *Non-Boltzmann Modeling for Air Shock-Layer Radiation at Lunar-Return Conditions.* Journal of Spacecraft and Rockets, 2008. **45**(5): p. 879-890.
21. Cornette, E.S., *Forebody Temperature and Calorimeter Heating Rates Measured During Project Fire II Reentry at 11.35 km/s*, 1966, NASA TM X-1305.
22. Birdsall, C.K. and A.B. Langdon, *Plasma Physics via Computer Simulation*. 1985, New York: McGraw-Hill.
23. Hockney, R.W. and J.W. Eastwood, *Computer Simulation Using Particles*. 1988, Bristol, U.K.: Inst. of Phys. Publishing.
24. Bird, G.A., *Molecular Gas Dynamics*. 1976, Oxford, U.K.: Clarendon Press.
25. Taylor, J.C., A.B. Carlson, and H.A. Hassan, *Monte Carlo Simulation of Radiating Re-Entry Flow.* Journal of Thermophysics and Heat Transfer, 1994. **8**(3): p. 478-485.
26. Bird, G.A., *Low Density Aerothermodynamics*, 1985, AIAA Paper No. 1985-0994.
27. Bird, G.A., *Direct Simulation of Typical AOTV Entry Flows*, 1986, AIAA Paper No. 1986-1310.
28. Gallis, M.A. and J.K. Harvey, *Ionization Reactions and Electric Fields in Plane Hypersonic Shock Waves.* Progess in Astronautics and Aeronautics, 1992. **160**: p. 234-244.
29. Carlson, A.B. and H.A. Hassan, *Direct Simulation of Reentry Flows with Ionization.* Journal of Thermophysics and Heat Transfer, 1992. **6**(3): p. 400-404.
30. Boyd, I.D., *Monte Carlo Simulation of Nonequilibrium Flow in a Low-power Hydrogen Arcjet.* Physcis of Fluids, 1997. **9**(10): p. 4575-4584.
31. Nanbu, K., *Probability Theory of Electron-Molecule, Ion-Molecule, Molecule-Molecule, and Coulomb Collisions for Particle Modeling of Materials processing Plasmas and Gases.* IEEE Transactions of Plasma Science, 2000. **28**(3): p. 971-990.
32. Nanbu, K., *Stochasitc Theory of Motion and Collision of Charged Particle in a Uniform Electric Field.* Journal of the Physical Society of Japan, 1994. **63**: p. 979-983.
33. Nanbu, K., *Direct Simulation Scheme Derived from the Boltzmann Equation.-II. Multicomponent Gas Mixtures.* Journal of the Physical Society of Japan, 1980. **49**: p. 2042-2049.

34. Nanbu, K., *Direct Simulation Scheme derived from the Boltzmann Equation-I: Monocomponent Gases.* Journal of the Physical Society of Japan, 1980. **49**: p. 2042-2049.
35. Babovsky, H. and R. Illner, *A Convergence Proof for Nanbu's Simulation Method for the Full Boltzmann Equation.* SIAM J. Num. Anal., 1989. **26**: p. 45-65.
36. Wilmoth, R.G., G.J. LeBeau, and A.B. Carlson, *DSMC Grid Methodologies for Computing Low-Density, Hypersonic Flows About Reusable Launch Vehicles*, 1996, AIAA 1996-1812.
37. LeBeau, G.J. and F.E. Lumpkin III, *Application Highlights of the DSMC Analysis Code (DAC) Software for Simulating Rarefied Flows.* Computer Methods in Applied Mechanics and Engineering, 2001. **191**(6-7): p. 595-609.
38. LeBeau, G.J., K.A. Boyles, and F.E. Lumpkin III, *Virtual Sub-Cells for the Direct Simulation Monte Carlo Method*, 2003, AIAA 2003-1031.
39. Gallis, M. and J.R. Torczynski, *Effect of Collision-Partner Selection Schemes on the Accuracy and Efficiency of the Direct Simulation Monte Carlo Method.* International Journal for Numerical Methods in Fluids, 2010.
40. Burt, J.M., E. Josyula, and I.D. Boyd, *Techniques for Reducing Collision Separation in Direct Simulation Monte Carlo Calculations*, in *42nd AIAA Thermophysics Conference*2011, AIAA Paper No. 2011-3312: Honolulu, HI.
41. Bird, G.A., *Monte Carlo simulation in an engineering context.* Progess in Astronautics and Aeronautics, 1981. **74**(1).
42. Borgnakke, C. and P.S. Larsen, *Statistical collision model for Monte Carlo simulation of polyatomic gas mixtures.* Journal of Computational Physics, 1975. **18**.
43. Bergemann, F. and I.D. Boyd, *New Discrete Vibrational Energy Model for Direct Simulation Monte Carlo Method.* Progess in Astronautics and Aeronautics, 1994. **160**: p. 174-183.
44. Haas, B.L., *Thermochemistry Models Applicable to a Vectorized Particle Simulation*, in *Department fo Aeronautics and Astronautics*1990, Stanford University.
45. Lumpkin III, F.E., B.L. Haas, and I.D. Boyd, *Resolution of Differences Between Collision Number Definitions in Particle and Continuum Simulations.* Physics of Fluids A, 1991. **3**: p. 2282.
46. Haas, B.L., et al., *Rates of Thermal Relaxation in Direct Simulation Monte Carlo Methods.* Physics of Fluids, 1994. **6**(6): p. 2191-2201.
47. Jeans, J.H., *The Dynamical Theory of Gases*. 2 ed. 1916, London: Cambridge University Press.
48. Landau, L. and E. Teller, *Zur Theorie der Schalldispersion.* Phys. Z. Sowjetunion, 1936. **10**: p. 14.
49. Gimelshein, S.F., I.D. Boyd, and M.S. Ivanov, *Modeling of Internal Energy Transfer in Plume Flows of Polyatomic Molecules by the DSMC Method*, 1999, AIAA Paper No. 1999-738.
50. Gimelshein, N.E., S.F. Gimelshein, and D.A. Levin, *Vibrational Relaxation Rates in the Direct Simulation Monte Carlo Method.* Physics of Fluids, 2002. **14**(12): p. 4452-4455.

51. Boyd, I.D., *Relaxation of Discrete Rotational Energy Distributions Using a Monte Carlo Method.* Physics of Fluids A, 1993. **5**(9): p. 2278-2286.
52. Parker, J.G., *Rotational and Vibrational Relaxation in Diatomic Gases.* Physics of Fluids, 1959. **2**(4): p. 449-462.
53. Millikan, R.C. and D.R. White, *Systematics of Vibrational Relaxation.* Journal of Chemical Physics, 1963. **39**(12): p. 3209-3213.
54. Gallis, M.A. and J.K. Harvey, *Atomic Species Radiation from Air Modeled with Direct Simulation Monte Carlo Method.* Journal of Thermophysics and Heat Transfer, 1995. **9**(3): p. 456-463.
55. Bird, G.A. *Simulation of Multi-Dimensional and Chemically Reacting Flows*. in *11th International Symposium on Rarefied Gas Dynamics*. 1978. Cannes, France: Commissariat a Lenergie Atomique.
56. Tonks, L. and I. Langmuir, *General Theory of a Plasma Arc.* Physical Review, 1929. **34**(1): p. 876-922.
57. Bartel, T.J. and C.R. Justiz, *DSMC Simulation of Ionized Rarefied Flows*, in *24th AIAA Fluid Dynamics Conference*1993, AIAA Paper 1993-3095: Orlando, FL.
58. Justiz, C.R. and C. Dalton, *A Hybrid Flow Model for Charged and Neutral Particles Around Spacecraft in Low Earth Orbit*, in *27th AIAA Thermophysics Conference*1992, AIAA Paper 1992-2935: Nashville, TN.
59. Gallis, M., R. Prasad, and J.K. Harvey, *The Effect of Plasmas on the Aerodynamic Performance of Vehicles*, 1998, AIAA 1998-2666.
60. Park, C., *Nonequilibrium Hypersonic Aerothermodynamics*. 1990, New York: Wiley.
61. Lord, R.G., *Modeling Vibrational Energy Exchange of Diatomic Molecules Using the Morse Interatomic Potential.* Physics of Fluids, 1998. **10**(3): p. 4.
62. Koura, K. and H. Matsumoto, *Variable soft sphere molecular model for inverse-power-law or Lennard-Jones potential.* Physics of Fluids A, 1991. **3**.
63. Park, C., R.L. Jaffe, and H. Partridge, *Chemical-Kinetic Parameters of Hyperbolic Earth Entry.* Journal of Thermophysics and Heat Transfer, 2001. **15**(1): p. 76-90.
64. Kang, S.W. and M.G. Dunn, *Theoretical and Measured Electron-Density Distributions for the RAM Vehicle at High Altitudes*, 1972, AIAA Paper No. 1972-689.
65. Gimelshein, N.E. and D.A. Levin, *Modeling of Glow Radiation in the Rarefied Flow About an Orbiting Spacecraft.* Journal of Thermophysics and Heat Transfer, 2000. **14**(4): p. 471-479.
66. Johnston, H.S., *Gas Phase Reaction Kinetics of Neutral Oxygen Species*, U.S.D.o. Commerce, Editor 1968, National Bureau of Standards: Washington, D.C.
67. Boyd, I.D. and T. Gokcen, *Computation of Axisymmetric and Ionized Hypersonic Flows Using Particle and Continuum Methods.* AIAA Journal, 1994. **32**(9): p. 1828-1835.
68. Bourdon, A. and P. Vervisch, *Study of a Low-Pressure Nitrogen Plasma Boundary Layer Over a Metallic Plate.* Physics of Plasmas, 1997. **4**: p. 4144-4157.

69. Park, C., *Chemical-Kinetic Problems of Future NASA Missions*, 1991, AIAA Paper No. 1991-464.
70. Losev, S.A., et al., *Thermochemical Nonequilibrium Kinetic Models in Strong Shock Waves on Air*, 1994, AIAA Paper No. 1994-1990.
71. Fujita, K., T. Yamada, and N. Ishii, *Impacts of Ablation Gas Kinetics on Hyperbolic Entry Radiative Heating*, in *44th AIAA Aerospace Sciences Meeting*2006, AIAA Paper No. 2006-1185: Reno, NV.
72. Gupta, R.N., *Navier-Stokes and Viscous Shock-Layer Solutions for Radiating Hypersonic Flows*, 1987, AIAA Paper No. 1987-1576.
73. Phelps, A.V., *Cross Sections and Swarm Coefficients for Nitrogen Ions and Neutrals in N2 and Argon Ions and Neutrals in Ar for Energies from 0.1 eV to 10 keV.* J. Phys. Chem. Ref. Data, 1991. **20**: p. 557.
74. Park, C., *Review of Chemical-Kinetic Problems of Future NASA Missions, I: Earth Entries.* Journal of Thermophysics and Heat Transfer, 1993. **7**: p. 385-398.
75. Park, C., J.T. Howe, and R.L. Jaffe, *Review of Chemical-Kinetic Problems of Future NASA Missions, II: Mars Entries.* Journal of Thermophysics and Heat Transfer, 1994. **8**(1): p. 9-23.
76. Gupta, R.N., et al., *A Review of Reaction Rates and Thermodynamic and Transport Properties for an 11-Species Air Model for Chemical and Thermal Nonequilibrium Calculations to 30,000 K*, 1990, NASA RP-1232.
77. Boyd, I.D., *Modeling of Plasma Formation in Rarefied Hypersonic Entry Flows*, 2007, AIAA Paper No. 2007-206.
78. Carlson, A.B., *Direct Simulation Monte Carlo with Ionization and Radiation*, in *Department of Mechanical and Aerospace Engineering*1990, North Carolina Sate University: Raleigh. p. 82.
79. Tayal, S.S., *Effective Collision Strengths for Electron Impact of N I.* Atomic Data and Nuclear Data Tables, 2000. **76**: p. 191-212.
80. Frost, R.M., et al., *Calculated cross sections and measured rate coefficients for electron-impact excitation of neutral and singly ionized nitrogen.* Journal of Applied Physics, 1998. **84**(6): p. 2989-3003.
81. Zatsarinny, O. and S.S. Tayal, *Electron Collisional Excitation Rates for O I using the B-Spline R-Matrix Approach.* The Astrophysical Journal Supplement Series, 2003. **148**: p. 575-582.
82. Bhatia, A.K. and S.O. Kastner, *The Neutral Oxygen Spectrum. I. Collisionally Excited Level Populations and Line Intensities under Optically Thin Conditions.* The Astrophysical Journal Supplement Series, 1995. **96**: p. 325-341.
83. Chernyi, G.G. and S.A. Losev, *Development of Thermal Protection Systems for Interplanetary Flight*, R.I.o. Mechanics, Editor 1999, International Science and Technology Center: Moscow.
84. Telulet, P., J.P. Sarrette, and A.M. Gomes, *Calculation of Electron-Impact Inelastic Cross-Sections and Rate Coefficients for Diatomic Molecules. Application to Air Molecules.* Journal of Qualitative Spectroscopy and Radiative Transfer, 1999. **62**: p. 549-569.

85. Gorelov, V.A., et al., *Experimental and Numerical Study of Nonequilibrium Ultraviolet NO and N2+ Emission in a Shock Layer.* Journal of Thermophysics and Heat Transfer, 1998. **12**(2): p. 172-179.
86. Johnston, C.O., *Nonequilibruim Shock-Layer Radiative Heating for Earth and Titan Entry*, in *Aerospace Engineering*2006, Virginia Polytechnic Institute and State University: Blacksburg, VA. p. 245.
87. Gorelov, V.A., et al. *Nonequilibrium Ionization and Radiation Behind Shock Wave in Martian Atmosphere*. in *Third European Symposium on Aerothermodynamics for Space Vehicles*. 1998. Noordwijk, The Netherlands: European Space Agency.
88. Park, C., *Rate Parameters for Electronic Excitation of Diatomic Molecules II. Heavy Particle-Impact Processes*, 2008, AIAA Paper No. 2008-1446.
89. Flagan, R.C. and J.P. Appleton, *Excitation Mechanisms of the Nitrogen First-Positive and First-Negative Radiation at High-Temperature.* Journal of Chemical Physics, 1972. **56**(3): p. 1163-1173.
90. Nagy, O., *Excitation Cross-Sections of N2+ Molecular Ion by Electron Impact and the Vibrational Energy Levels of the Three Target States.* Chemical Physics, 2003. **286**(1): p. 109-114.
91. Guerra, V. and J. Loureiro, *Electron and heavy particle kinetics in a low-pressure nitrogen glow discharge.* Plasma Sources Science & Technology, 1997. **6**: p. 361-372.
92. Raynaud, E., et al., *Huygens Aerothermal Environment: Radiative Heating*, in *3rd International Planetary Probe Workshop*2005, ESA: Anavyssos, Greece.
93. Magin, T.E., et al., *Nonequilibrium Radiation Modeling for Huygens Entry*, in *3rd International Planetary Probe Workshop*2005: Anavyssos, Greece.
94. Cheatwood, F.M. and P. Gnoffo, *User's Manual for the Langley Aerothermodynamic Upwind Relaxation Algorithm (LAURA)*, April 1996, NASA TM 4674.
95. Gnoffo, P., R.N. Gupta, and J.L. Shinn. *Conservation Equations and Physical Models for Hypersonic Air Flows in Thermal and Chemical Nonequilibrium*. in *NASA TP 2867*. Feb. 1989.
96. Roe, P.L., *Approximate Riemann Solvers, Parameter Vectors, and Difference Schemes.* Journal of Computational Physics, 1981. **43**(2): p. 357-372.
97. Yee, H.C., *On Symmetric and Upwind TVD Schemes*, in *NASA TM 883251*1986.
98. Mcbride, B.J., M.J. Zehe, and S. Gordon, *NASA Glenn Coefficients for Calculating Thermodynamic Properties of Individual Species*, Sept. 2002, NASA TP 2002-211556.
99. Sutton, K. and P. Gnoffo, *Multi-Component Diffusion with Application to Computational Aerothermodynamics*, 1998, AIAA Paper 98-2575.
100. Ralchenko, Y. and e. al. *NIST Atomic Spectra Database, Version 3.1.0*. July 2006; Available from: http://physics.nist.gov/PhysRefData/ASD/index.html.
101. Team, T.O.P., *The Opacity Project, Vol. 1*. 1995, Bristol and Philedelphia: Institute of Physics Publishing.
102. Cunto, W. and e. al, *TOPbase at the CDS.* Astronomy and Astrophysics, 1993. **275**: p. L5-L8.

103. Soon, W.H. and J.A. Kunc, *Nitrogen Plasma Continuum Emission Associated with N-(3P) and N-(1D) Ions.* Physical Review A, 1990. **41**: p. 4531-4533.
104. Chauveau, S., et al., *Radiative Transfer in LTE Air Plasmas for Temperatures up to 15,000 K.* Journal of Qualitative Spectroscopy and Radiative Transfer, 2003. **77**: p. 113-130.
105. Chambers, L.H., *Predicting Radiative Heat Transfer in Thermochemical Nonequilibrium Flow Fields*, 1994, NASA TM-4564.
106. Laux, C.O., *Optical Diagnostics and Radiative Emission of Air Plasmas*, 1993, High Temperature Gas Dynamics Lab, Mechanical Engineering Dept., Rept. T-288, Stanford University.
107. Whang, T.J., et al., *Franck-Condon Factors of the ..... Transitions of N2.* Journal of Quantitative Spectroscopy and Radiative Transfer, 1996. **55**: p. 335-344.
108. Stahel, D., M. Leoni, and K. Dresslar, *Nonadiabatic Representations of the 1Σu and 1Πu States of the N2 Molecule.* Journal of Chemical Physics, Sept. 1983. **79**: p. 2541-2558.
109. Chauveau, S., et al., *Contributions of Diatomic Molecular Electronic Systems to Heated Air Radiation.* Journal of Quantitative Spectroscopy and Radiative Transfer, 2002. **72**: p. 503-530.
110. Park, C., *Radiation Enhancement by Nonequilibrium in Earth's Atmosphere.* Journal of Spacecraft and Rockets, 1985. **22**: p. 27-36.
111. Hash, D., et al., *FIRE II Calculations for Hypersonic Nonequilibrium Aerothermodynamics Code Verification: DPLR, LAURA and US3D*, 2007, AIAA 2007-605.